Title
Exploring Graphene Physics for Optical Sensing

Author
Horng, Jason

Publication Date
2016

Peer reviewed|Thesis/dissertation

Exploring Graphene Physics for Optical Sensing

by

Jason Shih An Horng

A Dissertation submitted in partial satisfaction of the

requirements for the degree of

Doctor of Philosophy

in

Physics

in the

Graduate Division

of the

University of California, Berkeley

Committee in charge:

Professor Michael Crommie, Chair
Professor Feng Wang
Professor Seung-Wuk Lee

Spring 2016

Abstract

Exploring Graphene Physics for Optical Sensing

by

Jason Shih An Horng

Doctor of Philosophy in Physics

University of California, Berkeley

Professor Michael Crommie, Chair

Since the discovery of graphene in 2004, it has drawn significant attention in many different research or application fields due to its extraordinary electrical and optical properties. As a two-dimensional material, both graphene's electrical and optical properties can be dramatically modified due to small perturbations from the surrounding environment. Therefore, graphene has great potential as active medium for versatile and sensitive sensors. Early studies have demonstrated excellent sensitivity of graphene field-effect transistor for gas molecule sensing and action potential detection. As will be shown in this dissertation, graphene optical sensor can also be designed to have good sensitivity and enables new possibilities of optical spectroscopic measurement as well as opto-electronic studies. With the versatility of graphene, we show that graphene provides a great platform for electrochemical optical sensing as well as opto-electronic sensor in bio-electric detection.

There are three major topics in this dissertation. The first one is an extensive study of the intrinsic optical phenomena of Dirac electrons in monolayer graphene. The chemical potential of graphene can be tuned efficiently by electric field due to the two-dimensional nature and the unusual band structure of graphene. We study gate-dependence of both interband and intraband excitations with THz, infrared to visible optical spectroscopy. This work provides a first glance at the fundamental linear optical properties of graphene and forms the basis of application of graphene optical sensing.

In the second part, a tunable mid-infrared laser for graphene optical sensor application was developed. Lasers are powerful tools in sensing techniques since due to coherent behavior as well as the ability of performing imaging and spectroscopy. We develope our own mid-infrared laser source through parametric nonlinear down-conversion by two different methods, namely ,difference frequency generation and synchronized pumped optical parametric oscillator. Both methods generate strong, coherent, ultrafast mid-infrared light source from 2.4 to 4.7μm covering most of the molecular vibrational resonances. These light generation setups are ideal for infrared spectroscopy of molecules and will be employed to perform graphene-enhanced spectroscopy in the later chapters.

At last, the possibility of graphene optical sensing in both electrochemical and bio-electrical contexts are explored. As mentioned earlier, graphene's versatility makes it not only a remarkable transparent electrode, but also an interesting electro-chemical platform to study molecular dynamics during a chemical reaction. Here we demonstrate that, with micro-fabrication of graphene, we create an attractive platform for vibrational spectroscopy, which has interface specificity, sub-monolayer detection sensitivity and imaging capability, at the electrolyte/electrode interfaces. In another direction, we study the potential application of graphene in bio-electric detection and imaging. Research into the development of bio-electric imaging has been quite extensive in the past decade since brain research starts to allow us decoding the basic signaling through these imaging techniques. We show that, by integrating graphene with specially designed waveguides, we achieve sensitive local charge detectors and could have potential application in neuro-science for wide-field and highly-parallel action potential sensing.

Contents

List of Figures

Acknowledgements

I would like to extend my gratitude to the many people who helped to bring this research project to fruition. First and foremost I would like to thank my advisor, professor Feng Wang, for providing me the opportunity of taking part in the two dimensional material research. I am so deeply grateful for his continuous guidance and support throughout this project and through my entire Ph.D. study. Feng has been excellent and trusted mentors, and his simple and elegant physics presentations will continue to inspire me. During the most difficult times in my Ph.D. career, he was also willing to spend time talking to me and gave me the freedom I needed to move on. I genuinely appreciate his patient and thoughtful approach for students.

I also appreciate the help from Prof. Ron Shen and Prof. Mike Crommie. They are always willing to spend time with students and offer guidance from scientific understandings to career developments. Prof. Bianxiao Cui at Stanford University is our collaborator on the biological sensor project. I am grateful for her help for introducing me into biology research. She was always caring our progress and gave helpful advice from the biological side. I also want to thank Prof. Mike Crommie and Prof. Seung-Wuk Lee for advices and serving as my committee.

I thank my colleagues from the Wang group for their encouragement, discussions, advice, teaching, and help on countless occasions. My collaboration with Chih-Fan Chen and Baisong Geng in the graphene spectroscopic study have been wonderful and fruitful experiences. I learnt from them the basic optical and electric transport experimental techniques which are extremely important for my later research. Yaqing Bie, a fellow graduate visiting student whom I worked with for a long time, is an intelligent and careful person. I always found myself impressed by her cautious sample preparation procedure and her willingness to help other people. During the days I work with her, she also gave me lots of encouragement when the project does not go as we expected. Zhiwen Shi is a generous and patient teacher and also provided very helpful advices on my career development. In the biological sensor project, I worked in my senior years with Halleh Balch who is a brilliant young graduate student. During our commuting to Stanford, we discussed our future plans and she often pushed me to be more active on job searching, which made me a little nervous. But, I was really appreciate her positive attitude toward everyone.

I would also like to thank my previous and current officemates, Weitao Liu, Jaeho Sung, Kaihui Liu, Steve Byrnes, Bo Zeng, Sufei Shi, Likai Li, Chaw Keong Yong, as we always share thoughts and snacks in a crowded room. Especially, Sufei Shi, a very kind and patient mentor, helped me a lot on figuring out my interests and also my future career development. Lastly, I want to thank all the other fellow students and postdocs in Wang group and Shen group for their support; they are Tomer Drori, David Cho, Tsung-Ta Tang, Long Ju, Xiaoping Hong, Yu-Chieh Wen, Hui Ling Han, Yinghui Sun, Xinglai Shen, Jonghwan Kim, Chenhao Jin, Mingming Lu, Lili Jiang, Xunjun He, Steve Drapcho, Sheng Wang, Iqbal Utama, Trinity Joshi, Hans Kleemann, Rai Takahashi Kou, Ji-Hun Kang, Sihan Zhao.

It is also fortunate for me to be able to work with wonderful colleagues in Cui and Crommie group. I had long term collaboration with Hsin-zon Tsai and Patrick Forrester in Crommie group on graphene growth and fabrication process development. I appreciated their systematic study on the graphene growth and their efforts truly created new possibilities in experimental graphene studies. I worked with Carter Lin and Allister McGuire in Cui group at Stanford for several years. Their knowledge and expertise proved to be a great tool in our interdisciplinary study. I learnt from them various methods in biology study and different points of view on understanding the living world.

I also need to emphasize all the supports coming from staffs in physics department at Berkeley, especially from Anne Takizawa, Donna Sakima, Anthony Vitan, Carlos Bustamante and Meifei Lin. They take care of our miscellaneous affairs and provide us a great atmosphere and reliably infrastructure for research.

Finally I want to express my appreciation towards all friends and teammates in the BATS volleyball club, especially Limin Lee, Ho-Hsiang Wu, Sean Wu, Wei-Chun Kao, Ting-Ying Chung, Emma Yu, Kenghao Chang, Ling-Chieh Kung, I-Chih Shih, Peichun Hsu, Chang-Ming Jiang, Yu-Chieh Chang, Yi-Bo Liao, Ching-Yi Hsu, Shu-wei Tsai, A-Wei Chen, Aurora Lin, Lien-Yung Kao, and I-Chin Wu. Their supports had made my life in Berkeley more colorful and enjoyable. Finally, I must express my gratitude to my parents, Roy Horng and Meilin Chiang, and to my wife, Chih-yin Chou, for providing me with unfailing support and continuous encouragement throughout my years of study. This accomplishment would not have been possible without them.

Chapter 1

Introduction

1.1 Background and Motivation

In recent decades the invention of laser accelerates the development of spectroscopy and broadens the spectroscopic studies with completely new capabilities such as extremely high power, narrow linewidth, strong coherence and temporal resolution. Being such a versatile tool, laser spectroscopy could be virtually applied to many fields in modern society. Various fields of science have benefited significantly from laser spectroscopic techniques ranging from electronic band structure determination, near-field spectroscopy, fluorescence dye-labeled imaging to chemical gas identification.

Sensing techniques based on laser possess many advantages compared with techniques based on other light sources. The highly directional beam and spatial coherence enable laser to detect remote objects with LIDARs system (LIght Detection And Ranging) and determine distance accurately with Michelson interferometer which are impractical with incoherent light sources. The ability of performing visible to infrared spectroscopy also enables development of highly sensitive, species-selective and efficient technique for spectroscopic gas analysis. Furthermore, one can combine laser with optical cavities, waveguides, photonic crystals to perform cavity-based spectroscopy which can enhance the sensitivity by orders of magnitude. Nowadays, application of various laser sensing techniques does not remain confined to the laboratory and is already employed with the real world of sensing and chemical analysis.

On the other side, graphene, being a newly discovered two-dimensional material, has already drawn a lot attentions in many different research or application fields. Superior electrical conductivity and its gate dependence have been predicted and demonstrated experimentally. Possible applications like transparent electrode have been applied to commercial devices. In addition to the electrical properties, graphene has extraordinary optical properties. The absorption spectrum has a constant of 2.3% over a range from infrared to visible, therefore could enable an ultra broadband application. More importantly, one can modulate this absorption through electrostatic gating and turn off this optical transitions almost completely. This is due to graphene's two-dimensional nature and its unusual electronic band structure. One expect that a tiny variation in the surrounding can produce a dramatic effect on graphene's electrical or optical properties. Therefore, utilizing graphene or other two-dimensional material as an active medium for sensor is promising and has been studied extensively in the past few years.

In this thesis, I will focus on combing laser techniques with graphene and explore the possibility to use graphene as an optical sensing medium. The sensing techniques we developed could enable the graphene application in monitoring molecules during an eletro-chemical process and detecting various bio-electrical events in a biological system.

1.2 Outline of Thesis

In Chapter 2, I focus on the basic study of linear optical properties of Dirac electrons in monolayer graphene. Both fourier-transformed infrared spectroscopy and visible spectroscopy were performed to understand two major optical phenomena, intraband and interband optical transitions, in graphene. Gate-dependent absorption spectra are also taken with various gating techniques including silicon back gate and ion gel gating methods. The wide-range gate-dependent absorption spectra are then discussed with a physical model. It turns out that the absorption spectra can be described by our model considering both intraband and interband optical transitions.

In Chapter 3, I focus on a development of mid-infrared laser source with parametric down-conversion processes. Wavelength conversion of laser beams with a nonlinear process is an effective method to generate wavelengths outside the range of available laser materials. The working principle of our home-built difference frequency generation and synchronously pumped optical parametric oscillator setup will be introduced and the characterization of the light source properties will be shown. The produced coherent light sources can be scanned from 2.4 to 4.7μm which is the "fingerprint" region of molecular vibrational transitions. In the next chapter, we combine these light sources with graphene for molecule sensing.

In Chapter 4, a laser-based diffraction vibration spectroscopy at the electrolyte/electrode interfaces using graphene grating electrodes is demonstrated. A big obstacle in the development of electrochemistry field is the lack of a real-time imaging and high throughput tool to study the dynamics of chemical reactions with sub-monolayer sensitivity. However this situation could be addressed by a novel application of the diffraction spectroscopy, where one makes use of the strong power of laser and improve the relative contrast by ~ 50 times compared with conventional absorption spectroscopy. With improved laser stability and balanced detection, our technique can probe as low as about 1% of a monolayer coverage and provides a powerful tool to investigate fundamental processes at the electrolyte/electrode interfaces in an active electrochemical cell.

Finally in Chapter 5, I utilize the diffraction-based detection scheme with graphene grating structures that allows wide-field imaging and high-sensitivity measurements of electric field in solution at the same time. This electric potential sensor in solution is aimed to integrate with in-vitro cell cultures and enable action potential sensing to provide a complementary method for bio-electricity imaging. Later, another novel imaging method through incorporating graphene with a planar waveguide is developed to achieve high surface-specificity together with high sensitivity. The sensitivity is enhanced by 250 times and the detectable level is equivalent to 15μV with a bandwidth of 10Hz-10kHz. I also show that the imaging capability of our device can be used to monitor spatial-temporal dynamics of electric

field in real-time with cameras and has potential application in studying various electrophoresis processes and biological electrical signaling.

With the advance of two-dimensional materials research, these novel sensing methods can readily be applied to other materials and have potentials to construct opto-electronics with diverse purposes. We envision that these techniques can be used to monitor electron, ion and molecule dynamics in a wide range of devices and help to optimize the design of electrochemical engineering or bio-interfaces. Furthermore, the novel probes have high sensitivity as well as imaging capability, therefore researchers can applied them to many chemical and biological processes and facilitate new discovery in many fields.

Chapter 2

Gate-Variable Optical Transitions in Graphene

2.1 Introduction

Graphene provides a unique material system to study Dirac fermion physics in two dimensions. Researchers have demonstrated in graphene exotic Dirac fermion phenomena ranging from anomalous quantum Hall effects[1,2] to Klein tunneling[3] in low-frequency (dc) electrical transport. Besides applications in electrical transportation, graphene also has promising optical and optoelectronic properties: their low energy transitions can be continuously tuned by a gate voltage and the exotic band structure provides wide-band application range from THz to visible range.[4] Two major optical phenomena in graphene are intraband and interband optical transitions[5,6] and both of them are gate-variable.[7,8] We developed sensitive THz, infrared to visible optical spectroscopy using various techniques in different wavelength to probe these effects. The wide-range absorption spectroscopy ranging are discussed in this chapter and can be described by a model considering both intraband and interband optical transitions.

The understanding of gate-variable graphene optical conductivity is essential for developing graphene-based opto-electronics and future applications. The spectrum of graphene will also be used in the later chapters for designing various chemical or biological sensing techniques. Graphene optical transitions including both interband and intraband can be understood with its electronic structure and Fermi golden rules. Here, we start from introducing the basic electronics structure of graphene using tight-binding model.[9,10]

2.2 Electronic Structure of Graphene

Most of the graphene's electronic properties could be exactly calculated by a simple tight-binding theory. The graphene lattice consists of carbon atoms locates at honeycomb lattice and one carbon atom connects with the nearby three carbon atoms. The carbon-carbon chemical bonds are hybridized orbitals generated by superposition of 2s with $2p_x$ and $2p_y$ orbitals, i.e. the so-called sp2 hybridization. The electrons in the covalent bonds form deep fully filled valence bands, and thus their effects on the conductivity can be safely disregarded. The unhybridized$2p_z$ orbital is only slightly perturbed by the neighboring atoms, therefore a good description of graphene electronic properties is the tight-binding

approximation assuming that its electronic states can be simply represented by a linear combination of $2p_z$ orbitals. The resulting Hamiltonian can be represented by

$$H = -t\sum_{R,\sigma}\sum_{\delta=\delta_{1,2,3}}[a_\sigma^\dagger(R)b_\sigma(R+\delta)+H.c.] \quad \text{Eq. 2-1}$$

, where the operator $a_\sigma^\dagger(R)$creates an electron in $2p_z$ orbital in the sublattice A, whereas $b_\sigma^\dagger(R)$does the same in sublattice B; t is the hopping parameter connecting first-nearest neighbors, with a value of 3.2 eV. The spatial vectors$\boldsymbol{\delta}_{1,2,3}$ are represented inFig. 2-1 and have the form:

$$\boldsymbol{\delta}_1 = \frac{a}{2}(1,\sqrt{3}), \boldsymbol{\delta}_2 = \frac{a}{2}(1,-\sqrt{3}), \boldsymbol{\delta}_3 = -a\ (1,0) \quad \text{Eq. 2-2}$$

, where $a = 2.46$Å is the lattice constant of graphene. We can transform the Hamiltonian to momentum space and it reads:

$$H = \sum_{k,\sigma}\psi_{k,\sigma}^\dagger\begin{pmatrix}0 & -t\phi_k\\ -t\phi_k^* & 0\end{pmatrix}\psi_{k,\sigma} \quad \text{Eq. 2-3}$$

where $\psi_{k,\sigma}^\dagger = \begin{pmatrix}a_{k,\sigma}^\dagger & b_{k,\sigma}^\dagger\end{pmatrix}$, $\phi_k = \sum_{i=1,2,3}\exp(i\boldsymbol{k}\cdot\boldsymbol{\delta}_i)$.

By diagnosing the Hamiltonian, we can obtain the energy dispersion relation of π(bonding) and π^*(anti-bonding) bands:

$$E_\pm(\boldsymbol{k}) = \varepsilon_{2p} \pm t\sqrt{1+4cos^2\left(\frac{3k_xa}{2}\right)+4cos(\frac{\sqrt{3}k_ya}{2})cos(\frac{3k_xa}{2})} \quad \text{Eq. 2-4}$$

, where ε_{2p} is the energy $2p_z$ orbital, k_x, k_y are components of k vector in momentum space. We plot the band structure of graphene in Figure 2-1 and the zoom-in structure near k =0. One can find the band structure at the vicinity of k =0 can be approximated to a linear energy-momentum relation and is a zero-band gap semimetal due to inversion and time-reversal symmetry of graphene. The Hamiltonian and dispersion relation in Eq. 2-3 and Eq. 2-4 can be simplified to

$$H = \hbar v_F\boldsymbol{\sigma}\cdot\boldsymbol{k} \quad \text{Eq. 2-5}$$

and

$$E_\pm(k) = \varepsilon_{2p} \pm \hbar v_F|k| \quad \text{Eq. 2-6}$$

with $v_F = \frac{\sqrt{3}}{2}t = 1.1\times10^6 m/s$ the Fermi velocity in the graphene. The cone-like structure band structure means the electrons behave exactly the same as massless photons with reduced speed. This Hamiltonian has the same form as the Dirac equation so electrons in graphene are also called as massless Dirac Fermions.

The eigen-wavefunctions can be written as

$$|\mathrm{n}\boldsymbol{k}\rangle = \frac{1}{\sqrt{2}}\begin{pmatrix}-ine^{-i\theta_k/2}\\ e^{i\theta_k/2}\end{pmatrix} \quad \text{Eq. 2-7}$$

where $\theta_{\boldsymbol{k}}$ is the angle between$\boldsymbol{k}$and y-axis, and n is 1 for conduction band and -1 for valence band. This two-component wavefunction has the same form as the wavefunction of a spin-1/2 system, therefore this orbital degree of freedom is called pseudo-spin. In this analogy to spin system, the crystal momentum works as a magnetic field and the pseudo-spin is always pointing

parallel or anti-parallel to the momentum. Many electronic, optical properties of graphene are determined by this cone-like dispersion structure and the pseudospin of electrons states.[11,12]

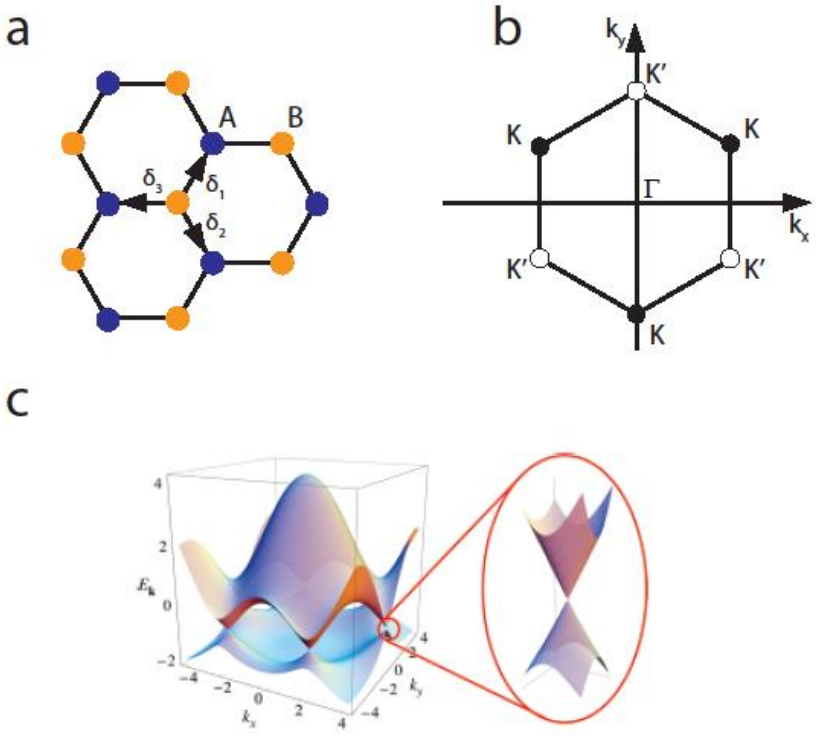

Figure 2-1 Monolayer graphene lattice and its band structure. a, Lattice structure of monolayer graphene. Each unit cell contains two carbon atoms: A sublattice (indicated by blue circles) and B sublattice (orange circles).δ_1,δ_2 and δ_3 are the vectors connecting nearest-neighbor carbon atoms.**b**, First Brillouin Zone of graphene. Filled and hollow dots represent the two inequivalent points K, K' at the corner of the first Brillouin Zone. **c**, The calculated band structure. The zoomed-in image on the right shows the linear band structure near the Dirac point, which is known as Dirac cone.

2.3 Optical Transitions in Graphene

We now incorporate the band structure of graphene with Fermi golden rule to understand its linear optical response.[7,8,11,13] In equilibrium graphene, direct interband transitions(Fig.2-2a) and indirect intraband transitions(Fig.2-2b) are typically the most important optical transitions to consider. There are also other proposed higher-order transitions(Fig.2-2c), but their effects are smaller and beyond the scope of discussion. [14] Here, we will discuss the optical response from interband and intraband transitions separately.

The two-dimensional optical conductivity $\sigma_g(\omega)$ describes the linear response of graphene and is the most important optical property to understand. $\sigma(\omega)$ can be related to permittivity by the following equations in SI unit if needed:

$$\sigma_{3d}(\omega) = \sigma_g(\omega)/d$$

$$\varepsilon(\omega) = \varepsilon_0\varepsilon_r + i\frac{\sigma_{3d}(\omega)}{\omega} \qquad \text{Eq. 2-8}$$

where σ_{3d} is the effective three-dimensional optical conductivity, d the thickness of graphene, ε_r the background permittivity.

2.3.1 Interband Transitions

The process of interband transitions involves an electron in the valence band absorbing a photon and reach a state in the conduction band and is shown in Fig.2-2a. Since the speed of light is much larger than the Fermi velocity, one can ignore the momentum of the absorbed photon and consider only the final state with the same momentum as the initial state. To figure out the effects from interband transitions, we calculate the response of graphene to an external electric field with the first order perturbation theory using Fermi's golden rule.[11]

We first consider an electromagnetic plane wave with electric field $\boldsymbol{E} = E_0\hat{\mathrm{x}}\cos\omega t$ incident at the normal onto a pristine graphene sheet with all valence states are filled and conduction states empty. Choosing the gauge so that the scalar potential φ = 0 and vector potential = $A_0\hat{\mathrm{x}}\mathrm{e}^{-\mathrm{i}\omega\mathrm{t}}$, so that the electric field $\boldsymbol{E} = -\frac{\partial \boldsymbol{A}}{\partial t} = i\omega\boldsymbol{A}$. The total Hamiltonian in the presence of electromagnetic field can be simply obtained by a substitution $\boldsymbol{k} \to \boldsymbol{k} + e\boldsymbol{A}$ with the band structure of graphene in Eq. 2-5. The interaction part of the Hamiltonian is described by:

$$H_{int} = ev_F\boldsymbol{\sigma}\cdot\boldsymbol{A} = \frac{ev_F}{i\omega}\sigma_x\frac{E_0}{\mathbf{2}}e^{-i\omega t} \qquad \text{Eq. 2-9}$$

The Fermi's golden rule states the transition probability for a transition from an initial state $|i\rangle = |v\ \boldsymbol{k}\rangle$ to the final state $|f\rangle = |c\ \boldsymbol{k}'\rangle$ with absorption of one photon is:

$$\frac{dw_{i\to f}}{dt} = \frac{2\pi}{h}|\langle i|H_{int}|f\rangle|^2\delta\left(\hbar\omega_{i\to f} - \hbar\omega\right) \qquad \text{Eq. 2-10}$$

wheref_i and f_f are the occupation fraction of initial and final state, respectively. With Eq. 2-7, one can find the matrix elements can be simplified to

$$|\langle i|H_{int}|f\rangle|^2 = \left(\frac{ev_FE_0}{2\omega}\right)^2\sin^2\theta_{\boldsymbol{k}}\,\delta_{\boldsymbol{k},\boldsymbol{k}'} \qquad \text{Eq. 2-11}$$

The total power absorbed from the incident wave can be written as

$$P = \sum_{i,f}\hbar\omega\frac{dw_{i\to f}}{dt}$$

$$= \hbar\omega\int\frac{4d\boldsymbol{k}}{(2\pi)^2}\left(\frac{ev_FE_0}{2\omega}\right)^2\sin^2\theta_{\boldsymbol{k}}\,\delta\left(\hbar\omega_{i\to f} - \hbar\omega\right) \qquad \text{Eq. 2-12}$$

where we take 2 spin and 2 valley degeneracy into account. After a lengthy but straightforward calculation and comparing with total incident power, one can obtain graphene absorption

$$\alpha_{gr}(\omega) = \frac{\frac{e^2 {E_0}^2}{8\hbar}}{\frac{\varepsilon_0 {E_0}^2}{2} c} = \pi\alpha \sim 2.3\% \qquad \text{Eq. 2-13}$$

This constant absorption coefficient of graphene is so-called "universal absorption". The experimental data shows the constant absorption ranges from mid-infrared up to 3eV where the saddle-point exciton effect comes into play and the linear band approximation breaks down. Another way to express total absorption power is using optical conductivity as

$$P = \frac{1}{2}\mathcal{R}e(\boldsymbol{j} \cdot \boldsymbol{E}^*) = \frac{1}{2}\mathcal{R}e(\sigma)|\boldsymbol{E}_0|^2 \qquad \text{Eq. 2-14}$$

Comparing this with Eq. 2-13, the corresponding real part of optical conductivity is

$$\mathcal{R}e(\sigma) = \frac{e^2}{4\hbar} \qquad \text{Eq. 2-15}$$

One interesting aspect of interband transitions is that the Fermi level determines whether the transition at specific energy is allowed or forbidden. A case with n-doped graphene is shown in Figure 2-2a.Transitions with photon energy $\hbar\omega < 2|E_F|$ are forbidden due to Pauli blocking effect while transitions with $\hbar\omega > 2|E_F|$ are still allowed. Therefore, one would expect that the absorption spectrum of graphene shows an onset at $2|E_F|$below which the absorption is blocked. The hole-doped side also retains the same behavior. To describe the Pauli blocking effect, one can write the interband contribution of optical conductivity in the following form:

$$Re(\sigma_g) = \frac{e^2}{4\hbar}\left[1 + \frac{1}{\pi}\left(tan^{-1}\frac{\hbar\omega - 2|E_F|}{\Gamma} - tan^{-1}\frac{\hbar\omega + 2|E_F|}{\Gamma}\right)\right]$$
$$Im(\sigma_g) = -\frac{e^2}{8\pi\hbar} ln\frac{(\hbar\omega + 2|E_F|)^2 + \Gamma^2}{(\hbar\omega - 2|E_F|)^2 + \Gamma^2} \qquad \text{Eq. 2-16}$$

whereΓ is interband broadening to describe the broadening effect including temperature, carrier lifetime and doping imhomogeneity. The imaginary part of optical conductivity is determined by Kramers-Kronig relation.

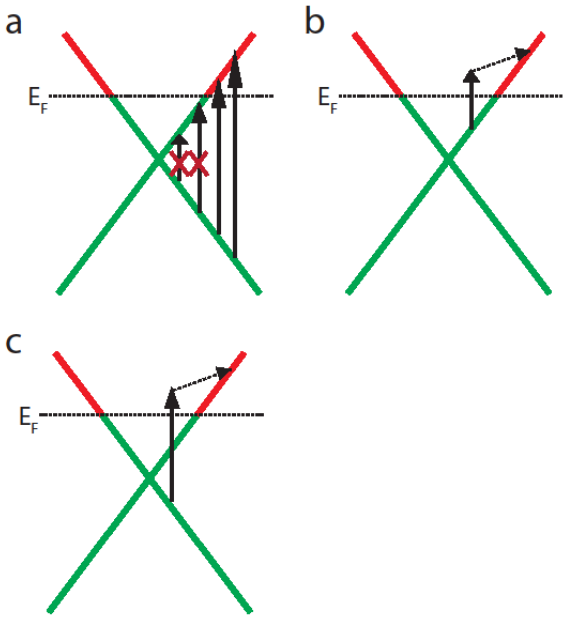

Figure 2-2 Optical transitions in graphene. a, Interband transitions from the filled states (green line) in the valence band to empty states (red line) in the conduction band. **b**, Intraband transitions from states below the Fermi level to above the Fermi level in the same band. **c**, Higher order of interband transitions from states below the Fermi level to above the Fermi level in different bands.

2.3.2 Intraband Transitions

Situating between electrical transport and optical interband transitions, graphene exhibit low-frequency intraband transitions. Intraband transitions are processes connecting the initial state and final state within the same band. The momentum mismatch between speed of light and Fermi velocity is satisfied by scattering off defects and impurities. The representation of intraband transitions are shown in Fig. 2-2b and involves an absorption of a photon and scattering by impurities or phonons. The spectroscopic study of intraband transitions in graphene can help us to understand free electron interaction with impurities. The intraband transitions are also called "free carrier response" and it electrical and optical properties are similar to those in simple metals. The free carrier response are usually examined on the basis of the Drude model. Here, we provide a semi-classical derivation of Drude behavior of graphene free electrons through Boltzmann equations. [14], [15], [15]–[17]

Consider a graphene piece in the presence of an electric field $\boldsymbol{E} = E_0\hat{\mathrm{x}}\exp(-i\omega t)$ and write the carrier distribution function$f(r,k,t) = f_0(r,k,t) + \delta f(r,k,t)$ where $f_0(r,k,t)$ is the distribution function in equilibrium and $\delta f(r,k,t)$ is the perturbation due to presence of electric fields. Since the $\delta f(r,k,t)$ is spatially uniform, the time-dependent Boltzmann equation reads:

$$\left(\frac{\partial f}{\partial t}\right)_{collision} = \frac{\partial f}{\partial t} + \dot{\boldsymbol{r}} \cdot \frac{\partial f}{\partial \boldsymbol{r}} + \dot{\boldsymbol{k}} \cdot \frac{\partial f}{\partial \boldsymbol{k}}$$
$$= \frac{\partial \delta f}{\partial t} - e\boldsymbol{E} \cdot \frac{\partial \varepsilon}{\partial \boldsymbol{k}} \frac{\partial f_0}{\partial \boldsymbol{\varepsilon}} \quad \text{Eq. 2-17}$$

In the relaxation time approximation, one assumes:

$$\left(\frac{\partial f}{\partial t}\right)_{collision} = -\frac{f - f_0}{\tau} = \frac{-\delta f}{\tau} \quad \text{Eq. 2-18}$$

where τ , which may be **k**-dependent, is the relaxation time between collisions with the impurity ions, defects and phonons. Solving the differential equation in Eq. 2-17 with relaxation time approximation, we obtain:

$$\delta f = \frac{eE_0 \boldsymbol{v_x}(\boldsymbol{k})}{1/\tau - i\omega} \frac{\partial f_0}{\partial \boldsymbol{\varepsilon}} e^{-i\omega t} \quad \text{Eq. 2-19}$$

The sheet current density in graphene can be expressed as

$$j_x = \frac{-e}{A} \sum_k f(k) \boldsymbol{v}_x(\boldsymbol{k}) = \frac{-e^2 E_0}{A} \sum_k \frac{\boldsymbol{v}_x^2(\boldsymbol{k})}{1/\tau - i\omega} \frac{\partial f_0}{\partial \boldsymbol{\varepsilon}} \quad \text{Eq. 2-20}$$

where *A* is the cross-section area. Noting that $\partial f_0/\partial \varepsilon$ is very small unless in the vicinity of the Fermi level, the integration is mainly contributed by wave vectors near the Fermi energy. This suggests that the transport and low frequency optical behaviors at low temperatures are dominated only by the electrons locating around the Fermi energy.

Now we can write the optical conductivity assuming $E_{\mathrm{F}} \gg kT$:

$$\sigma(\omega) = \frac{4e^2}{(2\pi)^2} \int_{-\infty}^{\infty} \varepsilon d\varepsilon d\theta \frac{v_F^2}{1/\tau - i\omega} \frac{-\partial f_0}{\partial \varepsilon}$$
$$= \frac{iD}{\pi} \frac{1}{\omega + i\Gamma} \quad \text{Eq. 2-21}$$

where $D = \frac{e^2 E_{\mathrm{F}}}{\hbar^2}$ is the Drude weight and $\Gamma = 1/\tau$ is the intraband broadening. The low-frequency intraband response of graphene is closely related to dc transport measurements and measurements of intraband responses can help us understand the impurities or phonon scattering process in graphene.[18]–[23]

2.4 Experimental Setup and Graphene Fabrication

In our study, we used Fourier-transform infrared spectroscopy (FTIR) to measure the transmission spectra of graphene samples over the range from 30 to 11000cm^{-1}(0.004 - 1.4eV) and deduce the frequency-dependent conductivity from the spectra. The gate-dependent spectra covers both interband and intraband transitions.

We used CVD graphene for this study because of an experimental consideration. To do reflection or transmission spectroscopy, the sample has to be larger than the light beam spot size which is determined by the wavelength and the effective numerical aperture. This is described by the diffraction limit of electromagnetic wave through equation:

$$D = \frac{1.22\lambda}{N.A.} \qquad \text{Eq. 2-22}$$

$\lambda$is the wavelength of light. Previously, infrared spectroscopy to probe a graphene monolayer was limited to >1000 cm^{-1} (wavelength <10 μm) because of the limited size of exfoliated graphene.[7,8,24,25] For spectroscopy at a longer wavelength up to ~300 μm, we need a large sample size. Here we used large-area graphene grown by chemical vapor deposition (CVD).

2.4.1 Graphene Fabrication and Gating

Graphene monolayers can be created or isolated through different ways, but by far the most popular way to create large area single crystalline or poly crystalline is by using a process called chemical vapor deposition(CVD). CVD is a method which can produce relatively high quality graphene, potentially on a large scale.

We followed the growth procedure developed by Ruoff group.[26] Graphene films were grown on thick copper foils in a high temperature furnace with CH_4 and H_2 mixture gas. To achieve large area single crystalline domain, we first annealed the copper foil in hydrogen atmosphere at 1000ºC to remove copper step edges and reduce number of seeds on the surface. Then a mixture of H_2/CH_4 was introduced into the system to initiate the graphene growth. After a continuous graphene layer was formed on copper foil, the system was cooled down to room temperature.

We then transferred with PMMA support to a Si/SiO_2 wafer after wet-etching to remove the copper film by $FeCl_3$. After dissolving the PMMA in acetone solution, high-quality graphenes of cm size on the various substrates were obtained. (Fig.2-3a) Raman spectra (Fig.2-3b) show that the sample was indeed monolayer graphene. Subsequently, Au/Ti electrodes (thickness ~ 50 nm) were deposited in vacuum through stencil masks onto the graphene sample for electrical measurements.

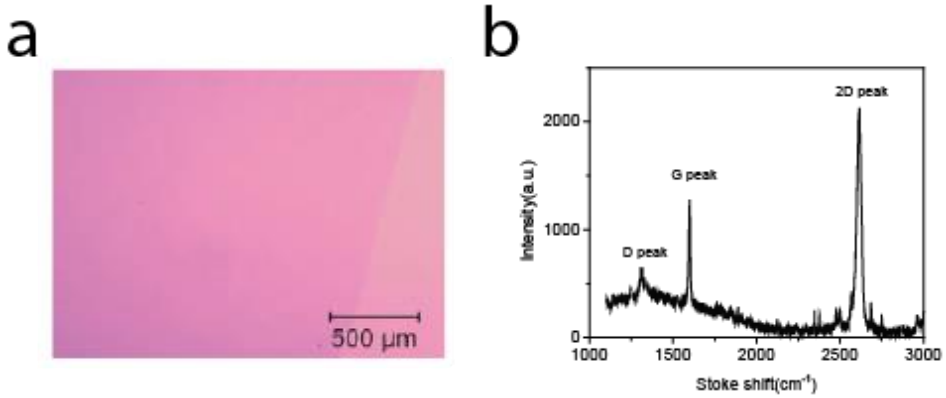

Figure 2-3 Chemical vapor deposition(CVD) graphene transferred on 300nm SiO_2/Si wafer. a, Optical image of the CVD graphene. **b,** Raman spectrum to confirm that the sample was indeed monolayer graphene.

The benefits of using CVD to deposit materials onto a substrate are that the quality of the resulting materials is usually very high. Other common characteristics of CVD coatings include imperviousness, high purity, fine grained and increased hardness over other coating methods. It is a common solution for the deposit of films in the semiconductor industry, as well as in optoelectronics, due to the low costs involved compared to the high purity of films created.

For electrostatic gating, we employed three different methods for the situations needed: silicon back gate, ion gel gating and aqueous solution gating. Silicon back gate with dielectric material is widely used in conventional two dimensional electron gases to create field-induced carriers. And, it can typically generate concentration up to ~ 10^{12}cm^{-2} without semicondcutor dielectric breakdown, but this method can be applied even in low temperatures. Ion gel gating, on the other hand, can be gated much more efficiently to over 10^{13}cm^{-2} because of its excellent chemical stability and compatibility with different gating configurations.[27] However, the ions in ion gel can be frozen at low temperatures and reduce the application in low temperature regime. Aqueous solution gating can also go to high doping concentration and is only limited by the electro-chemical reaction of graphene and water at around ±1V. In addition. Aqueous solution gating is compatible with biological systems and could have potential bio-engineering applications. [28]

2.4.2 Local Field Correction

In order to understand the intrinsic frequency-dependent conductivity of graphene, we develop a Matlab program to eliminate the optical effect from the substrates.

The frequency-dependent conductivity change of graphene $\Delta\tilde{\sigma}$ at different gate voltages is obtained from the measured transmission spectra using a perturbation treatment, because a monolayer graphene only absorbs a small fraction of the light. Within this approximation, the complex AC conductivity change is related to the difference transmission spectra by

$$\frac{-\Delta T}{T}(\omega) = \frac{4\pi}{c} Re(\Delta\tilde{\sigma} \times L) \qquad \text{Eq. 2-23}$$

where $-\Delta T/T$ is the normalized transmission difference, L the local field factor, and $\Delta\tilde{\sigma}$ the gate-induced conductivity change in graphene.

For suspended graphene, the local field factor is one and we obtain the well know form of

$$\frac{-\Delta T}{T}(\omega) = \frac{4\pi}{c} Re(\Delta\tilde{\sigma}) \qquad \text{Eq. 2-24}$$

.[8] For graphene sitting on a substrate one needs to consider the local field effect. For example, consider the case where graphene is sitting on a SiO_2/Si substrate. The local field factor L is uniquely defined by the refractive index of Si and SiO_2, as well as the thickness of SiO_2, and it can be determined accurately without any adjusting parameters. Specifically, L has the form

$$L = 1 + r_{ag} + t_{ag} r_{gs} t_{ga} \frac{e^{2inkd}}{1 - e^{2inkd} r_{gs} r_{ga}} \qquad \text{Eq. 2-25}$$

where r_{ag}, r_{gs} and r_{ga} are the Fresnel reflection coefficients at air-silica, silica-silicon and silica-air interferences, t_{ag} and t_{ga} are the corresponding transmission coefficients, n and d are complex reflective index and thickness of the SiO_2 layer, respectively, and k is the wavevector of the incident light.

The real and imaginary part of AC conductivity, σ' and σ'', is connected by Kramers-Kronig (K-K) relation

$$\sigma''(\omega) = \frac{-2\omega}{\pi}\int_0^\infty \frac{\sigma'(\bar{\omega})d\bar{\omega}}{\bar{\omega}^2-\omega^2} \qquad \text{Eq. 2-26}$$

Because the K-K relation holds true for all the gate voltages, the gate-induced conductivity change $\Delta\sigma = \Delta\sigma' + i\Delta\sigma''$ also satisfies the same K-K relation. Making use of the Eq. 2-23 and the K-K relation, we obtain both the real and imaginary part of the gate-induced AC conductivity from infrared transmission spectra. The Matlab program we developed can iteratively apply Eq. 2-23 and Eq. 2-26 to eliminate the optical effect from the substrates and achieve intrinsic optical conductivity of graphene.

2.5 Interband Transitions in Graphene Optical Spectrum

Graphene, a single layer of honeycomb carbon lattice, exhibits many exotic behaviors, ranging from the anomalous quantum Hall effect [1], [2] and Klein paradox [3] to coherent transport[21]. In contrast to the extensive effort on electrical transport, optical study of graphene has been limited.[7,8,24,25,29] Such optical investigation is important for understanding the electronic structures and excited-state properties of low-dimensional materials.

We have used infrared (IR) spectroscopy to probe interband optical transitions in monolayer graphene. Unlike conventional materials, the optical transitions in graphene can be dramatically modified through electrical gating: The normalized gate-induced changes in transition strengths approach the order of unity. Although field-effect–modulated electrical conductivity has long been the basis of modern electronics, such large modification of optical transitions by electrical gating is unusual. For comparison, relative refractive index change in typical electro-optical materials rarely reaches 10^{-3}. The special behavior of graphene is due both to its two-dimensional (2D) structure that confines electrons in one atomic layer and to its low density of states (DOS) near the Dirac point, which causes the Fermi energy (E_F) to shift significantly with variation of carrier density.

The strong gate dependence of optical transitions allows detailed examination of graphene band structure. We observed the linear Dirac band in graphene monolayer and were able to determine through direct optical means the band dispersion. Aside from such fundamental interests, the very unusual optical properties of graphene make it a promising material for IR optoelectronics. This is particularly attractive considering that graphene possesses superior carrier mobility, current carrying capability, and thermal conductivity, and can readily incorporate electrical coupling as in field-effect devices[8] and pn junctions.[29,30]

Here, we used Fourier-transform infrared spectroscopy (FTIR) to measure the transmission spectra of CVD graphene samples for photon energy from 0.4 to 1.4eV.[31] We control the Fermi energy of graphene samples through electrical doping using efficient ion gel gating. Figure 2-4a displays the schematic of a typical device. The carrier concentration in graphene is controlled by the top gate voltage V_g, and doping dependence of electrical transport and optical transmission are measured on the same graphene devices. Figure 2-4b shows the electrical resistance curve of a typical device, which has a charge neutral point (CNP) at 1.2 V. The resistance decreases from the CNP value upon both electron and hole doping. A lower resistance, corresponding to a higher carrier concentration and larger shift of Fermi energy, is achieved in the hole-doping region, which will be the focus of our study.

The features in the transmission spectra from 0.4 to 1.4eV are dominated by the Pauli blocking effects of interband transitions. Figure 2-4c displays gate-induced change in transmission spectra, $(T-T_{CNP})/T_{CNP}$, at different gate voltages. The spectra exhibit distinct step-like behavior, with increased transmission of photons below the threshold energy $2|E_F|$, from which we determine Fermi energy E_F and carrier concentration $n = (E_F / \hbar v_F)^2 / \pi$ where v_F is the Fermi velocity. With ion gel gating vertical electronic transitions with excitation energy as high as 1.8eV can be blocked here, the highest value achieved in graphene so far. It correspond to an electrically induced carrier concentration of $6\times10^{13}/cm^2$.

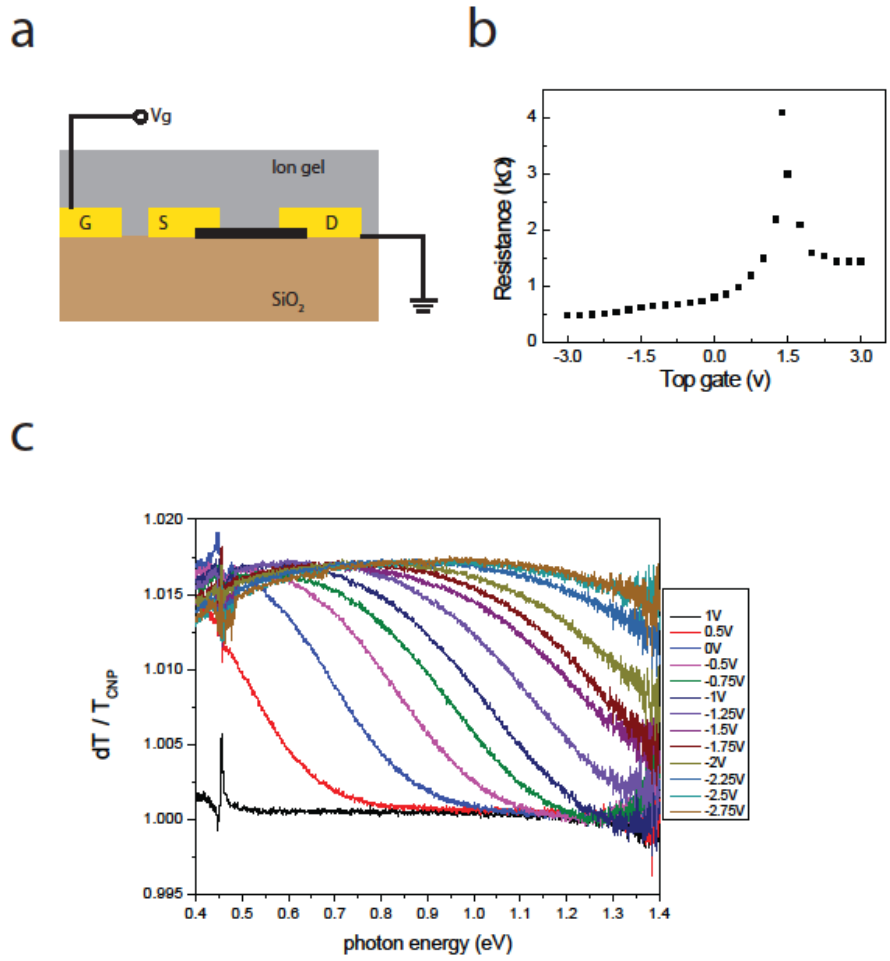

Figure 2-4 Controlling the optical transitions in graphene with ion gel gating. a, Illustration of an ion gel gated graphene on a SiO_2 substrate. **b,** Graphene resistance as a function of gate voltage V_g, which has a maximum at charge neutral point V_{CNP} = 1.2 V. The largest resistance decrease, corresponding to the highest carrier density, occurs at V_g = -3V with hole doping. **c,** Optical transmission spectra change, $(T\text{-}T_{CNP})/T_{CNP}$, when V_g–V_{CNP} is varied from -0.25 to -4V at 0.25V steps. Increased optical transmission takes place for optical excitation energies below $2|E_F|$, which increases with gating strength. $2|E_F|$ value up to 1.8 eV is achieved using the ion gel gating.

2.6 Drude Conductivity of Dirac Fermions in Graphene

Quantum theories of electron dynamic response in graphene have been developed by several groups[21,23,32]. They predict that, within the framework of Boltzmann transport theories, high frequency conductivity of monolayer graphene has a Drude form shown in Equation 2-21. The prefactor D, known as the Drude weight, has the value

$$D = \frac{v_F e^2}{\hbar}\sqrt{\pi|n|} \qquad \text{Eq. 2-27}$$

when electron-electron interactions are neglected, with $v_F = 1.1\times10^6 m/s$ being the Fermi velocity[2] and |n| the carrier density. This is distinctly different from classical materials where

$$D = \frac{\pi n e^2}{m^*} \qquad \text{Eq. 2-28}$$

The predictions on graphene Dirac fermion dynamics have never been directly tested experimentally. In fact, it was suggested from measurements of interband transitions[7] that *D* could deviate from the predicted value. There are also theoretical studies showing that electron-impurity interactions could result in carrier dynamics in graphene beyond the Boltzmann description[33,34], and that inclusion of electron-electron interactions could dramatically reduce the Drude weight *D*[15].

We report spectroscopic measurements of graphene conductivity from terahertz to mid-IR for different electron and hole concentrations. We confirm that the conductivityfrom free-carrier response indeed has a Drude-like frequency dependence. In addition, we have been able to determine the Drude weight *D* and scattering rate Γ of doped graphene directly and separately for the first time. We observe an electron-hole asymmetry for *D,* and find that values of *D* is lower than the theoretical prediction in equation 2-21[18,21,23]. This reduction of Drude weight (arising from free carrier intraband transitions) is connected to corresponding changes in interband transitions[7], [8], and we demonstrate that the sum rule requiring the integrated intraband (Drude) conductivity and interband conductivity to be a constant is well obeyed.

Black dots in Fig. 2-5(e) show the DC conductivity as a function of the gate voltage in a typical graphene sample. The minimum conductance occurs at 14V, which defines the charge neutral point (CNP) of the sample. Carrier density in graphene is related to the gate voltage by n = 7.5×10^{10} (V_{cnp}-V_g) $cm^{-2}V^{-1}$ [2], where negative (positive) density corresponds to electron (hole) doping. To double-check this relationship, carrier concentration is also measured by infrared spectroscopy method developed from Ref. [7], in which we identify the onset energy of interband absorption at $2E_F$ at different gate voltage and then compute the concentration by $E_F = \hbar v_F \sqrt{\pi |n|}$. The carrier density obtained from two different methods shows that systematic error for the carrier concentration is less than 5%.The sample had an initial hole doping of 1.05×10^{12} cm^{-2} at $V_g = 0$, and a hole mobility around 2700 $cm^2/V.s$. As seen from Fig. 2-5(e), the DC conductivity for hole doping is reasonably linear with $|n|$, and there is a large asymmetry between electron and hole conductivity at the same $|n|$. In previous studies, conclusions have frequently been made on carrier scattering from such DC conductivity data based on $\sigma_{DC} = D/\pi\Gamma$ and the assumption in Eq. 2-27 holds exactly as theory predicts[23-25]. However, the validity of this approach has never been tested.

An independent determination of *D* and Γ can be achieved through AC conductivity measurements using IR spectroscopy. The gate-induced change of AC conductivity (referred to CNP value), $\Delta\tilde{\sigma} = \tilde{\sigma} - \tilde{\sigma}_{cnp}$, can be obtained readily from the difference IR absorption spectra. Fig. 2-5a and Fig. 2-5b show the real part of the AC conductivity change $\Delta\sigma'$ in the low-wavenumber range (<450 cm^{-1}) for different electron and hole concentrations. In this spectral range free carrier response (i.e., an increase in conductivity with carrier density)

dominates, providing direct information on Dirac fermion electrical transport. The complete set of $\Delta\sigma'$ spectra in Figs. 2-5a and 2-5b can be fit (dashed line) by $\Delta\tilde{\sigma}(\omega) = iD/\pi(\omega + i\Gamma) - iD_{cnp}/\pi(\omega + i\Gamma_{cnp})$ using the Drude form for $\tilde{\sigma}$ and $\tilde{\sigma}_{cnp}$. A finite charge neutral point response (D_{cnp} and Γ_{cnp}) accounts for inhomogeneous electron and hole puddles present in graphene. In the fittings, we set Γ_{cnp} equal to that when graphene is weakly doped. The value of D_{cnp} is set so that $D_{cnp}/\pi\Gamma_{\mathrm{cnp}}$ gives the DC conductance at the charge neutral point. From the Drude fits, we obtain directly the scattering rate Γ and Drude weight D as a function of electron and hole concentrations, shown as symbols in Fig. 2-5c and Fig. 2-5d, respectively.

Note that the gate-induced infrared absorption from the p-doped Si substrate is negligible. Real part of hole AC conductivity in silicon is described by

$$\sigma' = \frac{ne^2}{m_h}\frac{\Gamma}{\Gamma^2+\omega^2} \qquad \text{Eq. 2-28}$$

For the same carrier density, it is more than one order of magnitude smaller than graphene conductivity across the experimental spectral range (30 cm^{-1} <ω< 6000 cm^{-1}) due to the large hole effective mass (m_h= 0.36 m_0) and small scattering rate (Γ ~ 4 cm^{-1} at 100 K) [35].

From the values of D and Γ extracted from the IR spectroscopy, we can obtain $\sigma_{DC}(=D/\pi\Gamma)$ of graphene at different carrier concentrations [red dots in Fig. 2-5e]. It agrees nicely with the directly measured DC conductivity in our sample for all gate voltages (black dots). This agreement provides a consistency check of the Drude description.

We now compare our experimentally determined Γ and D to theory predictions. Fig. 2-5c shows that Γ is roughly a constant at different hole concentrations, while it is higher in value and increases with the carrier concentration for electron doping. This electron/hole concentration dependence of Γ is not predicted by theory, and cannot be described by pure unitary scattering or charge impurity scattering of Dirac fermions[17]. A combination of different scattering mechanisms seems to be necessary to explain the observation.

While theoretical prediction on Γ may vary depending on the scattering mechanisms assumed, the same theoretical value for the Drude weight[36] is always obtained when electron-electron interactions are neglected. Comparison of non-interacting theory (blue line) and experiment (black symbols) in Fig. 2-5d, however, shows an appreciable difference. In the strongly doped region ($|V_g-V_{cnp}|$>20 V) where the Boltzmann theory is supposed to be most reliable, the measured D is lower than the theoretical value by 20-45%. (The experimental uncertainty is less than 10%.). An electron and hole asymmetry is also present in the measured D.

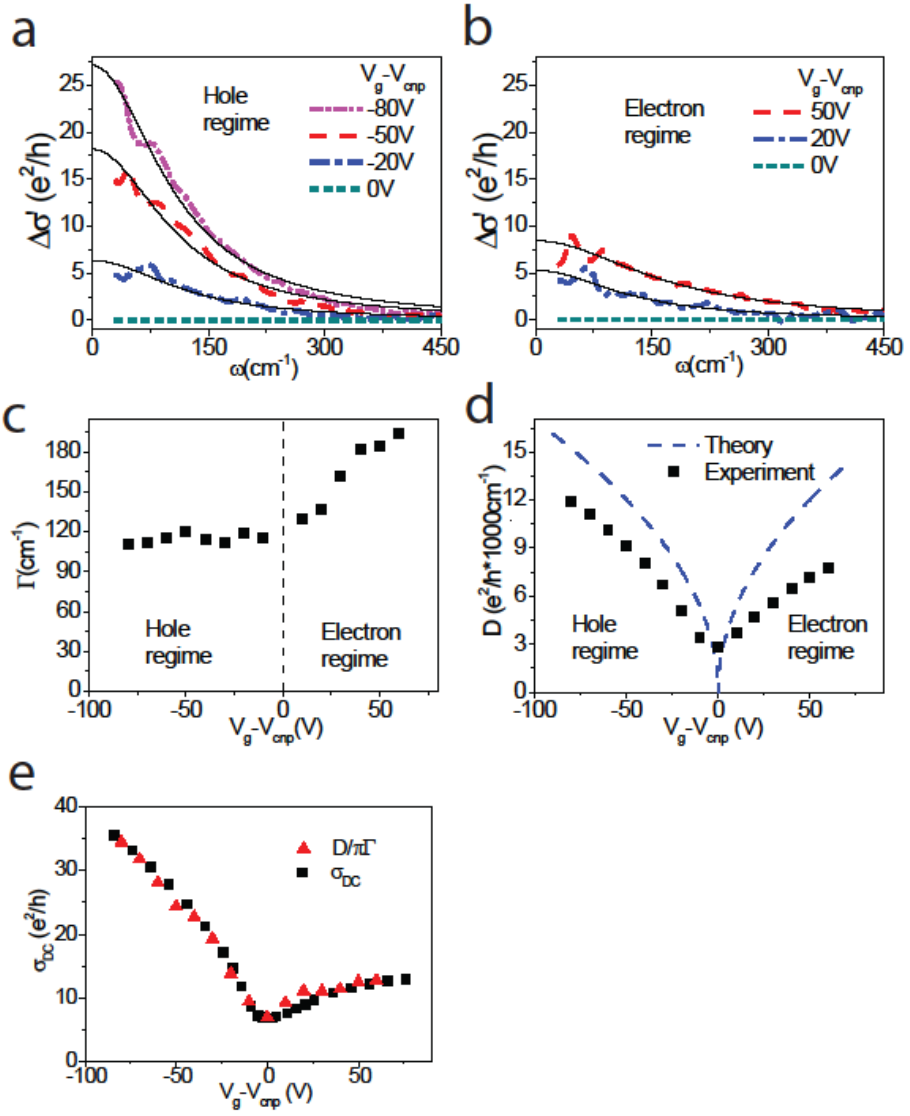

Figure 2-5 Free-carrier responses in graphene. a, b,Gate-induced change of AC conductivity $\Delta\sigma'$ in hole- and electron-doped graphene, respectively, for 30 $cm^{-1} < \omega < 450$ cm^{-1} (dashed lines). The frequency dependence of AC conductivity can be fit by the Drude model (solid lines). **c**, The scattering rate Γ and ,**d**, Drude weight D at different electron and hole concentrations. Surprisingly, the Drude weight is substantially lower than theoretical predictions based on the Boltzmann transport theory (blue line in (**d**)) and shows an electron-hole asymmetry. **e,** DC conductivity in the form of $D/\pi\Gamma$ obtained from the Drude fit of terahertz/far-IR measurements (triangles) agrees well with the values from direct DC transport measurements (squares).

2.7 Sum Rule in Graphene Optical Response

Fig. 2-6a and 2-6b show the optical conductivity difference (referred to CNP) at different hole and electron concentrations in the spectral range 600-6000 cm^{-1}. A gated-induced decrease in optical conductivity is clearly present from zero to a cut-off frequency of $2E_F/\hbar$ that increases with carrier doping, as the theory predicts. However, the observed interband optical conductivity decrease in doped graphene is appreciably less than σ_0 (dashed lines in Fig. 2-6a and 2-6b)

The general sum rule for oscillator strengths in solids state that the integrated conductivity over all frequencies is a constant. In the case of non-interacting free carriers described by prevailing graphene theories, the integrated intraband absorption increases by

$$\int \Delta\sigma'_{intra} d\omega = \frac{D}{2} = \frac{v_F e^2}{2\hbar}\sqrt{\pi|n|} \qquad \text{Eq. 2-29}$$

upon carrier doping. This increase is compensated exactly by an integrated interband absorption

$$\int \Delta\sigma'_{inter} d\omega = \sigma_0 \frac{2E_F}{\hbar} \qquad \text{Eq. 2-30}$$

with $E_F = \hbar v_F\sqrt{\pi|n|}$ and $\sigma_0 = e^2/4\hbar$[11], [23], [37]. In our case, the sum rule is still valid, and the observed anomalous reduction of Drude weight in intra-band transitions should be accompanied by a corresponding change in interband transitions at large wavenumbers. Fig. 2-6a and Fig. 2-6b show the optical conductivity difference (referred to CNP) at different hole and electron concentrations in the spectral range 600-6000 cm^{-1}. A gated-induced decrease in optical conductivity is clearly present from zero to a cut-off frequency of $2E_F/\hbar$ that increases with carrier doping, as the theory predicts. However, the observed interband optical conductivity decrease in doped graphene is appreciably less than σ_0 [dashed lines in Fig. 2-6a and 2-6b], and the deviation is larger for electron doping compared with hole doping. This reduction in gate-induced absorption decrease, as well as electron-hole asymmetry in interband transitions, matches well with the reduction in gate-induced absorption increase and electron-hole asymmetry in intraband Drude weight. To be more quantitative, we plot in Fig. 2-6c the absolute values of integrated conductivity change for interband transitions (black symbol) and intraband transitions (red symbol, which is proportional to the Drude weight change) at different carrier doping. The two agree almost perfectly, just as the sum rule requires. A reduction of gate-induced interband absorption has also been observed previously for mechanically exfoliated graphene[7]. Based on the sum rule that we established experimentally, it indicates that the anomalous Drude weight reduction is general for both exfoliated and CVD samples.

This reduction of Drude weight cannot be easily understood. One theoretical study showed that electron-electron interactions in graphene could lead to a reduced Drude weight[33]. However, this theory predicted a much larger reduction of the Drude weight (over 80%) for graphene on SiO_2 than what we have observed. It is also possible that reduction of D is a

consequence of defects-induced electron or hole localization, which decreases the effective 'free' electron or hole concentration. In addition, the electron-impurity interactions may play a role and contribute to the observed electron-hole asymmetry[34]. Further experiments with higher quality graphene will be required to pin down the underlying mechanism for the Drude weight reduction.

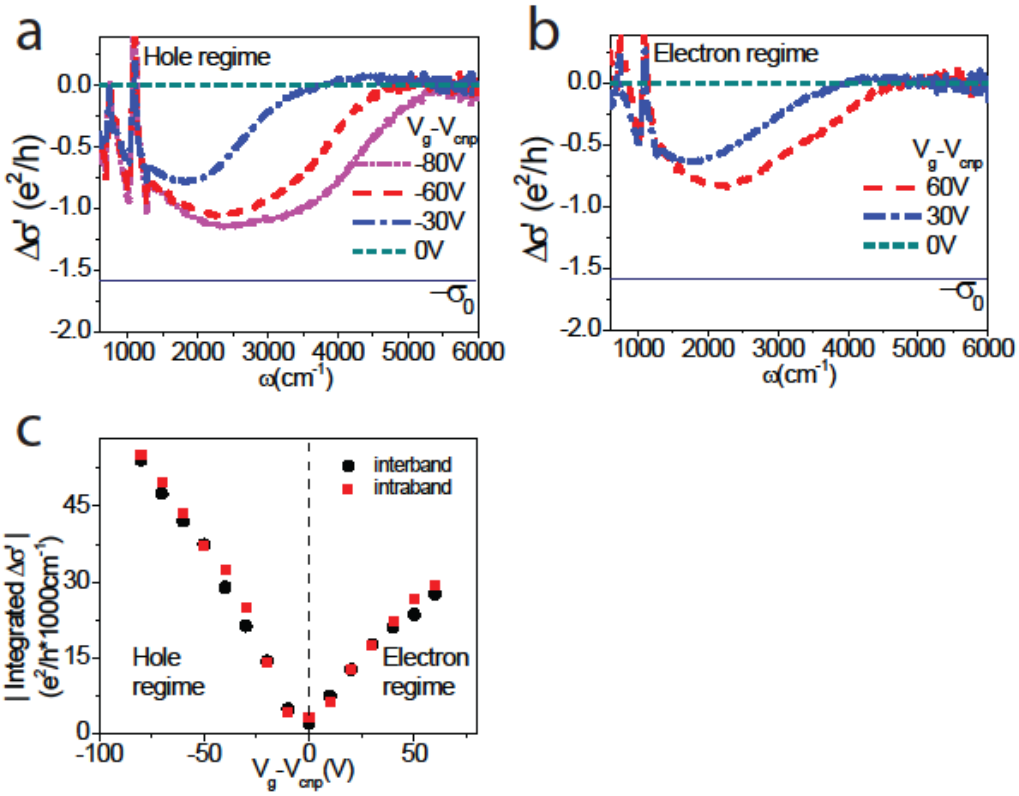

Figure 2-6 Sum rule in graphene. a,b, Gate-induced change of interband AC conductivity $\Delta\sigma'$ in hole- and electron-doped graphene, respectively, over 600 $cm^{-1} < \omega < 6000\ cm^{-1}$. The AC conductivity decreases due to empty initial states (hole doping) or filled final states (electron doping) for interband transitions below $2E_F$. (The sharp features around 1200 cm^{-1} are extrinsic and arise from SiO_2 phonon resonances of the substrate). Observed interband conductivity decrease is appreciably less than the theoretical predicted value of $\pi e^2/2h$ (horizontal dashed line), and shows electron-hole asymmetry. **c,** Upon charge carrier doping, integrated conductivity change has an increase from intraband transitions (squares) that equals the decrease from interband transitions (circles). The two values agree quantitatively at all gate voltages, as required by the oscillator strength sum rule.

2.8 Summary

We understand the graphene optical transitions including both interband and intraband transitions through both theoretical and experimental methods. The graphene electronic structure is derived by the tight-binding model and the optical conductivity is calculated by the Fermi golden rules. We employ fourier-transformed infrared spectroscopy from 30 to 11000 cm^{-1} to confirm the gate-dependent optical conductivity of graphene. Combining the contributions from both interband and intraband transitions in graphene, the optical conductivityσ_g at different Fermi energies (E_F) can be written by[38]

$$Re(\sigma_g) = \frac{e^2}{4\hbar}\left[1 + \frac{1}{\pi}\left(tan^{-1}\frac{E - 2|E_F|}{\Gamma} - tan^{-1}\frac{E + 2|E_F|}{\Gamma}\right)\right] + \frac{e^2}{\pi\hbar\tau}\frac{|E_F|}{E^2 + (1/\tau)^2}$$

$$Im(\sigma_g) = \frac{e^2E}{\pi\hbar}\frac{|E_F|}{E^2+(1/\tau)^2} - \frac{e^2}{8\pi\hbar}ln\frac{(E+2|E_F|)^2+\Gamma^2}{(E-2|E_F|)^2+\Gamma^2} \quad \text{Eq. 2-31}$$

where E is the incident photon energy, Γ and $1/\tau$ are the interband and intraband transition broadening, respectively.

Chapter 3

Broadly Tunable Infrared Light Source for Molecular Vibrational Spectroscopy

3.1 Introduction

For many years, the infrared region of the spectrum has been of great interest to researchers both in chemistry and material science. One particular important region is the mid- to far-infrared frequency region from about 100 to 3900 cm^{-1}, where the typical molecular vibration and phonon modes are sitting in. The optical absorption of these modes not only provides a general means for chemical compound detection, but also offers various methods to scrutinize the details of the molecular structure such as defects, stacking order, orientation, etc. For a long time, the research in this area was hampered by the low spectral brightness of blackbody sources. This problem has been changed dramatically with the commercialized Fourier transform infrared spectrometers due to their multiplex origin to overcome the low source intensity problem.

Nonetheless, the advance in infrared laser light source is still an active area in physical and chemical research. Not only the infrared laser creates a bright light source to enable fast detections for dynamics study, but also the coherent property of laser can be applied for different techniques, for example in the cavity ring-down spectroscopy[39]. With the development of femto-second pulsed laser, one can also exploit the temporal resolution to achieve pump-probe spectroscopy or even 2D IR echo spectroscopy[40]. The generation of coherent mid- to far-infrared light source then becomes a field of interest in the optical physics community.

There are several methods to generate infrared laser source currently. Materials with bandgap at mid-infrared, such as PbSSe and PbSnTe, have been demonstrated to lase at cryogenic temperature[41]. However, the lasing condition becomes unstable at room temperature operation. Quantum cascade laser(QCL), achieving lasing through the intersubband transitions from a repeated stack of semiconductor multiple quantum well heterostructures, is another promising candidate[42]. The structure of heterostructures in QCL can be designed to emit in the mid- to far-infrared spectrum, but its tunability is usually limited for each chip.

The parametric down-conversion provides a simple solution to create strong, ultrafast and tunable infrared laser[43,44]. Wavelength conversion of laser beams in down-conversion is an effective method to generate wavelengths outside the range of available laser materials since the available wavelength range is usually determined by the transparent window of the

nonlinear crystal. In this chapter, we introduce the working principle of our home-built DFG and synchronously pumped OPO setup and characterize the light source we generate.

3.2 Difference Frequency Generation (DFG)

Difference frequency generation (DFG) is a optical parametric down conversion process that involves combining two photons of different energiesω_p, ω_s to produce a third photonω_i whose energy equals the difference between those of the incident photons. Conventionally, the incident beams with higher photon energy is called as pump beam and the lower one is called as signal beam. The generated third beam is called as idler.

3.2.1 Working Principles of Difference Frequency Generation

The DFG process can occur when lights traveling in a nonlinear crystal where the nonlinearity $\chi^{(2)}$ exhibits. Only crystal materials lacking inversion symmetry can exhibit a nonlinearity $\chi^{(2)}$, so the DFG is usually generated in such a crystal. Lithium niobate ($LiNbO_3$) and lithium tantalate ($LiTaO_3$) are the commonly used crystals since they have relatively strong nonlinearity although the damage threshold is relatively low. The photorefractive damaging effects depends strongly on the material composition and therefore can be mitigated via MgO doping. Other nonlinear material like potassium titanyl phosphate (KTP, $KTiOPO_4$) and lithium triborate(LBO) have their own advantages and sometimes are used for noninear optics. For mid-infrared and tera-hertz generations, the crystal materials need to be transparent in the infrared spectral region. The important crystals for this purpose are silver gallium sulfide and selenide ($AgGaS_2$ and $AgGaSe_2$) and gallium selenide (GaSe).

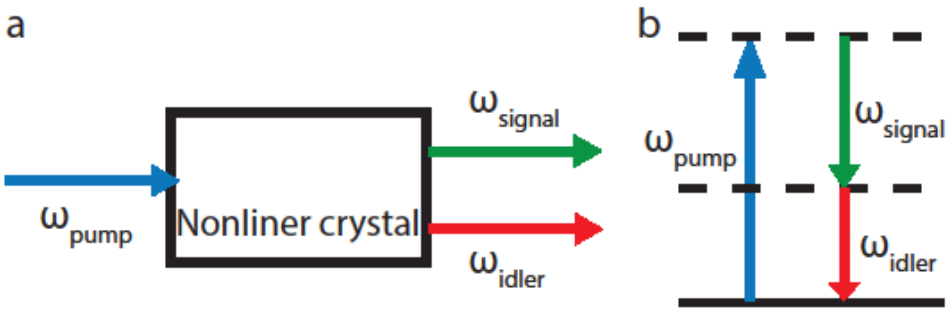

Figure 3-1 Schematic of optical parametric down conversion process. a, Optical parametric down conversion process converts an input pump waveω_p into two outputs, the signalω_s and idlerω_i, through the nonlinear effect in a birefringent crystal. **b,** Energy conservation of the optical parametric down conversion.

As shown in Figure 3-1,the optical parametric down conversion process converts an input pump waveω_p into two outputs, the signalω_s and idlerω_i. For efficient energy transfer, two important conditions have to be met simultaneously. First condition shown in Equation 3-1 is the energy conservation, which means the generated photon energy will be the difference between the two

input photons. The second condition shown in Equation 3-2 is the phase matching condition, meaning the previously generated beam needs to be in phase with newly generated beam for coherent add-up through the length of the crystal. For efficient down-conversion, we want pump, signal and idler beams propagating through the crystal at the same velocity and maintaining their relative phases.

$$\omega_{pump} = \omega_{signal} + \omega_{idler} \quad \text{Eq. 3-1}$$

$$k_{pump} = k_{signal} + k_{idler} \quad \text{Eq. 3-2}$$

This implies that the index of refraction of the three beams is the same since k=nw in a crystal. However, this condition is not easily achievable under most cases due to the refractive index dispersion of the crystals. Since $\omega_{pump} > \omega_{signal} > \omega_{idler}$, the dispersion relation usually indicates that $n_{pump} > n_{signal} > n_{idler}$. This will lead to gradual build-up of the phase difference between the previously generated beam and the newly generated beam, and once the phase reaches π, the output beams are going to destructively interfere with each other and produce a smaller output.

One traditional way to achieve phase matching is using optical birefringence of anisotropic crystal. Since the extraordinary refractive index is usually larger than the ordinary refractive index. one can make one or two beams polarized at the extraordinary axis and the others polarized at the ordinary axis. In this scheme, the Eq. 3-1 and Eq.3-2 could be both satisfied when one make an appropriate choice of crystal angle, light polarization and direction of propagation. Under such circumstance, the destructive interference due to phase mismatching is diminished and therefore an efficient down-conversion process can be generated. However due to the sensitivity of the refractive index with respect to polarization direction and temperature, the phase matching condition is only met at critical angles and complicates the alignment and tuning procedure. As a compromise, a short crystal is usually used to ease the phase matching, while the length of the crystal becomes the limiting factor of the conversion efficiency.

3.2.2 Experimental Setup of DFG and Characterization

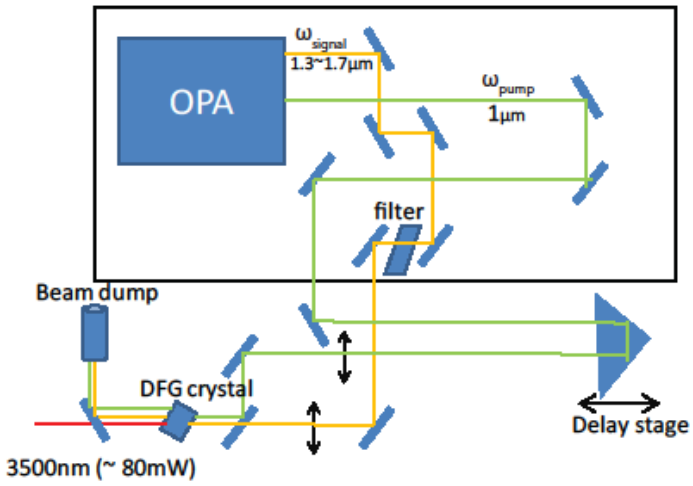

Figure 3-2 Experimental optical paths in our DFG system. The pump beam(1028nm, green line) and signal beam(1.3-1.7μm, yellow line) are sent into a lithium niobate crystal with correct time delay and polariztions. The idler beam(red line) at 2.4 - 4.7μm then can be created.

Figure 3-2a shows a schematic of detailed optical paths in our DFG system. The infrared radiation is generated by a femtosecond laser source. Specifically, an amplified femtosecond laser system (Pharos, Light Conversion Ltd) delivers laser pulses at 1028nm with a pulse duration of260fs and a repetition rate of 150KHz. We take 1W of 1028nm beam to use as pump beam in our DFG system. After going through a delay stage, a f=50cm focusing lens and a half-waveplate for tuning its polarization, the pump beam is sent into a nonlinear crystal to generate DFG.

The rest of 1028nm laser pumps a broadly tunable optical parametric amplifier (Orpheus OPA, Light Conversion Ltd) covering wavelengths from 600 nm-2200 nm. This OPA is used as the signal beam in our DFG setup. For the DFG generation within in 2.4 - 4.7μm, we can tune the OPA output from 1320nm to 1780nm to match the energy conservation relation. The signal beam is sent into a filter to remove unwanted spectral range and a f= 20cm lens to focus on the nonlinear crystal. The pump and signal beam are combined using a dichroic mirror which reflects 1028nm pump light while transmits the signal beam.

The mid-infrared(2.4 - 4.7um)idler are generated by mixing the pump laser (1028nm) and the OPA output through difference frequency generation. We choose a 2mm thick lithium niobate(LiNbO3) as our nonlinear crystal since the transparent regime is between 350 and 5200nm which transmits all pump, signal, and idler beams. At the same time, lithium niobate is known to have high seconed-order nonlinearity therefore we can generate down-

conversion process with relative low power. The pump and signal beam are set to have nice spatial overlap by both aligning them through two faraway apertures and mounting the focusing lens on translational stages to fine tune their beam waist at crystal. The temporal overlap is determined by sending both beam to a known BBO crystal to monitor the sum frequency generation. We fine tune the delay stage the maximize the sum frequency generation to achieve nice temporal overlap.

In order to satisfy the phase matching condition in equation 3-2, one needs to send input beams with correct polarization and set the nonlinear crystal at a specific angle. For our DFG crystal, we choose type II scheme where the pump beam is in the extraordinary polarization while the signal and idler are in the ordinary polarization. An half-wave plated then is inserted in the pump beam to rotation its polarization such that it is 90degree compared to the signal beam. We then rotation the lithium niobate crystal to search for phase matching condition by monitoring the output power at idler frequency. The monitoring is done with putting a dichroic mirror in front of a pyro-electric power meter to remove pump and signal beam.

The conversion efficiency of DFG can be estimated through the couple-wave equation with plane-wave approximation[45], [46]and have the following form:

$$G = \frac{P_s(z) - P_s(0)}{P_s(0)} = \frac{8\pi^2 d_{eff}^2 P_p L^2}{n_s n_i n_p \varepsilon_0 \lambda_i \lambda_s c} sinh^2\left(\frac{\Delta k}{2} L\right) \qquad \text{Eq. 3-3}$$

,where λ_i, λ_s, n_s, n_i, $n_p$and c are idler wavelength, signal wavelength, signal refractive index, idler refractive index, pump refractive index and vacuum speed of light respectively. d_{eff} is the effective second-order non-linearity crystal. P_p and P_s are pump and signal power, respectively, and $L$is the crystal length.The phase factor $sinh^2\left(\frac{\Delta k}{2} L\right)$ accounts for phase mismatch ($\Delta k = k_{pump} - k_{signal} - k_{idler}$) and in the perfect phase matching case this term is unity.Note that the power gain increases quadratically with the crystal length due to the fact that electric field increases linearly along the crystal length under phase matching condition and this electric field gain will be squared to obtain the power gain.

With our experimental condition, the pump beam is 1W at 150kHz with 80μm beam size, therefore P_p is estimated to be 120 GW/cm^2. d_{eff} is the 0.51pm/V for the lithium niobate crystal in the type II DFG scheme(eo-o). Assuming perfect phase matched, one can find the theoretical gain is 240%. This plane wave approximation turns out to overestimate the gain and models including Gaussian beam calculation can be found in reference [45].

The maximum output power and conversion efficiency for different wavelengths of our DFG setup are shown in figure 3-3a.The output power shows that we achieve to generate strong mid-infrared light source from 2.4 to 4.7um. The DFG generation on the short wavelength side is limited by the filter we input to select signal wavelength. On the long wavelength side, it is limited by the transparent window of lithium niobate crystal. The largest conversion efficiency is 160% at 3.3μm. The conversion efficiency is slightly lower than the theoretical

gain 240% as expected due to the theoretical model does not include Gaussian beam propagation.

The output spectrum of the DFG setup is measured by a spectrometer and an infrared liquid-nitrogen-cooled InSb camera. The resulting spectra for three different wavelength input around 3μm are shown in figure 3-3b. The bandwidth at full width at half maximum is around 50cm^{-1}, corresponding to 86nm, for all three input. The bandwidth of the output DFG is agreed with the bandwidth of the pump beam. With such as bandwidth, one can potentially monitor several molecular vibration at the same time.

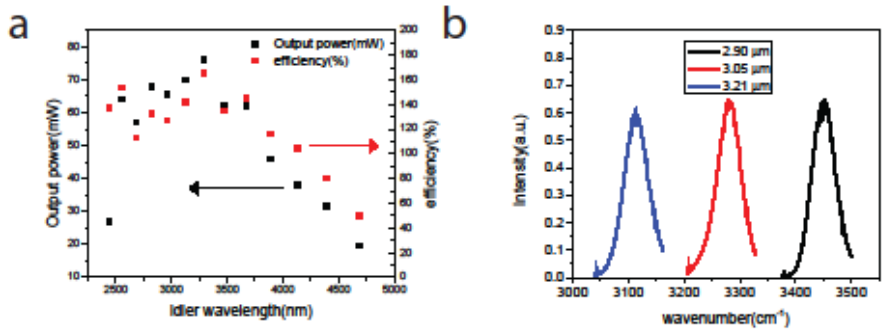

Figure 3-3 Experimental results from our DFG system. a, The maximum output power and conversion efficiency for different wavelengths of our DFG setup. **b,** The output spectrum of the DFG setup for three different signal beam wavelengths. The bandwidth at full width at half maximum is around 50cm^{-1}.

3.3 Synchronously Pumped Optical Parametric Oscillator

An optical parametric oscillator (OPO) is a parametric oscillator that converts an input laser wave (called "pump") with frequency ω_p into two output waves of lower frequency (ω_s, ω_i) by means of second-order nonlinear optical interaction[47]. With the advent of reliable high-powered mode-locked oscillators and high-quality non-linear crystals, optical parametric oscillators(OPOs) became viable sources of widely tunable ultrafast light during the last few years.

Here, we focus on the working principle of our home-built synchronously pumped OPO based on a Yb-doped fiber pulse laser at 1030nm as pumping system. The OPO system is able to generate stable and bright source from 3μm to 5μm.

3.3.1 Optical Parametric Oscillator and Quasi-Phase Matching Condition

An optical parametric amplifier(OPA) is an optical parametric system, inputting two light beams ω_p and ω_s, and designed as a single-pass - only one pulse present in the non-linear crystal at any one time, which we will talk about in section 3.4. If the non-linear crystal is placed into a resonator as shown in Figure 3-4a then the non-linear threshold is strongly reduced. Such a system is referred to as an OPO (optical parametric oscillator). In the optical parametric oscillator the initial idler and signal waves are taken from background waves, which are always present. One can also understand OPO as a light source similar to a laser, which also uses a cavity, but based on optical gain from parametric in a nonlinear crystal rather than from stimulated emission. Since the amplification of lights is based on a parametric process, unlike a laser, the output at arbitrary wavelength can be designed in principle as long as the final output is in the transmission range of the crystal.

An OPO can be either pumped continuous-wave laser or synchronously pumped with a mode-locked laser. For continuous-wave operation, an OPO is pumped with a high power laser since the lasing threshold for OPOs is high and it usually requires at least a few watts to surpass the threshold. Below the threshold, the OPO only gives some parametric and have negligible output power. An synchronously pumped OPO requires the resonator round-trip frequency matches the pulse repetition rate of the pump or a multiple of the pump repetition rate. This is usually done with a resonator with an adjustable mirror to fine tune the cavity length. Due to the strong peak intensity of typical mode-locked lasers, the required average pump power can be well reduced.

Wavelength conversion of laser beams in OPOs is an effective method to generate tunable radiation as well as radiation at wavelengths outside the range of available laser materials. In our study, we aim to generate strong and stable coherent light source for molecular spectroscopy in 3-5μm. The home-built OPO is designed to be synchronized with the pump source which is mode-lock fiber laser and with periodically poled lithium niobate(PPLN) as the gain medium. In the following paragraphs, we discuss the working principle of the PPLN.

As shown in chap 3-2, the traditional way to achieve phase matching is using optical birefringence of anisotropic crystal. However, the phase matching condition can only be met at critical angles and with various experimental instability the aligning becomes complicated. Therefore, one usually use a thin crystal to ease the phase matching condition which also limits the conversion efficiency eventually.

Another method called "Quasi-phase matching" provides a solution without crystal rotation and starts to become popular in the community[48], [49].In a difference frequency generation, energy flows from pump to signal when the phase between the two optical waves is less than π. Beyond π, energy flows back from the signal to the pump frequencies. The main concept of quasi-phase matching is to flip the crystal axes whenever the phase between the two optical waves reaches π, thereby convert destructive interference into constructive interference and the energy always flows from pump to signal. With such design, the

conversion efficiency is no longer limited by crystal length and therefore an efficient difference frequency generation can be achieved.

A commonly used material is lithium niobate which is a ferroelectric nonlinear crystal and therefore one can create poling patterns in a crystal through electrical poling with structured electrode. For quasi-phase matching, one make the periodically poled lithium niobate(PPLN) with periodicity $\Lambda = \frac{2\pi}{\Delta k}$. The additional wavevector provides an additional wavevector for the phase matching condition:

$$\Delta k = k_{pump} - k_{signal} - k_{idler} \qquad \text{Eq. 3-4}$$

Since the design does not depend on angle tuning, one can pole the crystal along the maximum nonlinear coefficient direction. The maximum nonlinear coefficient for lithium niobate is d33 = 27 pm/V and is used in PPLN where the three beams have the same polarization along the extraordinary direction.

In practice, lithium niobate crystals for wavelength conversion application are usually doped with MgO (<5%) because the dominant damage mechanism - photorefractive damage - can be mitigated through changing the material composition. The MgO-doped lithium niobate has significantly higher damage threshold(610 MW/cm^2) compared to the undoped crystal[50].

3.3.2 OPO Construction and Characterization

To achieve a stable light source for laser spectroscopy for molecular spectroscopy, we construct an optical parametric oscillator that could efficiently convert an input pump wavelength (1030 nm)into infrared wavelengths. Our home-built OPO is designed to be synchronized with the pump source - the round trip time of the pulse in the OPO cavity is the same as two times of repetition rate of the pump. 1-mm-thick 5% MgO-doped PPLN(MgO:PPLN) crystal is used as the pumping material to achieve quasi-phase matching. The idler wavelength is chosen to be around the C-H stretching bonds (3.3 μm) with the signal beam sitting at around 1500 nm. A Yb-doped fiber pulse(400fs) laser at 1030nm with 55.6MHz repetition rate is used as a pump laser. The pulse energy is 80nJ per pulse.

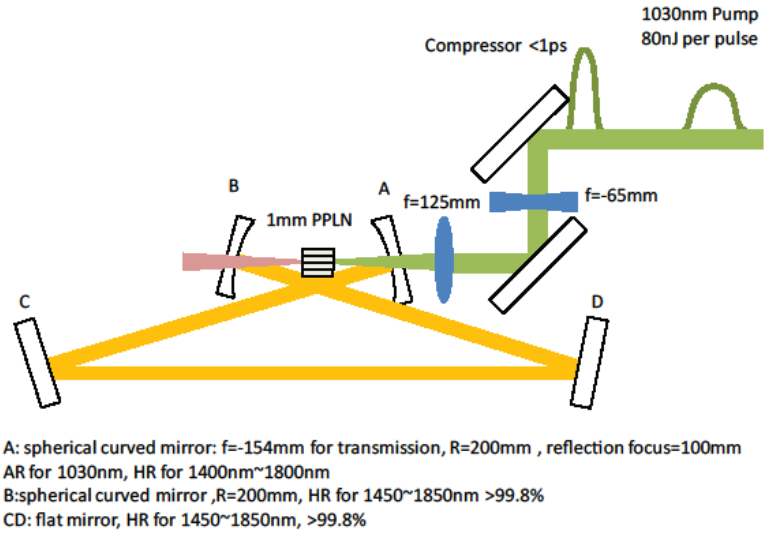

Figure 3-4 Experimental optical paths in our synchronously pumped OPO system. The pump beam(1030nm, green line) is first compressed to less than 1 picosenscond by a grating pair compressor. The compressed pump beam then is sent into the OPO cavity with the PPLN crystal. By controlling the position of C mirror, the zero time delay can be found and signal beam(1.3-1.7μm, yellow line) together with idler beam(2.4 - 4.7μm, red line) can be created.

Figure 3-4 shows the setup of the OPO. The pump laser is sent to a compressor to reduce the pulse width to less than 1ps and then a half-wave plate to change the polarization to vertical. A 15-cm focal length lens is used to focus the pump beam on to the PPLN crystal. A ring cavity is built with two planer mirror(C,D in Fig.3-4) and two curved mirror(A,B in Fig.3-4) and the optimal oscillator geometry is calculated with SNLO software(*10*). The radii of curvature of the curved mirrors are 20 cm. The curved mirrors are separated by 28cm to achieve the best mode overlap with the crystal. The incident angle of the flat mirrors is about 10 degree. The MgO-doped PPLN crystal is placed at the focal position between the two curved mirrors.

Along the transverse direction of the crystal, there are nine gratings with periods from 27.91 to 31.59 μm in the PPLN for different quasi phase matching conditions. The transmission of the specially-coated cavity mirrors for pump (1025 nm - 1030 nm) and idler (2300 nm - 4300nm) will be more than 90% to optimize input and output efficiency. The inner-side surfaces of the mirrors has highly reflective coatings (more than 99.9%) for signal wavelength (1400nm- 1900nm) so that the signal loss can be smaller for a lower lasing threshold. We also put the PPLN crystal in a temperature-controlled oven for further fine-tuning for the output wavelengths. In principle, the output at arbitrary wavelength can be designed, as long as the final output is in the transmission range of the crystal (down to 4.5-5μm).

To make the pulse OPO to work, one needs to design the total cavity length to be the distance for pulses to travel one trip in one or multiple repetition periods. With 55.6MHzrepetition

rate, the cavity length needed is 2.70m length which the pulse travel twice in the cavity before pumped. We carefully design the position for each mirror to make sure the total cavity distance adds up to 2.70m and then we mount the planar mirror C on the translational stage to fine tune the distance. A dispersive glass is inserted into the cavity for stretching the pulse and making the OPO more stable.

Lasing requires the signal gain to be larger or equal than the signal loss. The loss in the OPO comes from imperfect reflection at all four mirrors, crystal surfaces and dispersive glass. We estimated that our cavity has roughly ~4% loss without the dispersive glass inserted. Therefore threshold gain in the system should be around 4%. We can estimate the gain based on Eq. 3-3. With our experimental condition, the peak powerP_p is estimated to be 57 MW/cm^{2}for1W average power input with 100μm beam size. Input with other constants into Eq. 3-3, one can get an estimation of gain which is 7.3% per 1W average power therefore we expect to see lasing threshold around 550mW. Experimentally, we achieved a threshold of about 800mW with this experimental configuration.

To stabilize the OPO system against various experimental noises, such as air density fluctuation and pump laser repetition rate drift, we insert a dispersive glass into the OPO cavity to broaden the pulse width to achieve more stable light source. The idler output is shown in the figure 3-5 and the pumping threshold increases to 2.5W due to the reflection from the glass and lower peak power. With 5W pump, the pump depletion could reach about 36% with the idler output power at ~0.6W. To further stabilize the OPO system, we can add a PID feedback loop to the delay stage for controlling the cavity length. The feedback loop can counteract the pump laser repetition rate drift and we can achieve ~0.5% power fluctuation over 1 hour operation.

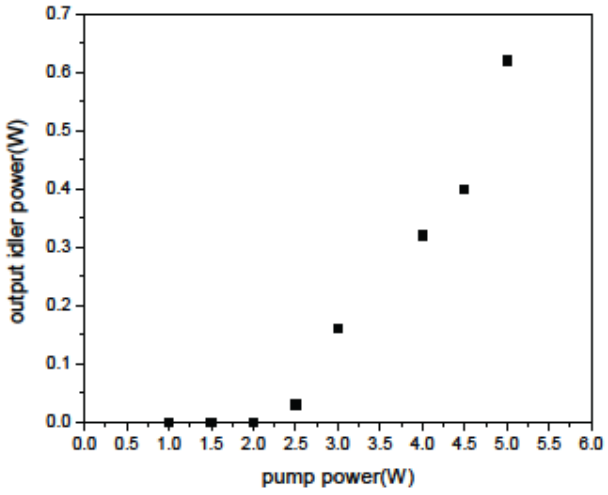

Figure 3-5 Experimental output power from our synchronously pumped OPO system with dispersive glass inserted. The idler output is measured by a pyroelectric powermeter after filtering out signal and pump. The pumping threshold is 2.5W due to the reflection from the glass and lower peak power. With 5W pump, the pump

depletion could reach about 36% with the idler output power at ~0.6W.

3.4 Summary

To sum up, we have demonstrated an tunable mid-infrared DFG generation with femtosecond Ti:sapphire pumping laser and lithium niobate crystal under phase matching condition. A strong, coherent, ultrafast mid-infrared light source is created from 2.4 to 4.7μm with >20mW average power and a conversion efficiency around 150%. To further explore the possibility in infrared laser, we also built an synchronized OPO system with PPLN crystal. The lasing threshold is reduced significantly compare to the DFG system. A strong and stable mid-infrared light source is also achieved in this case. These two light generation setups are the ideal tools for infrared spectroscopy of molecules and we will combine them with graphene-enhanced spectroscopy, which we will describe in the next chapter.

Chapter 4

Vibrational Spectroscopy at Electrolyte/Electrode Interfaces with Graphene Gratings

4.1 Introduction

The electrolyte/electrode interface is of great interest for both fundamental science and applied technology: a rich variety of electrical field dependent physical[51–53]and chemical processes[54,55] take place at this interface, which are important for applications such as batteries[56], fuel cells[57,58] and electroplating[59]. However, microscopic understanding of the processes at electrolyte/electrode interfaces is quite limited due to lack of suitable experimental probing techniques[60–62]. For example, powerful surface techniques such as scanning tunneling spectroscopy and many electron-based spectroscopy cannot access this interface. Optical spectroscopy can in principle probe buried interfaces and provide spectroscopic information of functional groups[63–65], but its application in probing the electrolyte/electrode interface has to overcome several challenges: (1) both the electrolyte and conventional metal electrodes are opaque to infrared light[66]; (2) the interfacial signal can be easily overwhelmed by the bulk electrolyte signal, and therefore in-situ detection with sub-monolayer sensitivity and surface specificity is difficult.

Graphene is an attractive electrode for studies of electrolyte/electrode interfaces. It is stable and transparent to infrared light, and is being actively explored for applications in supercapacitors[67],batteries, solar cells[68] and displays[69]. In addition, the carrier concentration (or Fermi level) of graphene, a key electrode parameter for understanding the electric double layer and interfacial processes, can be directly determined through optical absorption spectroscopy[70,71].

In this chapter, we show that graphene gratings provide an attractive platform for vibrational spectroscopy at the electrolyte/electrode interfaces: monolayer graphene is stable and transparent, and infrared diffraction from graphene gratings offers enhanced detection sensitivity and interface specificity. Using the adsorption of cetrimonium bromide (CTAB) on graphene as a model system, we demonstrate the vibrational spectroscopy of methylene group(CH_2) of adsorbed sub-monolayer CTAB molecules, and reveal a reversible field-induced electrochemical deposition of CTAB on the electrode controlled by the bias voltage.

Such vibrational spectroscopy with graphene gratings is promising for real time and in-situ monitoring of different chemical species at the electrolyte/electrode interfaces.

4.2 Diffraction Spectroscopy Design with Graphene Grating

The usual method to measure IR absorption spectroscopy is to use transmission or reflection configuration with FTIR and tungsten light as light source to achieve high signal-to-noise ratio. However, when the measured sample is in low concentration or the signal level is small, it takes a much longer time to acquire the data with reasonable signal-to-noise ratio. The speed of data acquisition is important when one wants to monitor dynamical processes such as chemical reactions or diffusions. Therefore, a new method to enhance sensitivity and increases data acquisition speed is desirable.

Here, we combine modern laser technique and diffraction spectroscopy to develop a high-speed, highly sensitive detection technique for molecular vibrational spectroscopy. The novel "diffraction spectroscopy" based on graphene grating electrodes is designed to achieve high detection sensitivity and interfacial specificity study.

The experimental scheme is illustrated in Fig.4-1a. A femtosecond optical parametric amplifier is used as the light source, which produces tunable broadband infrared radiation with a bandwidth of ~80 cm^{-1} and a repetition rate of 150 KHz. Then the infrared beam is collimated to around 5mm beam size and then separated by a beam splitter and divided into two path ways. One is sent onto a graphene grating electrode, which forms an electrochemical cell together with a platinum counter electrode and the aqueous electrolyte (Fig.4-1b), for molecular vibrational spectroscopy. The other is shining on a grating with the same groves design(8um period thin gold on a fused silica substrate) as a reference to minimize the laser intensity and spectral drift. Both the dispersed beam from graphene grating and reference grating are then collected by a liquid nitrogen cooled InSb camera with 128×128 pixel arrays.

To probe molecular species at the electrolyte/graphene electrode interface, we measure the first-order diffraction from the graphene grating rather than the transmission or reflection signal. Fig. 4-1b shows the optical microscopy image of a typical graphene grating with 8 μm period on a fused silica substrate[72].The diffraction signal originates from the periodic variation of optical susceptibility at the interface, which comes from not only the graphene grating itself, but also the different adsorbed molecules and chemical species in the electrolyte double layer (EDL) induced by the graphene electrode relative to that of the fused silica substrate(Fig.4-1c). The bulk electrolyte solution beyond the nanometer thick double layer region is homogeneous and contributes no diffraction signal. Therefore this diffraction scheme provides excellent interface specificity.

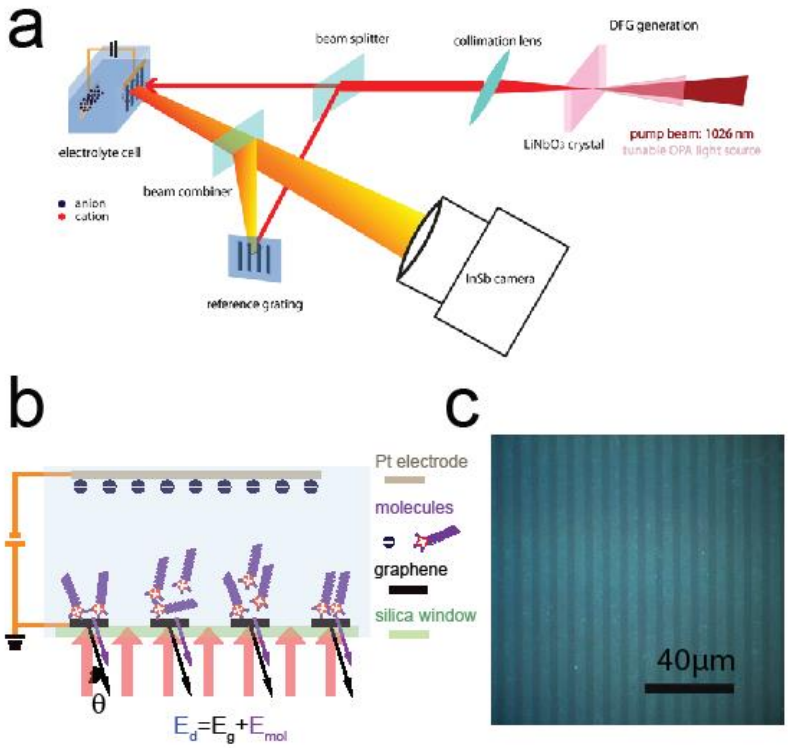

Figure 4-1 Schematic illustration of the spectroscopy design with graphene grating. **a**,The electrochemical cell and spectroscopy configuration. Fused silica substratesare used as cell windows.The diffraction singals originate froman effective grating formed by periodic graphene/electrolyte and fused silica/electrolyte interfaces. The incident light electric field E_{in} is p-polarized, and the 1st order diffraction is collected at the diffraction angleθ=25.9º. **b**, The diffraction signal is generated by a periodic variation of the optical susceptibility at the interface, which comes from both the graphene grating itself and the different adsorbed molecules like CTAB and chemical species in the electrolyte double layer (EDL) induced by the graphene grating. **c**, Optical microscopic image of a graphene grating on fused silica. The bright ribbonsare graphene and the grating period is 8 μm.

From the scattering theory, the grating diffraction process can be treated as an incident light wave excites the graphene and the radiation from graphene grating eventually constructively interferes at the diffraction angle. The first order diffraction intensity from the graphene grating is described by

$$I_g = |E_g|^2 = \eta \cdot |\sigma_g E_{in}|^2 = \eta \cdot |E_{in}|^2 \cdot [\left(Re(\sigma_g)\right)^2 + \left(Im(\sigma_g)\right)^2] \qquad \text{Eq. 4-1}$$

where E_g is the radiated electric field from graphene grating at the diffraction angle, η is a prefactor related to incident angle, polarization and grating geometry and σ_g is the complex conductivity of graphene.

Figure 4-2 displays the simulated $|\sigma_g|^2$ spectra at various Fermi energy E_F. Near the CNP, $Re(\sigma_g)$ from interband transitions dominates the diffraction signal and therefore produce a flat diffraction spectrum. As the doping increases, $Re(\sigma_g)$ decreases significantly due to Pauli blocking, and accounts for the reduced diffraction intensity for photon energy $\hbar\omega < 2|E_F|$. At the same time, $Im(\sigma_g)$ from intraband transitions starts to dominate the low frequency part of spectrum, which ultimately leads to diffraction intensity increasing at low frequency.

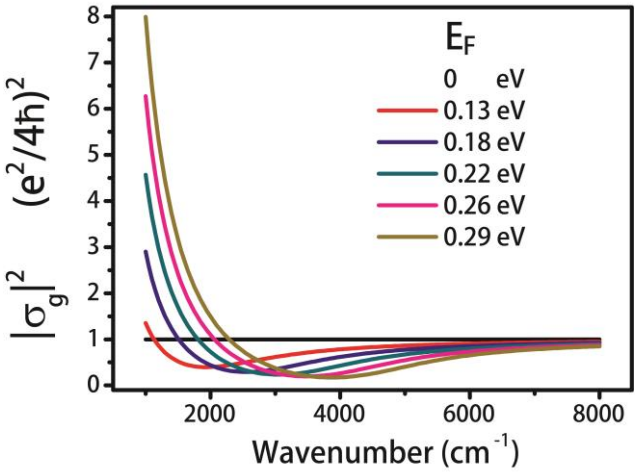

Figure4-2.Simulated $|\sigma_g|^2$ from pristine graphene gratings at different Fermi energy E_F. Intensity of diffraction spectra is proportional to $|\sigma_g|^2$.

4.3. Molecular Vibrational Modes in Diffraction Spectroscopy

The frequency of a molecular vibration mode is typical in the range from 10^{12} to 10^{14} Hz(from microwave to infrared range)[73]. The vibrational states of a molecule can be probed through either infrared spectroscopy or Raman spectroscopy. The most direct way is through infrared spectroscopy, as vibrational transitions typically require an amount of energy that corresponds to the infrared region of the spectrum.

The infrared spectroscopy can be used to identify the functional groups present in a molecule via excitation of molecular vibration modes. More detailed study can even tell the conformation, stacking order, environment of the molecules. The infrared spectroscopy is proven to be a powerful tool to understand the molecular behaviors, including absorption processes on surfaces, chemical reactions dynamics, and nano-material characterizations.

Here, we use graphene grating to develop a new molecular vibrational spectroscopy method to study molecular dynamics.

4.3.1 Vibrational Spectroscopy in Diffraction Scheme

With molecules attached to graphene grating, the diffraction intensity is described by interference between the radiation from graphene and molecules. Therefore, the total diffraction intensity

$$I_{\mathrm{d}} = \left|E_{\mathrm{g}} + E_{\mathrm{mol}}\right|^2 = \eta \cdot |E_{\mathrm{in}}|^2 \cdot [\left(Re(\sigma_{\mathrm{g}}) + Re(\sigma_{\mathrm{mol}})\right)^2 + \left(Im(\sigma_{\mathrm{g}}) + Im(\sigma_{\mathrm{mol}})\right)^2 \quad \text{Eq. 4-2}$$

,where σ_{mol} is the complex conductivity of molecules.

The diffraction spectroscopy greatly enhances the detection sensitivity of the electrode-induced changes of molecular concentration at the interface. In conventional infrared absorption spectroscopy, the transmitted light intensity I_{t}results from interference between the incident light and the forward scattering of molecular species, i.e. $I_{\mathrm{t}} = |E_{\mathrm{in}} + E_{\mathrm{mol}}|^2 \approx |E_{\mathrm{in}}|^2 + 2 \cdot Re(E_{\mathrm{in}}{}^{*} \cdot E_{\mathrm{mol}})$, where E_{in} and E_{mol} is theelectrical field of incident light andmolecular radiation respectively, and $|E_{\mathrm{mol}}|^2$ is omitted because $|E_{\mathrm{mol}}| \ll |E_{\mathrm{in}}|$ .The relative intensity change due to light absorption is therefore determined by $\Delta I_{\mathrm{t}}/I_{\mathrm{t}} \approx 2 \cdot Re(E_{\mathrm{in}}{}^{*} \cdot E_{\mathrm{mol}})/|E_{\mathrm{in}}|^2$. For a monolayer of material, $|E_{\mathrm{mol}}|$ from molecular vibration is typically less than 10^{-3} of E_{in}[74]. So the absorption signal is usually ~10^{-3} of the background light, and requires special infrared spectrometer and long-time average to obtain a reasonable absorption spectrum. In contrast, the diffracted signal is due to the interference between the diffraction of graphene electrode (E_{g}) and the periodic modulation of molecular species within the electrical double layer (E_{mol}) (Fig. 4-1b). Therefore the relative intensity change in the diffraction signal is

$$\Delta I_{\mathrm{d}}/I_{\mathrm{d}} \approx 2 \cdot Re\left(E_{\mathrm{g}}{}^{*} \cdot E_{\mathrm{mol}}\right)/\left|E_{\mathrm{g}}\right|^2. \quad \text{Eq. 4-3}$$

Because the diffracted electrical field from the graphene grating (E_{g}) is about 1% of the incident electrical field E_{in}[75,76], the relative contrast of the molecular vibration signal in diffraction spectra will be enhanced by almost two orders of magnitude compared with direct absorption spectroscopy.

In principle, this technique can be extended to ultrathin film metal gratings. However, it is practically difficult to form sub-nanometer or 1 nm thin continuous metal films. For thicker films, the diffraction from metal will lead to a strong background and diminish the advantage of the diffraction spectroscopy.

4.3.2 Methylene Stretching Modes of PMMA Residues On Graphene

We first apply this vibrational spectroscopy based on graphene gratings by investigating PMMA residue polymer on graphene originated from the transfer and photolithography processes. CH_2stretchingmodes is abundant in PMMA and of interest for graphene device research[77].

The diffracted spectra within the spectral range of 2800cm^{-1}-3000cm^{-1} from the transferred graphene grating at the electrolyte/electrode interfaces in an electrochemical cell are taken with a two-dimensional InSb IR camera. First, we examine the diffraction signal E_g from the graphene grating electrode using 12mM NaCl solution as the electrolyte. Figure 4-3a shows the diffraction intensity at 3000 cm^{-1} as a function of the bias voltage from 1.1 V to -0.4V (black squares), which is normalized by the intensity value at the charge neutral point (CNP) of graphene. The diffraction intensity at 3000 cm^{-1} contains contribution mainly from the graphene grating because this frequency is away from any molecular vibration resonances in this system. The bias voltage of the electrochemical cell acts as an electrical gate that controls carrier concentration in graphene. At V_{bias} = 0Vgraphene is strongly p-doped in the NaCl solution, and it becomes charge neutral at V_{bias} = 1.0V. We observe that the diffraction intensity shows a local maximum at the CNP, which decreases upon hole doping to ~ 10% of the CNP signal at V_{bias} = 0.5V. Afterwards, the diffraction signal starts to increase with further hole doping. This non-monotonically change in IR diffraction from the graphene grating originates from the gate-dependent complex optical conductivity in graphene[78], since the first order diffraction intensity from the graphene grating I_g is proportional to $Re(\sigma_g)^2 + Im(\sigma_g)^2$, where $Re(\sigma_g)$ and $Im(\sigma_g)$ is the real part and imaginary part of graphene conductivity σ_g.

Figure4-3b displays the calculated $Re(\sigma_g)$, $Im(\sigma_g)$ and $|\sigma_g|^2$ at 3000cm^{-1} as a function of the Fermi energy E_F. Near the CNP, $Re(\sigma_g)$ from interband transitions dominates the diffraction signal. $Re(\sigma_g)$ decreases significantly when $2|E_F|$ equals the incident photon energy due to Pauli blocking, and accounts for the reduced diffraction intensity from carrier doping initially. However, at high doping levels $Im(\sigma_g)$ from intraband transitions starts to dominate, which ultimately leads to diffraction intensity increasing at high $|E_F|$. The solid line in Figure4-3a shows the good agreement of this model with the experimental data.

Next, we show the IR diffraction spectra (from 2800cm^{-1} to 3000cm^{-1}) from as-prepared graphene electrodes in the 12mM NaCl solution at different bias voltages. Figure 4-3c shows the normalized diffraction spectra $I_d(\omega)/I_d^{CNP}(\omega)$, where $I_d^{CNP}(\omega)$ the spectrum at CNP, is used as the reference. We observed two sharp resonances at 2916cm^{-1}and 2848cm^{-1}on top of a broad background signal. The broad background arises from the graphene electrode, which first decreases and then increases with higher electron doping controlled by V_{bias}. The two resonances at 2916cm^{-1} and 2848cm^{-1} correspond to the anti-symmetric and symmetric

stretching vibrations of the methylene group (-CH_2-), respectively. A weak resonance at 2960 cm^{-1} corresponding to methyl group (-CH_3) is also present. The appearance of CH_2 vibration peaks indicates that there are hydrocarbons on top of as-prepared graphene in NaCl solution, presumably due to the residue from the polymer transfer and/or photolithography processes.

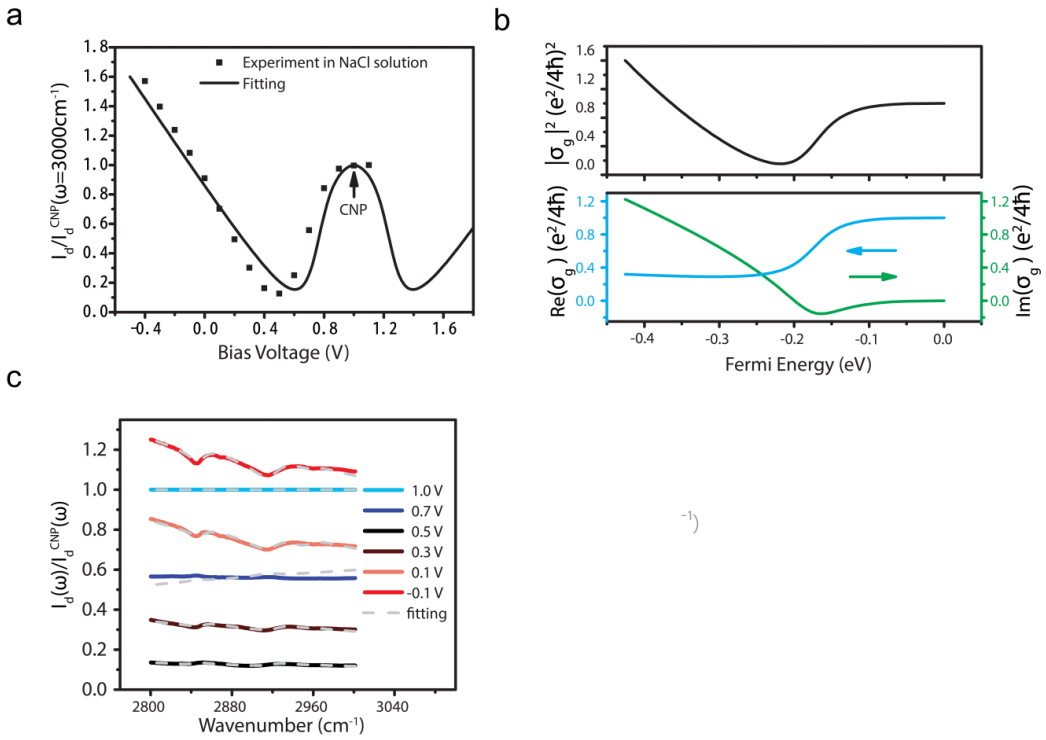

Fig.4-3 Bias-dependent diffraction spectra with graphene gratingsin different electrolytes. a, Normalized diffraction intensity I_d/I_d^{CNP}as a function of V_{bias}at 3000cm^{-1}, which probes only the graphene grating response. The black dots and black line are experimental data and fitting, respectively,for graphene gratings in a 12 mM NaCl solution. The diffraction intensity shows a local maximum at CNP (V_{bias}=1.0 V). **b**, Simulation of the graphene conductivity in the NaCl solution as a function of Fermi level. Red:$Re(\sigma_g)$; green: $Im(\sigma_g)$; black: $|\sigma_g|^2 \propto I_d$. **c**, The solid lines show normalized diffraction spectra $I_d(\omega)/I_d^{CNP}$ (ω) at different V_{bias}. Two CH_2 vibrational resonances at 2916 $cm^{-1}$and 2848 cm^{-1} are observed from polymer residues for the as-prepared graphene grating in a NaCl electrolyte.The dashed lines are theoretical fitting of the diffraction spectraas described in the text.

The diffraction spectra in Figure 4-3c result from the interference between the graphene and CH_2 vibration signals, and their understanding requires quantitative description of diffracted

electrical field from both graphene and CH_2 vibrations at different bias voltages. The normalized diffraction intensity is described by

$$\frac{I_d}{I_d^{CNP}} = \frac{[Re(\sigma_g+\sigma_{mol})]^2+[Im(\sigma_g+\sigma_{mol})]^2}{[Re(\sigma_g^{CNP}+\sigma_{mol}^{CNP})]^2+[Im(\sigma_g^{CNP}+\sigma_{mol}^{CNP})]^2} \quad \text{Eq. 4-4}$$

,where σ_g and σ_{mol} are the effective complex conductivity for graphene and the adsorbed molecules, respectively. σ_g^{CNP}, σ_{mol}^{CNP} are corresponding value near CNP. This equation can be directly derived from Eq. 4-2.

We find that the experimental data can be well fitted by a constant amount of CH_2 functional groups radiation interfering with the gate-dependent graphene radiation at different carrier concentration. All experimental diffraction signals including optical responses of both graphene grating (Fig.4-3a) and periodic modulated molecular vibrations (Fig.4-3c) are fitted using Eq. 4-4 with same material parameters. The fitting results are shown in solid black lines in Fig. 4-3a and in dashed silver lines in Fig. 4-3c, and the model used is described below.

The graphene complex conductivity$\sigma_g$used in the fitting is described by Eq. 2-26**.** The free carrier scattering rate $1/\tau$ has little effect on the dielectric constant in our spectral range and can be approximated as zero. The Fermi level E_F varies with the carrier concentration n as $E_F = hv_F\sqrt{\pi n}$, where the Fermi velocityv_F is set to 10^6 m/s. In the electrolytic cell, the averaged carrier concentration n_0 can be described by a capacitor model $n_0 = C(V_{bias} - V_{CNP})/e$, where C is fitted to be 1.17 and 0.77 $\mu F/cm^2$ for NaCl and CTAB gating, respectively.To account for the doping inhomogeneity in graphene, we introduced a local carrier concentration broadening of $\Delta = 2\times10^{11}/\text{cm}^2$. As a result, the conductivity of graphene can be described as

$$\sigma_g(n_0) = \frac{\int \sigma_g(n) e^{-(n-n_0)^2/\Delta^2} dn}{\int e^{-(n-n_0)^2/\Delta^2} dn} \quad \text{Eq. 4-5}$$

The interband transition broadening Γ is assumed to be proportional to the carrier concentration and it is qualitatively described as $\Gamma = A|V_{bias} - V_{CNP}|$ in our simulation. The fitting results for the diffraction intensity as a function of V_{bias} are plotted in Fig. 4-3a (solid lines), where the fitting parameter are listed in Table 4-1. Using the model described above, we can calculate the diffraction spectra from 1000 cm^{-1} to 8000 $cm^{-1}$for pristine graphene gratings at different E_F.

Fitting parameters	C (/cm^2· V)	A (eV/V)	Δ (/cm^2)
NaCl gating	7.3×10^{12}	0.26	2×10^{11}
CTAB gating	4.8×10^{12}	0.21	3.3×10^{11}

Table 4-1 Fitting parameters of graphene grating diffraction intensity at 3000 cm^{-1} for NaCl gating and CTAB gating

The molecular responsesσ_{mol} from $CH_2$and CH_3 vibrations can be described by a Lorenz model. Three vibrational resonances are present: the anti-symmetric CH_2, symmetric CH_2, and CH_3 resonances. The molecular optical susceptibility χ_{mol} andoptical conductivityσ_{mol}aretherefore characterized by

$$\chi_{\mathrm{mol}} = \frac{e^2}{\varepsilon_0 m_{\mathrm{CH2}} d_{\mathrm{mol}} (2\pi c)^2}\left[\left(\frac{NA_1}{\nu_1^2-\nu^2-i\nu\cdot\Gamma_1}\right)+\left(\frac{NA_2}{\nu_2^2-\nu^2-i\nu\cdot\Gamma_2}\right)\right]+\frac{e^2}{\varepsilon_0 m_{\mathrm{CH3}} d_{\mathrm{mol}} (2\pi c)^2}\left(\frac{N'A_3}{\nu_3^2-\nu^2-i\nu\cdot\Gamma_3}\right) \quad \text{Eq. 4-6}$$

$$\sigma_{\mathrm{mol}} = i\omega d_{\mathrm{mol}}\varepsilon_0\chi_{\mathrm{mol}} \quad \text{Eq. 4-7}$$

Here$N$, N',m_{CH2}, m_{CH3}, d_{mol}, is, respectively, the CH_2, the CH_3functional group density, CH_2 and CH_3 functional group mass, thin molecule film thickness. A_i(i = 1, 2, 3) , ν_i (i = 1, 2, 3) , and Γ_i (i = 1, 2, 3) are oscillator strength, resonance wave number, and the broadening of each mode, which is symmetric CH_2, anti-symmetric CH_2 and CH_3 resonance in sequence. The oscillator strengths A_1=0.63, A_2=1.372, A_3=0.21is taken from literature by assuming effective mass of CH_2 group as 14 proton mass. The fitting of Fig. 4-3c yields resonance peak positions and widths at around ν_1 =2848 cm^{-1}, ν_2 =2920 cm^{-1}, ν_3 =2960 cm^{-1}, Γ_1 =25 cm^{-1}, Γ_2 =30 cm^{-1}, Γ_3 =20 cm^{-1} (Fig.4-4 a, b), comparable to the established values.

We estimate the density of CH_2 groups is ~$1.1\times10^{15}cm^{-2}$on as prepared graphene gratings from the magnitude of the CH_2 anti-symmetric and symmetric stretching modes[79].The change of lineshape of the vibration resonance at different voltages is due to the interference between the molecular and graphene responses. We note that the CH_2 concentration corresponds to on average one CH_2 group per unit cell in graphene, i.e. an "effective" monolayer coverage, although the actual distribution of hydrocarbon is likely to be randomly distributed with relatively large clusters. And this effective monolayer coverage leads to a change of diffraction intensity of ~ 6% from the graphene grating (Fig. 4-2c). This is in contrast to only~ 10^{-3} change for monolayer CH_2 absorption in conventional transmission measurements. Indeed, we observe the CH_2 peaks from organic residue at 10^{-3} level in similarly prepared graphene samples using conventional FTIR spectroscopy with hours of average. Using the diffraction spectroscopy with graphene gratings, the relative signal change is enhanced by ~ 50 times, and it enables us to obtain monolayer CH_2 absorption spectra within seconds.

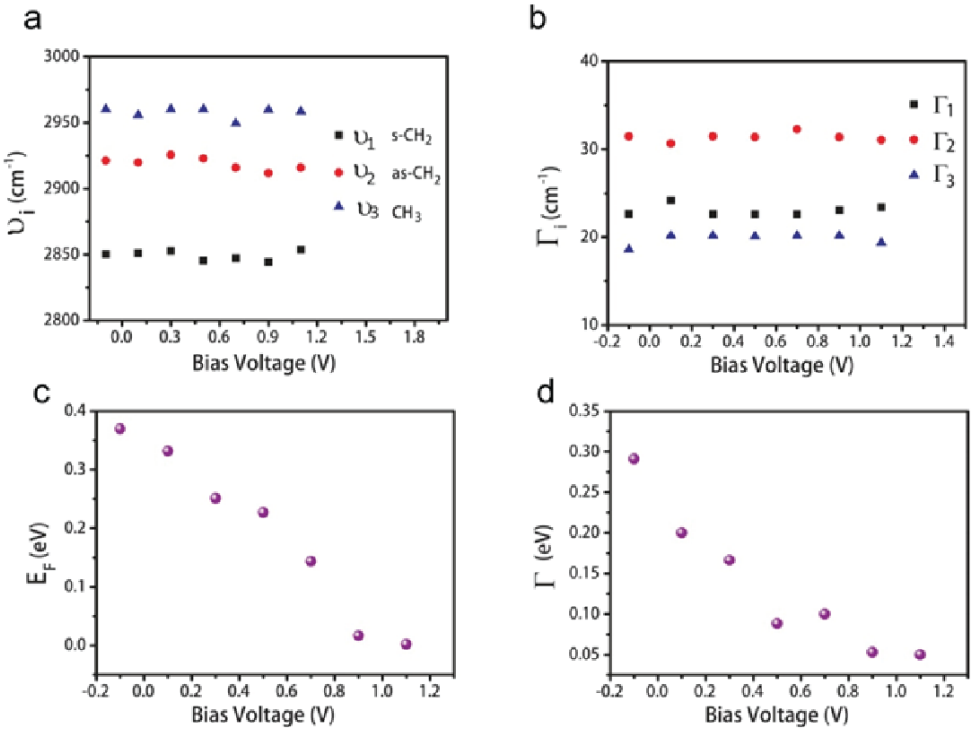

Figure 4-4 Fitted parameters of interference between graphene grating diffraction and molecule resonance diffraction as bias voltage is increasing in 12 mM NaCl electrolyte. a, Molecular vibration resonance peak position. **b,** Molecular vibration full width half maximum. **c,** Graphene Fermi level. **d,** Graphene interband broadening. Charge neutral point voltage V_{CNP} = 1.0 V.

4.4 Observation of Adsorbed CTAB in Diffraction Spectra

The vibrational spectroscopy based on graphene grating, with its high sensitivity and interface specificity, enables us to in-situ monitor the accumulating process of molecular species at the electrolyte/graphene electrode interface. Here we use a cationic surfactant CTAB($CH_3(CH_2)_{15}N(CH_3)_3Br$) as a test system. CTAB have been widely used to assist DNA extraction[80], gold nanoparticle synthesis[81] and carbon nanotube dispersion[82].

We plot in Fig. 4-5a (red squares) the gate-dependent diffraction signal at 3000 $cm^{-1}$from the graphene grating in 11mM CTAB solution. Compared with graphene in NaCl solution, the voltage dependence shows a similar behavior except that the CNP is strongly shifted to V_{bias} = 0.2V. Apparently CTAB largely cancels the strong p-doping in as-prepared graphene, presumably due to the adsorption of cation$CH_3(CH_2)_{15}N(CH_3)_3^+$ (abbreviated as CTA^+) that induces a significant amount of electrons in graphene.

The diffraction spectra near CH_2 vibration frequencies from the CTAB solution/graphene electrode interface at different bias voltages are shown in Fig.4-5b. The CNP spectrum at V_{bias} = 0.2V is used as the reference. The spectra are reproducible in many cycles when the bias voltage is varied between -1 V to 1.5V, and there is a finite hysteresis when scanning direction switches. The bias dependent spectra are quite similar to that in NaCl solution (Fig. 4-3c) except that the area of CH_2peakis2 times larger. It indicates a higher CTAB concentration near the graphene electrode than that near bare fused silica substrate. A quantitative fitting of the spectra (dashed lines in Fig. 4-3c)can be achieved by assuming a constant excess CTAB molecule surface density of $1.9\times10^{14}cm^{-2}$, corresponding to effectively 0.16 CTAB molecule per unit cell of graphene. The adsorbed CTAB molecules are likely to be disordered and isotropic since the spectral weight ratio for symmetric CH_2 and anti-symmetric CH_2 modes resembles that of isotropic ensemble of CTAB molecules.

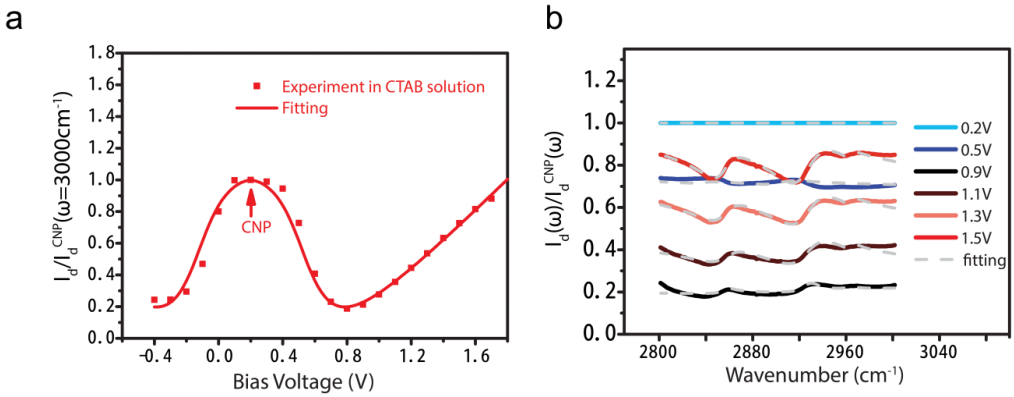

Figure 4-5 Bias-dependent diffraction spectra with graphene gratings in 11mM CTAB solution. a, Normalized diffraction intensity I_d/I_d^{CNP}as a function of V_{bias}at 3000cm^{-1}, which probes only the graphene grating response. The red dots and red line are experimental data and fitting, respectively,for graphene gratings in a 11 mMCTAB solution. The diffraction intensity shows a local maximum at CNP (V_{bias}=0.2 V). **b**, The solid lines show normalized diffraction spectra $I_d(\omega)/I_d^{CNP}(\omega)$ at different V_{bias}. More pronounced CH_2 vibrational resonances at 2916 $cm^{-1}$and 2848 cm^{-1} are observed for graphene gratings in the 11mM CTABdue to CTAB adsorption at the interface.

4.5 In-Situ Vibrational Spectroscopy for Electrochemical Reaction

We investigate CTAB electrochemical reaction with graphene electrode with diffraction spectra as an example. The diffraction spectra around CH_2streching modes are taken to show the concentration change at the electrolyte/electrode interface due to electrochemical deposition and dissolution of the CTAB molecules.

4.5.1 Deposition Process Monitored by Diffraction Spectroscopy

For the electrochemical reaction to happen, we scanned the bias voltage from 1.5V to -1.5V, and then back to 1.5V in 1.4mM CTAB solution. Figure 3a shows the bias-dependent diffraction intensity at 3000 cm^{-1}, and Fig. 3b is the corresponding cyclic voltammetry curve. Figure 3c-f display the diffraction spectra when the V_{bias} is scanned from 1.5V to -1.5V (Fig. 4-6c, d), then from -1.5V to 0.2 V (Fig. 4-6e). Here we focus on the anti-symmetric CH_2 vibrations in the spectral range of 2870-2980 cm^{-1} and all the spectra are normalized by the initial CNP spectrum at V_{bias} = 0.3V.

When V_{bias} is varied between 1.5V to -1.2 V (Fig. 4-6c, d), the evolution of the spectra is similar to that in Fig.4-5b, and it can be accounted for by the interference of graphene grating and a constant amount of CH_2 groups at the interface. Spectra with electron or hole doping are largely symmetric because the graphene intrinsic response is symmetric. When V_{bias} reaches -1.5V and starts to scan back, we see very different behavior in the diffraction spectra as shown in Fig.4-6e. First, we observe a strong increase in the overall diffraction intensity, indicating significant electrochemical deposition of materials at the graphene electrode. At the same time, we observe new spectral features emerging around 2920 cm^{-1} (red arrow) and 2944 cm^{-1} (green arrows.).

To understand the physical meaning of these spectra features evolution, we develop a model to depict the diffracted electrical field from both graphene and deposited CTAB molecules at different bias voltages similar to the adsorption case. We modified the Eq. 4-4 and replaced optical conductivity of adsorbed molecule term σ_{mol} at high Fermi level with the optical conductivity of deposited CTAB term σ_{dep} and we get

$$\frac{I_{\mathrm{d}}}{I_{\mathrm{d}}{}^{CNP}} = \frac{\left[Re(\sigma_{\mathrm{g}}+\sigma_{\mathrm{dep}})\right]^2+\left[Im(\sigma_{\mathrm{g}}+\sigma_{\mathrm{dep}})\right]^2}{\left[Re(\sigma_{\mathrm{g}}{}^{CNP}+\sigma_{\mathrm{mol}}{}^{CNP})\right]^2+\left[Im(\sigma_{\mathrm{g}}{}^{CNP}+\sigma_{\mathrm{mol}}{}^{CNP})\right]^2} \quad \text{Eq. 4-8}$$

$$\chi_{\mathrm{dep}}^{\mathrm{res}} = \frac{e^2 N_{\mathrm{dep}}}{\varepsilon_0 m_{\mathrm{CH2}} d_{\mathrm{dep}} (2\pi c)^2}\left[\left(\frac{A_4}{\nu_4^2-\nu^2-i\nu\cdot\Gamma_4}\right)+\left(\frac{A_5}{\nu_5^2-\nu^2-i\nu\cdot\Gamma_5}\right)+\left(\frac{A_6}{\nu_6^2-\nu^2-i\nu\cdot\Gamma_6}\right)\right] \quad \text{Eq. 4-9}$$

$$\chi_{\mathrm{dep}}^{\mathrm{non-res}} = \alpha \quad \text{Eq. 4-10}$$

$$\sigma_{\mathrm{dep}} = \sigma_{dep}^{res} + \sigma_{dep}^{non-res} = \mathrm{i}\omega d_{\mathrm{dep}} \varepsilon_0 \left(\chi_{\mathrm{dep}}^{\mathrm{res}} + \chi_{\mathrm{dep}}^{\mathrm{non-res}}\right) \quad \text{Eq. 4-11}$$

,where the σ_{dep} can be separated into two parts: $\sigma_{dep}^{non-res}$ the non-resonant contribution and σ_{dep}^{res} the resonant contribution of CTAB molecules. σ_{dep}^{res} is further described with the Lorentz model and is representing the resonances contribution in the spectrum range as described by Eq. 4-9, Eq. 4-11,where$\chi_{\mathrm{dep}}$is the optical susceptibility of deposited CTAB molecules. In Eq. 4-9, the most pronounced three resonance with ν_4 = 2850 cm^{-1}, ν_5 = 2918 cm^{-1}, ν_6 = 2944 cm^{-1}, Γ_4 =22 cm^{-1},Γ_5 =30 cm^{-1}, Γ_6 =16 $cm^{-1}$are used in the fitting. The resonance at 2850 cm^{-1} and 2918 cm^{-1} are CH_2 symmetric and anti-symmetric stretching modes. The 2943 cm^{-1} has been assigned to symmetric stretching mode for the head group of CH_3-(N^+). $\sigma_{dep}^{non-res}$ in Eq. 4-10, is the non-resonance part of the optical conductivity of the deposited CTAB layer. It is related to the non-resonant susceptibility of CTAB layer $\chi_{\mathrm{dep}}^{\mathrm{non-res}}$ as shown in Eq. 4-11. $\chi_{\mathrm{dep}}^{\mathrm{non-res}}$ is simply described by a real constant α =1.06 in our spectral range. The fitting results are shown as gray dashed lines in Fig. 4-6f with

experimental spectra taken during the CTAB depositing on the graphene grating. The model is able to qualitatively reproduce the experimentally observed spectral features.

Previous studies of CTAB have shown that a new vibrational resonance around 2943 cm^{-1} is associated with the head group of CH_3-(N^+) in crystalline CTAB[83], and its presence indicates the formation of highly ordered CTAB at the graphene electrode. Therefore our observed potential dependent diffraction spectra indicate that once the V_{bias} reaches -1.5V, a new electrochemical process is triggered to deposit highly ordered CTAB on the graphene electrode. This deposition process can be monitored in real time with our diffraction spectroscopy.

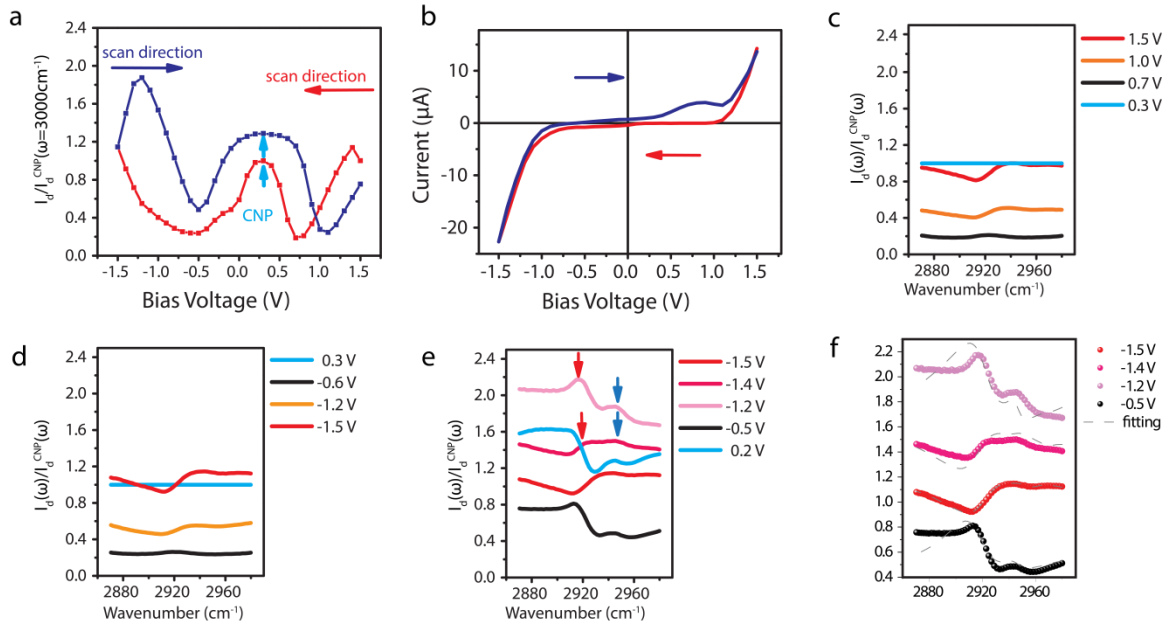

Figure 4-6 Electrochemical deposition process monitored by diffraction spectroscopy. a, Diffraction intensity I_d from the interface at 3000 cm^{-1} as a function of the bias voltage V_{bias}. V_{bias} was scanned from1.5V to -1.5 V (red), and then back to 1.5 V (blue). **b**, The cyclic voltammetry current shows a significant increase of current flowing through the interface at V_{bias} = -1.5V during the negative scan, and an extra peak at V_{bias} = 1 V during the positive scan. **c,d,e** are diffraction spectra from 2870-2980cm^{-1} near the anti-symmetric CH_2 vibration during the voltage scanning. All the spectra are normalized by the initial CNP spectrum at V_{bias} = 0.3 V. **c**,**d**, Vibrational spectra with V_{bias} scanning from 1.5V to -1.5V show behavior similar to that in Fig. 4-5b. It can be described by a constant amount of CH_2 group but a varying graphene dielectric constant. **e**, Vibration spectra with V_{bias} scaning from -1.5V to 0.2V. Total light diffraction intensity increases after V_{bias} has reached -1.5V, the threshold for significant current increase in the cyclic voltammetry. At the same time, two new features near 2920cm^{-1}(red arrow) and 2944cm^{-1} (green arrow) emerges. These

spectra features indicate significant electrochemical deposition of crystalline CTAB after V_{bias} has passed -1.5V. The electrochemically deposited CTAB molecules persists and leads to a resonance dip at the new CNP with V_{bias}= 0.2 V. **f**, Fitted spectra are included as the gray dashed lines in addition to the experiment results using the CTAB deposition model.

4.5.2 Dissolution Process Monitored by Diffraction Spectroscopy

When the bias voltage is further increased to positive, the deposited CTAB systematically modify the diffraction spectra. At the CNP with V_{bias} = 0.2V, the normalized spectrum shows distinct features rather than a constant. When V_{bias} is further scanned beyond 1 V, however, the features associated with the deposited CTAB layer become weaker and then disappears, and the spectral shape becomes similar to those in Fig.4-5c and d. It indicates that the deposited CTAB layers are being dissolved at these bias voltages. The observed deposition and dissolution of CTAB layers is also monitored with the cyclic voltammetry curve in Fig. 4-6b, where we observe a significant increase of current at V_{bias} = -1.5V in the negative scan, coincidence with the start of CTAB deposition, and a peak around V_{bias} = 1V in the positive scan, coincidence with the disappearing of CTAB deposition. After the V_{bias} reaches 1.5V, most of the deposited CTAB is dissolved, and the graphene electrode recovers to its initial status. The deposition/dissolution process is reversible as shown in the Fig. 4-7, as the spectra for V_{bias} larger than 1V become similar to the spectra in Fig. 4-5b where we have only adsorbed CTAB on graphene.

The origin of the observed electrochemical deposition and dissolution of CTAB layers is not clear yet. When the graphene electrode is acting as an anode at V_{bias} = -1.5V, it can potentially oxide Br^- into Br_2 at the electrode. In this case, one may expect the corresponding CTA^+ cation reduction and deposition in the platinum counter electrode. However, we observe the deposition of CTAB layers at the graphene electrode. Further theoretical investigation will be required to understand microscopically the unconventional deposition processes taking place at the interfaces.[83,84]

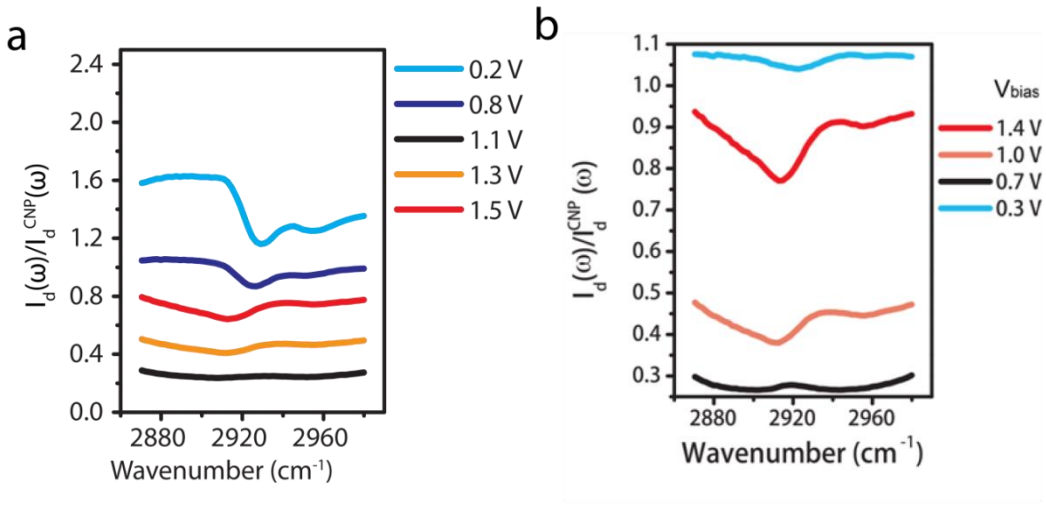

Figure 4-7 Electrochemical dissolution process monitored by diffraction spectroscopy. a,Vibration spectra with V_{bias} scaning from 0.2V to 1.5V. The deposited CTAB are dissolved when V_{bias} is scanned over 1 V, and the spectral features become similar to those of the origninal state as in Fig. 4-6c and d. **b**, The diffraction spectra display the similar behavior as that in Fig. 4-6c and indicate that most of deposited CTAB layers are dissolved and the electrochemical reaction is reversible.

4.6 Summary

We demonstrated vibration spectroscopy at the electrolyte/electrode interfaces using graphene grating electrodes. Its high detection sensitivity and interface specificity enables fast and in-situ monitoring of molecular vibrations at the electrochemical interface. In this proof-of-principle study we used CH_2 vibrations as an example, but the technique can be readily applied to other functional groups at different infrared frequency ranges. The diffraction spectroscopy enhances the relative contrast by ~ 50 times compared with conventional absorption spectroscopy. Currently we demonstrate a sub-monolayer detection sensitivity, which is mainly limited by our laser fluctuation. With improved laser stability and/or balanced detection, we envision that the technique can probe as low as about 1% of a monolayer coverage and provides a powerful tool to investigate fundamental processes at the electrolyte/electrode interfaces in active electrochemical cells.

Chapter 5

Sensing Spatio-Temporal Dynamics of Electric Field in Solution with Graphene

5.1 Introduction

Research into the generation and distribution of electric field dynamics in liquids and dielectrics is scientifically quite general, spanning basic research of bioelectric signaling [85–89] to applied engineering of lab-on-a-chip devices[90–94]. However, scalable non-perturbative observation of these electric field dynamics remains limited by the lack of an appropriate tool to resolve the voltage, spatial, and temporal fluctuations over a high dynamic range.

The development of bio-electric imaging and the application various optical imaging techniques to study the behavior of individual biological molecules and molecular assemblies in vitro and in live cells are of great interest for biological and neural science. One particular attracting field is detection of the electrical signals, including action potential voltages and local field potential, originated from the neuron, heart, and muscle cells[95–97]. It is well-known that, with the patch-clamp technique developed in standard electrophysiology, people can measure the electrical activity on a wide range of scales from single channel proteins, individual neuron cells, to whole organs such as the heart[98]. However, it is very difficult to scale up the patch-clamp electrodes to achieve simultaneous observation of a large number of cells while maintaining individual cell resolution. Therefore, the development of diverse bio-electrical imaging techniques is crucial for research in neural science.

Recent development in multi-electrodes arrays[88], [99–101] and various voltage sensitive dye techniques[102–104] addresses this scalability problem and these approaches have revolutionized the data collection in neural science. However, they are also facing other limitations. Multi-electrode arrays detection small extracellular potential through current amplification, but are less suitable for single cells resolution recording due to cross-talk between nearby channels. Many researcher are interested in voltage sensitive dyes recently as their fluorescence signals can reflect the action potential behavior and the optical measurements permits imaging many areas or volumes simultaneously. Yet the method unavoidably implants voltage sensitive dyes on cell membranes and this raises the question whether the biological behavior measured is an endogenous process

Therefore, a label-free method to image local electric fields in real time with high spatial and voltage sensitivity will be desired. Graphene provides unique doping-dependent optical properties and its two-dimensional nature suggests that the optical properties should be sensitive to the surrounding fluctuations. Graphene hence is a great candidate for optical sensor, especially in detection of small electrical potential variation. We explore different methods to further enhance the graphene sensitivity to electrical signals and show the possibility of using graphene as a complementary bioelectric signaling detection for neural science.

5.2 Bio-Electric Signal Detection and Graphene

Understanding the human brain is one of the greatest scientific challenges of our time. Its progress relies on a fundamental understanding on how a network of inter-connected neurons store and process information. Major research activities include the study of neuronal network formations and their purpose, the investigation of functions or dysfunctions of the brain using the imaging methods, and brain-computer interface research for neural prosthetics are still emerging fields. Their progress are highly dependent on the development of methods for imaging of the brain.

Neurons encode information by electrical signals. They receive input information in the form of miniature postsynaptic potentials mostly from dendrites; integrate signals from many synaptic responses with their intrinsic membrane potentials; and distribute output information in the form of action potentials through the axons[105,106]. Therefore, one of the most important tactics for decoding that information is to accurately record electric potentials generated by neurons.

Neural interfacing and prosthetics have shown promises to "read" the minds of the individuals and translate these thoughts into actions performed via a computer, which aims at restoring function in paralytics by providing the brain with new output pathways. Basic research is being conducted in our laboratory to develop novel non-invasive brain-computer interface systems, which can perform complex tasks reliably and efficiently. Functional neuron imaging approaches are also used to elucidate the neuroscience mechanisms underlying brain-computer interface applications, and for enhancing the performance of brain-computer interface.

Intercellular electrical activity is central to signaling and computation of excitable cells such as neuron, heart, and muscle cells. The voltages generated by bio-electric fields span three orders of magnitude and can fluctuate on the scale of microseconds to hours. As a result, the study of network-scale activity requires the ability to non-perturbatively record single-cell signals over a large field of view and at long time scales. Conventionally, there are two major classes of electrophysiology methods for recording action potentials with complementary capabilities – intracellular and extracellular recordings. Intracellular recording such as using patch clamps is the most sensitive method, but it is highly invasive

and its complex implementation usually limits the number of parallel recordings to neurons. Extracellular recording such as using multi-electrode arrays (MEAs)is non-invasive and permits parallel recording of 64-128 neurons, which is very useful in studying the behavior of network activities. However, multi-electrode array only records those neurons that happen to be in close contact with the electrodes. In addition, a hundred neurons are still a small fraction of the total number of neurons in a neuronal network. Therefore, the electrical detection of field dynamic in multi-electrode arrays is sensitive to small voltage fluctuations but challenging to parallelize and the spatial resolution of these techniques is limited to the distance between and the integrated area over the electrodes.

Our aim is to develop a novel technique to detect electric activities of neurons in a neuronal network in a highly parallel and non-invasive manner. Our detection technique exploits unique physical properties of graphene, whose optical transmission can be modulated by surface charge density (or gating voltage). This approach is fundamentally different from previous approaches in that electrical action potential is read out optically through voltage-sensitive optical transitions of graphene.

In contrast to electrical measurements, methods of optically imaging local electric field dynamics would open new opportunities for research and permit parallel and scalable detection of local electric field fluctuations across several orders of magnitude.
Here, we demonstrate optical imaging of local electric field dynamics with voltage sensitive spatio-temporal resolution across a wide field of view in non-equilibrium inhomogeneous solutions. With graphene-based platform, a high dynamic range, high sensitivity to voltage fluctuations, Hz-kHz frequencies, and nice spatial resolution over a wide field of view imaging technique could be designed.

Over the past decade, graphene's unique electronic and optical properties have been studied extensively. In addition to its exotic electronic behavior and ultrafast carrier relaxation dynamics, graphene couples strongly to light across both the visible and the infrared range, where absorption is given by $A = \pi\propto \sim 2.3\%$. This absorption can be controlled through electrostatic gating. The presence of a local electric field dramatically and rapidly modifies graphene's optical transitions by locally shifting the electronic Fermi level. A graphene-based optical sensor of electric field has several distinctive advantages over other materials:

(1) High sensitivity to gating voltage. Due to the low density of state of graphene near Dirac point, the Fermi energy changes dramatically with the gating voltage. The induced charge doping in the graphene causes the changes in graphene Fermi energy. Because the density of states of graphene near Dirac point is lower than typical metal electrodes, the Fermi energy is very sensitive to the induced charge doping. The huge Fermi energy shift in graphene can lead to a great optical properties modification.

(2) Ability to shift Fermi energy by gating. To use the induced charge doping in graphene to modulate the optical transitions, we want control the initial Fermi energy in graphene around half of the photon energy, a small amount of ion concentration at the electrode/electrolyte interface can already turn off the graphene optical transitions.

(3) High-speed operation. With a typical resistivity as low as 100Ω.□ at room temperature, the Fermi level and hence the optical absorptions of graphene can be rapidly modulated through the band-filling effect[107,108].

(4) Simple, cost-effective fabrication. With optical detection scheme, the devices do not require a elaborate photo-lithography for micro-electrodes. This simplifies the costly fabrication process and could become a more user-friendly technique for many biology labs.

Though this broadband absorption is strong for a single atomic layer, the 2.3%absorption is not ideal for many sensing and optoelectronic applications where one desires near-100% modulation. Recent studies has shown that by structuring graphene to access plasmon modes or integrating graphene with an optical waveguide, one can significantly improve the signal-to-noise ratio for various sensing purposes. We develop two different and novel methods, graphene grating diffraction and graphene-waveguide platform, to increase the optical modulation depth for a fixed voltage signal strength. With careful designs of our graphene platform, we obtain label-free methods to image local electric fields in real time with high spatial and voltage sensitivity.

5.3. Graphene Grating Electric Field Sensor

We propose a new optical sensing technique based on diffraction of graphene grating electrode that provides a non-invasive, high-spatial resolution, high sensitivity, fast-speed method which may enables sensitive and reliable detection of action potentials in the cultured neuron networks. A monolayer graphene is made into grating structure to further allow us to develop imaging techniques that greatly enhances the detection voltage sensitivity of electrical double layer and probes the biological processes involving ion-movement.

We demonstrate the possibility of electric field sensor based on graphene grating structure using voltage pulses generated from stimulating electrodes as a model system. By monitoring the diffraction intensity of the device, we observe the optical effects due to changes of potential at the electrical double layer.

5.3.1Experimental Design of Graphene Grating Sensor

We develop a novel optical sensing technique based on graphene grating electrodes to achieve high detection sensitivity for biological and chemical study. The experimental scheme is illustrated in Figure5-1a. An 1.55um diode laser is used as the light source, which produces stable light output in infrared range with minimal water absorption. To probe the electrical signal from cells at the electrolyte/graphene electrode interface, we measure the first-order diffracted infrared radiation from the graphene grating rather than the conventional transmission or reflection signal. The infrared radiation is focused on to a graphene grating at ~30 degree through a 20X microscope objective. The graphene grating is designed so that the 1st order diffraction light of 1.55um is normal to the sample and can be

collected by the objective. The reflected light from the grating is blocked by a blocker. After reflected by a D-shaped mirror, the 1st-order diffraction light from the graphene grating is sent to a InGaAs photodetector for light intensity measurement. An InGaAs camera is used to align the light path and observe the sample condition at the interface. Figure1b shows the real experiment layout in the lab. Attention to its simplicity and cost effectiveness.

Figure 5-1b shows a real picture of our measurement set-up. The incident light shines from the side of the objective and is focused with an oblique angle at the substrate holding the graphene grating. The incident angle is controlled so that diffraction signal will be close to the center of the objective. The reflection light is well separated from our diffraction signal, and can be blocked with a beam block. An external gate voltage Vg is used to set the graphene Fermi energy and to test the optical response of graphene grating diffraction to electrostatic gating. We choose a semiconductor laser at 1.55 micron as our light source because stable, high power lasers are readily available with their wide applications in telecommunication. The light is focused with a long working distance objective designed for near infrared light. The sample holder is paced on a 3D moving stage which allows fine tuning of the sample position. The diffraction light goes into an InGaAs camera which helps to locate cells and adjust the focus. After the system has been optimized, the camera is taken away, and the diffraction light is sent into a low-noise InGaAs detector for data recording.

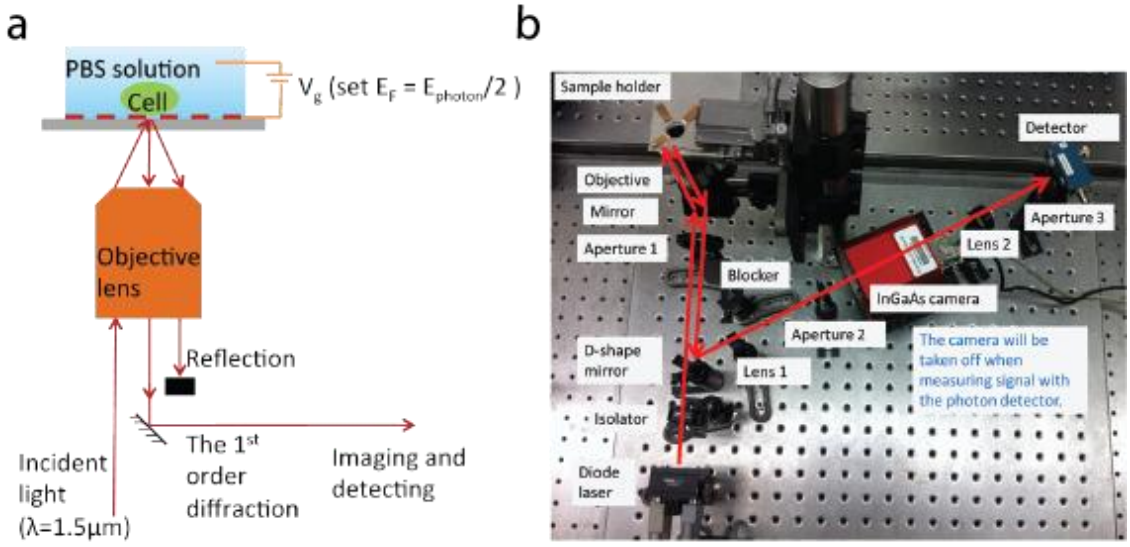

Figure 5-1 Experimental scheme with graphene grating sensor for action potential detection. a, Schematic showing using an single objective for illumination, blocking reflection light and collecting the 1st-order diffraction light. b, Real picture of our measurement set-up. 1.55um light is sent into the graphene grating sample with an objective. The 1st-order diffraction light is collected by the same objective and imaging into an InGaAs camera for electric potential detection.

The scheme described above is based on the diffraction signal from a graphene grating and the behavior of the diffraction signal is different from traditional techniques using reflection signal. The diffraction signal originates from the periodic variation of optical susceptibility at the interface and the ions concentration near graphene can affect the graphene optical susceptibility and generate signal to the light intensity. The bulk electrolyte solution beyond the nanometer thick double layer region, on the other hand, is homogeneous and contributes no diffraction signal. Therefore this diffraction scheme provides excellent interface specificity.

The diffraction scheme greatly enhances the detection sensitivity of the electrode-induced changes of ion concentration at the interface. In conventional infrared reflection measurements, the reflected light intensity I_{r}results from interference between the incident light and the backward reflection of radiation, i.e. $I_{\mathrm{r}} = \left|E_{\mathrm{sub}} + E_{\mathrm{gr}}\right|^2 \approx |E_{\mathrm{sub}}|^2 + 2 \cdot Re\left({E_{\mathrm{sub}}}^* \cdot E_{\mathrm{gr}}\right)$, where E_{sub} ,E_{gr} is reflected light electrical field from substrates, graphene radiation electrical field respectively. The relative intensity change due to light absorption from graphene is therefore determined by $\Delta I_{\mathrm{r}}/I_{\mathrm{r}} \approx 2 \cdot Re\left({E_{\mathrm{sub}}}^* \cdot E_{\mathrm{gr}}\right)/|E_{\mathrm{r}}|^2$. For a monolayer of material, $|E_{\mathrm{gr}}|$ from graphene is typically less than 10^{-2} of ${E_{\mathrm{sub}}}$[20].Therefore the reflection signal is usually ~10^{-2} of the background light, and requires special infrared spectrometer and long averages to obtain an reflection spectrum. In contrast, the diffracted signal in our detection scheme is simply due to the diffraction of graphene electrode(E_{g}). Therefore the relative intensity change can reach 100% from on to off state.

Another advantage of using the diffraction scheme is reducing the scattering light from cells. In conventional reflection microscopy, the scattered light due to bio-sample is mainly concentrated in the reflecting direction. Since the scattered light intensity of cells can be as large as the reflection light, this could be a major problem. Due to large background noise from cell scattering, the reflection signal is greatly immersed in the noise. However, in our diffraction scheme, the 1st order diffraction direction is well separated from the reflection light. Therefore, the scattered light is greatly reduced in the detection scheme.

The diffraction scheme, compared to the fluorescence and patch clamp method, also avoid expensive. time-consuming and precision-interfering labeling steps to mark analytes. Therefore, it is a promising approach to fast-detecting ion channel activity.

5.3.2 Characterization of Graphene Grating Sensor

We demonstrate the capability of this diffraction scheme based on graphene gratings by electrolyte gating in an electrochemical cell. The diffracted infrared light from the graphene grating are taken by a InGaAs photodiode after a focusing lens.

The figure 5-2a shows the graphene microribbons we fabricate on a microscope slide. The period of the ribbon is 4um and the aspect ratio is about 1:1 as we expected. The overall size of graphene microribbons is 2.5mm by 2.5mm, and the quality of the ribbons are in general

very good. The graphene ribbons are connect to the graphene itself, therefore we are able to use electrode to gate them and change their Fermi energy.

Figure 5-2b plots our experimental data on diffraction light intensity as a function of the gate voltage. A quantitative description of the gate-dependent diffraction signal can be given by considering both the real and imaginary part of graphene's dielectric constant. The most important feature here is a large change of the diffraction intensity at two threshold gate voltages corresponding to $|E_F|=E_{photon}/2$: the intensity of graphene grating diffraction is high at close to charge neutral point when optical transitions at 1.5 μm are allowed. The diffraction intensity decreases to almost zero when graphene is sufficiently electron or hole doped (i.e. $|E_F|>E_{photon}/2$) and the optical transitions in graphene are Pauli blocked. The overall diffraction intensity can change by almost 10 times with electrostatic gating, which is orders of magnitude higher than the 2% change observed in transmission. This large gate-induced modulation of diffraction signal is critical for sensitive voltage detection.

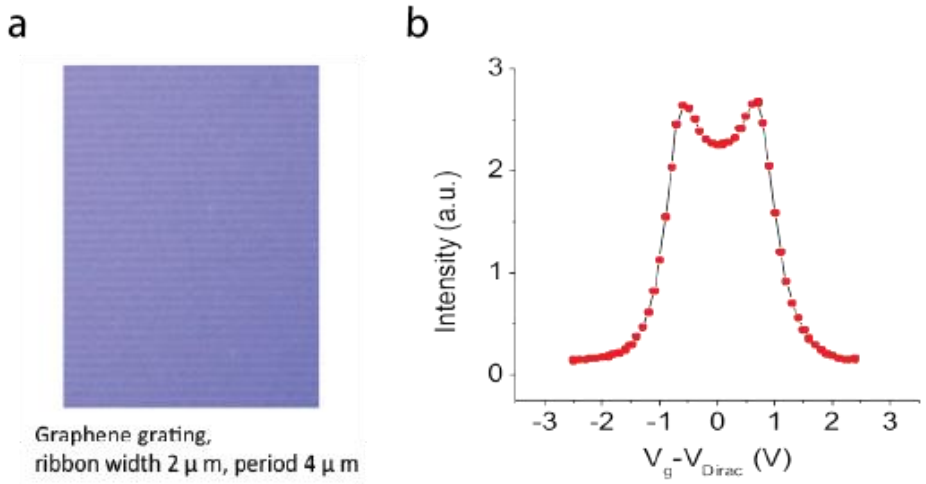

Figure 5-2 Experimental characterization of diffraction signal from graphene grating sensor in a PBS solution. a, An optical image of our fabricated graphene grating device. The image shows the quality of the ribbons is very nice. b, The measured diffraction light intensity as a function of the gate voltage from the graphene grating device. The modulated diffraction intensity can change by almost 10 times with electrostatic gating with a PBS solution.

When a neuron fires an action potential, it induces changes in the local ion concentration on the graphene surface, which generates a gate voltage change that is probed by a change in diffraction light intensity from the graphene grating. To detect the small action potential generated by neuron cells, we will set the graphene Fermi energy to the threshold point, i.e. $E_F=E_{photon}/2$. This Fermi energy is set by setting the external gate voltage V_g at ~0.9 V, which is well below the water electrolysis potential, and will not affect neuron behavior. A small input modulation voltage can lead to the largest optical diffraction output in our configuration.

Figure 5-3a illustrates the experimental condition to achieve maximum sensitivity for measuring small time-dependent voltage modulation. When a neuron fires an action potential, it induces changes in the local ion concentration on the graphene surface, which generates a gate voltage change and be probed by a change in diffraction light intensity from the graphene grating. To detect the small action potential generated by neuron cells, we will set the graphene Fermi energy to the threshold point, i.e. $E_F=E_{photon}/2$. This Fermi energy is set by having external gate voltage V_g at ~0.9 V, which is well below water electrolysis potential, and will not affect neuron behavior. A small input modulation voltage can lead to largest optical diffraction output in our configuration.

Figure 5-3b plots the data for measuring small time-dependent voltage modulation without cells. In this measurement, we apply a periodic rectangular waveform on the gate voltage with V_{pp} = 1mVand 100μV. We can observe clear periodic modulation of graphene grating diffraction signal at V_{pp} = 1mV. Even with the gate voltage at V_{pp} = 100μV, we can identify modulation of optical signal synced with the gate voltage, although it is close to the noise fluctuation. This smallest detectable voltage at 100μV is already quite good, and it can be significantly improved in an optimized configuration.

Extracellular action potential signals ranging from ~100-200μV in neurons to 500-1000μV in cardiomyocytes have been measured in extracellular recording using multi-electrode arrays.[85] We expect cells on graphene will exert a larger gating potential than the extracellular potential measured by MEA. This is because MEA electrodes are usually only partially covered by the cell, while graphene right underneath the neuron cells can be conveniently probed with the flexibility of optical microscopy. Therefore high-fidelity recording of action potential in neurons can be achieved if we can have a detection sensitivity at ~ 20μV with graphene gratings. In our configuration, 20μV gating voltage corresponds to a change of graphene charge density of 2×10^9 electrons/cm^2, and it can lead to a modulation of graphene grating diffraction intensity by 10^{-4}(based on the optical response function to gate voltage shown in Fig. 5-2b.) Although this is a small modulation, it is well within the detection limit of modern optical technology.

The ultimate limitation for detection sensitivity is set by photon shot noise. With a 2mW laser illumination on the graphene grating, we observe a diffraction light intensity at ~ 40nW. The corresponding photon shot noise is at 2 pW at 1kHz bandwidth. Therefore the smallest detectable modulation limited by the shot noise is at 5×10^{-5}.Beyond the shot noise, the detection sensitivity in real optical system is also constrained by the detector noise and laser fluctuation. At 1.5μm, a 0.1mm diameter InGaAs photodiode has noise equivalent detection power of 150 fW with 1kHz bandwidth. Therefore detection noise contributes a negligible relative intensity noise at about 4×10^{-6}.For action potential imaging.

Currently, the largest noise source in our optical configuration is the laser fluctuation, which has a relative intensity noise at 5×10^{-4} and limits our voltage sensitivity to 100μV. However, the laser noise can be readily improved by a close-loop stabilization to improve the laser stability. State-of-art close loop stabilization has achieved stable laser operation with relative intensity fluctuation less than 10^{-8}[109]. In comparison, our goal at fluctuation at than 10^{-4} should be readily achievable by incorporating a feedback photodiode and direct laser diode

current modulation. Second, a balanced detection with two photodiodes, where difference signal from the two photodiodes automatically eliminates the noise from laser fluctuation. With this improvement, we expect to achieve a voltage-sensitivity better than 20μV for high fidelity and high-speed recording of neuron action potential with light.

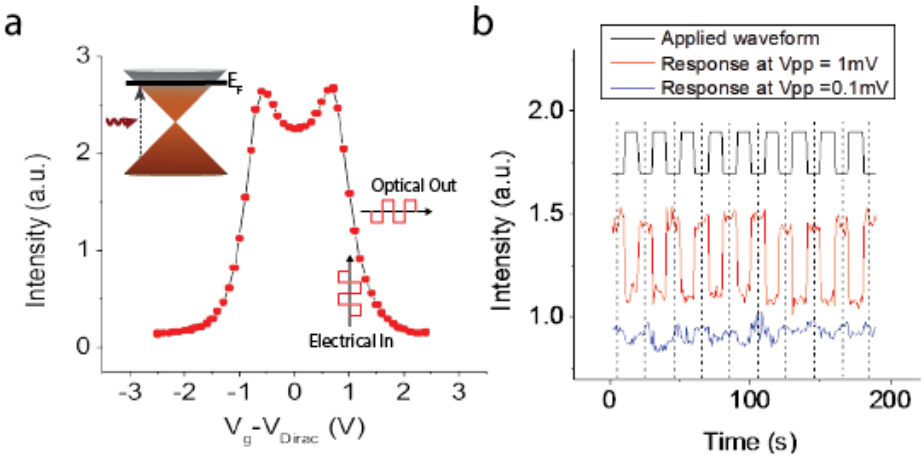

Figure 5-3 Experimental sensitivity characterization of graphene grating as an electric potential sensor in a PBS solution. a, Illustration of the experimental condition to achieve maximum sensitivity for measuring small time-dependent voltage modulation **b,** Experimental results of using graphene grating in PBS solution to detect small time-dependent voltage modulation. This smallest detectable voltage at 100μV is achievable which is dramatically improved from the traditional reflection scheme.

5.4 Graphene-Coupled Waveguide Device

Although the diffraction scheme of graphene grating device shows a promising approach to detection small voltage fluctuation in a solution, the application with in vitro cell organization is proven to be difficult. When neuron cells or cardiomyocite cells grow on the graphene grating surface, the optical response not only comes from the diffraction light of the graphene grating but also from the scattered light of the cell mediums. In our test trials with cell cultures, the images from InGaAs camera show that the diffraction light has a similar intensity compared to the scattered light from cell cultures. The additional background light originated from the cell medium scattering decreases the signal-to-noise ration of our detection and might prohibit the efficiency to detect action potential firing events.

In this section, we develop another method based on total internal reflection to address this problem. The total internal microscopy is typically used in biology where only a thin region of a specimen is under study. The evanescent electromagnetic field decays exponentially from the interface, and thus penetrates to a depth of only approximately 100 nm into the sample medium. The scattered light from cell medium can therefore be reduced while the surface specificity is also greatly improved. We integrate our sensor

material - graphene - with a planar waveguide to form a waveguide/solution total internal reflection interface for achieving optical electrical potential sensor compatible with in vitro cell cultures.

Though graphene's broadband absorption is strong for a single atomic layer, it is nevertheless limiting in the context of optoelectronic applications where one desires near-100% modulation. Recent research has demonstrated that by integrating graphene with an optical waveguide, one can significantly increase the interaction length between graphene and the propagating evanescent wave.[110–112]Different techniques have also been used to enhance light-matter coupling in graphene, such as photonic crystal cavities[113–116], plasmonics[110,117–119], and metamaterials[120–122].Here, we choose to couple graphene with a planar waveguide. With careful design of our waveguide and tuning the Fermi energy, we obtain the so-called critical coupling condition where the rate at which the propagating beam leaks out of the waveguide is equal to the rate of absorption into graphene[123,124]. In critical coupling condition, the ratio of the light coupled into the waveguide and the light absorbed by graphene reaches unity. In the context of our sensor, these design tactics permit a theoretically maximum and experimentally optimized sensitivity to fluctuations in the local electric field.

5.4.1 Working Principle of Critical Coupling Waveguide

We develop a novel waveguide coupling scheme based on critical coupling concept to enhance the graphene sensitivity to local potential changes in solutions. The structure of the waveguide-integrated graphene sensor is shown in Figure 5-4a. 150nm-thick Ta_2O_5 (n= 2.0856) layer acting as a waveguide is sandwiched between water(n=1.33) and 1000nm-thick SiO_2(n=1.4440) layer. An equilateral SF-11 glass(n = 1.7443) works as a substrate and coupler to the waveguide. Large area graphene grown by chemical-vapor-deposition is transferred on theTa_2O_5 surface and forms a electrochemical cell together with a Ag/AgCl or Pt/Ir counter-electrode and the aqueous electrolyte. The Fermi energy and hence the optical absorption of graphene can be modified by applying a voltage across counter- and graphene electrode to change the local electric potential. To probe the local electric potential at graphene-liquid interface, a collimated, 1.55μm, polarized infrared beam is coupled evanescently into the high-refractive index planar waveguide(Ta_2O_5 layer) through a prism and a low-refractive index layer(SiO_2 layer). The reflected light from the device is collected by an infrared objective and detected by an InGaAs photodiode.

Figure 5-4b shows the cross-section of the waveguide structure and reveals the concept of critical coupling. Here, a collimated,1.55μm incident light with transverse electric field polarization(TE mode) is sent into the waveguide structure at an oblique direction larger than critical angle for both SF11-SiO_2 surface(labeled as interface1) and Ta_2O_5-solution surface(labeled as interface2). Interface1 and Interface2, with reflection coefficient$|r_1|$ and $|r_2|$ close to 1, can be treated as two highly reflected mirrorsdue to total internal reflections.

To tackle the multilayer reflection problem, we can separate the system into two sub-systems: one consists SF11/SiO_2(1000nm)/Ta_2O_5 and other consists Ta_2O_5/Graphene/water as each of them forms a highly reflecting surface. The sub-systems are shown in Figure 5-4c. The SF11/SiO_2(1000nm)/Ta_2O_5 sub-system can be treated by standard methods in frustrated total internal reflection(FTIR). Here, we assume the reflection and transmission coefficients for light incident from the SF11 side are r_1' and t_1', while the coefficients from the Ta_2O_5 side are r_1 and t_1. One can prove that $|r_1| = |r_1'|$ and $t_1 t_1' = (1 - |r_1|^2)\exp(\delta_1 + \delta_1' + \pi)$[125],where δ_1 and δ_1' are the phase of $r_1$and r_1', respectively.

In the Ta_2O_5/Graphene/water sub-system, r_2 is defined as the reflection coefficient for light incident from Ta_2O_5 side at the interface. r_2 can be calculated with fresnel equation and perturbation theory on graphene absorption $r_2 = 1 - A_{gr} \times 1.66$, where A_{gr} is the absorption of graphene, r_2^0 is reflection coefficient at interface of Ta_2O_5/water without graphene.

Now, we consider the optical property of the combined system. As these two sub-systems are highly reflective, the combined structure consist of two parallel highly reflected mirrors and therefore forms a Fabry-Perot cavity. The total reflected radiation E_r is the interference of the multiple reflections and has the following form:

$$\frac{E_r}{E_0} = r_1' + t_1 t_1' r_2 e^{i\delta}\left[1 + \left(r_1 r_2 e^{i\delta}\right) + \left(r_1 r_2 e^{i\delta}\right)^2 + \cdots\right]$$
$$= r_1' + \frac{t_1 t_1' r_2 e^{i\delta}}{1 - r_1 r_2 e^{i\delta}} \qquad \text{Eq. 5-1}$$

,where E_0 is the incident electric field, $e^{i\delta}$ the phase accumulation during light travels in the Ta_2O_5 medium. With the relationship between r_1, r_1', t_1, t_1' derived previously, one can simplified the equation to

$$\frac{E_r}{E_0} = e^{i\delta'}\frac{|r_1| - |r_2|e^{i\Delta}}{1 - |r_1||r_2|e^{i\Delta}} \qquad \text{Eq. 5-2}$$

,where $\Delta = \delta + \delta_1 + \delta_2$ is the total phase accumulation for light travels a round trip in the waveguide. It is clear now the resonance of the Fabry-Perot cavity happens when $e^{i\Delta} = 1$, which is exactly the same requirement for the zeroth mode for Ta_2O_5 planar waveguide.[126] The phase accumulation Δ depends on incident angle sensitively, therefore we can find the resonance of Fabry-Perot cavity by varying the incident angle to the waveguide structure.

By squaring the Eq. 5-2, one can get the reflectance formula shown in Eq. 5-3 and the critical condition $|r_1| = |r_2|$, at which the reflection intensity diminished and all the lights are absorbed by graphene. These two parallel highly reflected mirrors form a Fabry-Perot cavity and show resonance behavior at a specific incident angle when the phase shift accumulation in Ta_2O_5 layer creates a destructive interference in reflection intensity. With 150nm-thick Ta_2O_5 layer, the resonance angle θ_{res} is at 60º as we designed. Similar to the analysis for Fabry-Perot cavity, one can show that the reflectance R in our optical system, considering the interference from all multiple reflections, can be described by:

$$R = \left|\frac{E_r}{E_0}\right|^2 = \frac{(|r_1|-|r_2|)^2}{(1-|r_1||r_2|)^2} \quad for\ resonance\ angle \qquad \text{Eq. 5-3}$$

,where E_0 is the incident electric field, E_r is the total electric field in the reflection direction. When the light incidents at the resonance angle, the reflection has a so-called "critical point" at $|r_1| = |r_2|$, where its intensity diminished and all the lights are absorbed by graphene.Note that $r_2$can be tuned by graphene Fermi energy and can be written as $|r_2| = 1 - A_{gr}(E_F) \times 1.66$ based on fresnel equation with Ta_2O_5-water interface at the resonant angle, where $A_{gr}(E_F)$ is the absorption of graphene at 1.55μm as a function of Fermi energy. Therefore, the reflection intensity can be used to monitor potential fluctuation on graphene.\

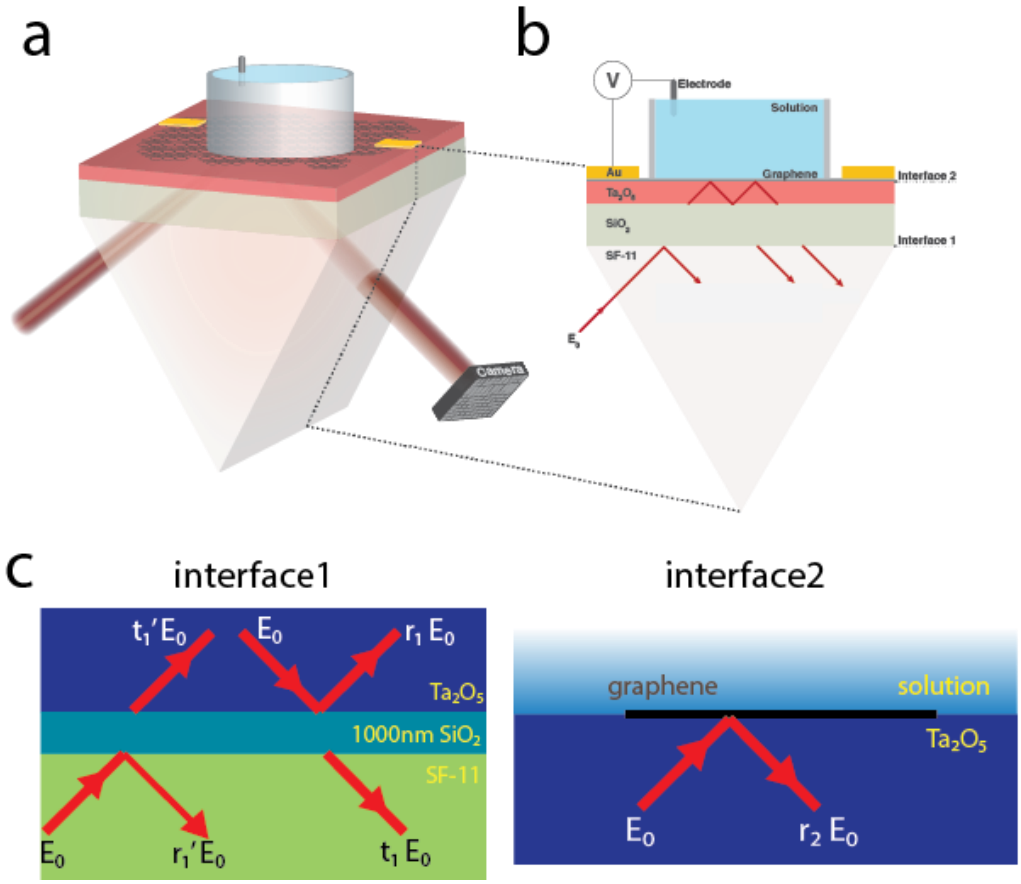

Figure 5-4 The illustration of device structure and graphene absorption measurement. a, The structure of the graphene-coupled waveguide device. The sensor device consists of a layer of graphene(black), high-refractive index planar waveguide(red layer), low-refractive index layer(gray layer), and a prism for coupling light. Ag/AgCl electrode is put in PBS solution for setting the graphene Fermi energy to optimize sensitivity for local potential detection. A collimated,1.55μm incident light with transverse electric field polarization(TE mode) is sent into the waveguide structure at an oblique direction and its reflection is detected by a InGaAs photodiode

or a InGaAs camera. **b**, The cross-section of the device structure. Interface1 and Interface2 form a Fabry-Perot cavity. The device operates at the so-called "critical point" where the multiple reflections destructively interfere resulting total reflection intensity diminished. The critical condition is violated when local electric field perturbation is in the presence due to corresponding graphene absorption change. One can then detection tiny local potential variation with large contrast by reflection measurement since the unperturbed reflection is essentially zero. **c**, Interface1 and interface2 are highly reflective and form a Fabry-Perot cavity. The definition of r_1',r_2,t_1,$t_1'$are given.

5.4.2 Optical Response of Critical Coupling Waveguide

To optimize the device structure, we built a custom Python simulation that explored materials, dimensions, tolerances, and coupling conditions to provide theoretical bounds on spatial resolution and potential sensitivity. The simulation is based on transfer-matrix formalism and is able to deal with multilayer reflection problems. These simulated conditions included polarization and coupling angle of the infrared beam, graphene's optical properties in aqueous solutions, and the structure of planar waveguide layers. Drawing upon these results we found the optimal parameters, compatible with standard fabrication techniques, for the spatial and charge sensitivity.

Figure 5-5a shows the reflection map of s-polarized planewaves with various wavelength of light and incident angles from a graphene-coated waveguide structure shown in Fig. 5-1a. Most of the wavelength and incident angle combination give unity reflection due to total internal reflection. Only when the incident angle matches with the zeroth transverse electric mode(TE mode), lights can couple into the waveguide and absorption of graphene is significant.

Fig. 5-5a shows the reflection of s-polarized planewaves at 1.55um from the same waveguide structure as a function of incident angles for different graphene Fermi energy. The dips in the reflection curves are due to the zeroth transverse electric mode of the waveguide and the depth of resonance dip changes significantly for different Fermi energies of graphene. The optical absorption of graphene decreases monotonically with the Fermi energy and determines the fraction of light being absorbed in the waveguide. The simulation indicates that the strongest (deepest) resonance takes place at one specific Fermi energy (376 meV in Figure5-5b). At this Fermi energy, the absorption of graphene is such that the multiple reflections in the waveguide destructively interfere, resulting in a near-zero reflection of the probe beam.

Finally, we simulate reflectance in a real experimental setting where the incident angle is fixed at the resonance condition and assuming numerical aperture N.A. = 0.002 by averaging the reflectance within the angle divergence(~0.6º). The absorption of graphene used in the simulation is taken from a direct reflection experimental data. The simulated voltage-

dependent reflectance and responsitivity of the device is shown in fig. 5-5c as yellow and green lines, respectively.

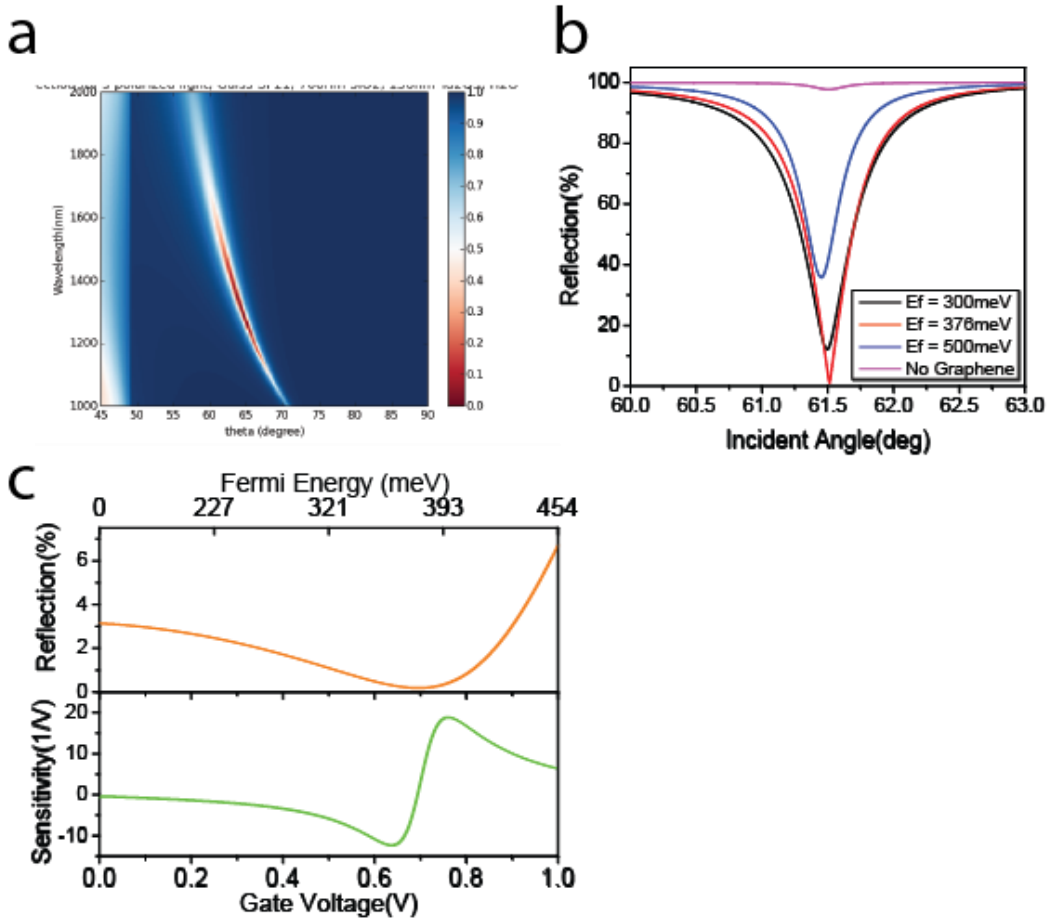

Figure 5-5 Simulation of optical responses from waveguide devices. a, Reflectance map of s-polarized planewaves with various wavelength of light and incident angles from a graphene-coated waveguide structure shown in Fig. 5-4. Reflectance is reduced due to absorption of graphene only when the incident angle matches with 0^{th} TE mode of the waveguide. **b,** Reflectance as a function of incident angles for different graphene Fermi energy. The depth of resonance dip can be controlled by the graphene Fermi energy. **c,** Simulated voltage-dependent reflectance and responsitivity of the graphene-waveguide device.

5.4.3 Critical Coupling Condition

Operating the device at the critical condition can enhance the contrast significantly due to low reflection background. Previous studies of doped graphene spectroscopy[75]show that $A_{gr}(E_F)$ is a constant 2.3% for low fermi energy and monotonically vanishes for higher

fermi energy as the band-filling effect comes into play. The tunable range of graphene absorption is from 0.5% to 2.2 % with little electrochemical reactions, suggesting $|r_2|$ can be tuned from 99% to 96.3%. We design the thickness of SiO_2 layer to be 1000nm making the total internal reflection at interface1 slightly frustrated and resulting $|r_1| = 98.2\%$. Since $|r_1|$ is in the tuning range of $|r_2|$, we then apply an external gate to modify graphene absorption such that $|r_1| = |r_2|$ which is expected to happen when $E_F \sim 400meV$. Once the critical condition is achieved, all the lights are absorbed by graphene and the reflection intensity from the device can be zero theoretically. With the presence of local electric field perturbations, the critical condition is violated due to corresponding graphene absorption change and the reflection intensity become non-vanished. One can detection small local potential variation with large contrast by reflection measurement since the unperturbed reflection is essentially zero.

Fig.5-6a shows the experimental data for reflectance of TE-polarized, collimated 1.55μm beam incident at the resonance angle of the fabricated waveguide as a function of gating with Ag/AgCl electrode in phosphate-buffered saline(PBS) solution. The reflectance is constant close to charge neutral point of graphene ($V_{cnp} = -0.14V_g$) as r_2 is smaller than r_1. As the Fermi energy of graphene increases, the reflectance shows a dip at $+0.41V_g$ and $-0.69V_g$ indicating r_2 equals to r_1 and the critical coupling condition is achieved. With even higher gating voltages, the reflectance increases again since $r_2$becomes larger than r_1. The simulated curve with experimental determined graphene absorption in PBS is shown in figure 5-6a as gray dash line, and align well with the experimental reflectance curve except the simulated curve is slightly wider possibly due to sample variation in double layer capacitance. The lowest reflectance we achieved is 0.63% at $+0.41V_g$ and such a low reflectance enable the device to work as a sensitive potential sensor. The nonzero reflectance at the correct optical absorption comes from divergence of infrared beam, non-uniformity of CVD-grown graphene absorption or the imperfect deposition process in waveguide manufacturing.

The responsitivity of the device is determined by the reflection contrast change due to a modulated gating voltage and can be characterized by dR/R.dV where dV is the magnitude of small modulating gate voltage, R the reflectance, dR the change of reflectance due to voltage modulation. The corresponding dR/R.dV of our device is shown in Fig. 5-3b. The responsitivity curve has a maximum value of 1.2%/mV at $V_g = +0.53V$. With a commercially available 10mW 1.55um butterfly diode laser, we find the laser fluctuation noise can be limit within 0.015%(root-mean-square) for bandwidth from 10Hz to 10kHz without much efforts. With such a sensitivity, we estimate the detection limit of our device is around 12μV.From the absorption of graphene, we estimate that the responsitivity in a transmission configuration dT/T.dV = 0.0048%/mV due to intrinsic broadening of graphene interband transitions. Therefore, the graphene sensor integrated with waveguides can increase the interaction length of light with graphene and enhance the responsitivity by 250 times.

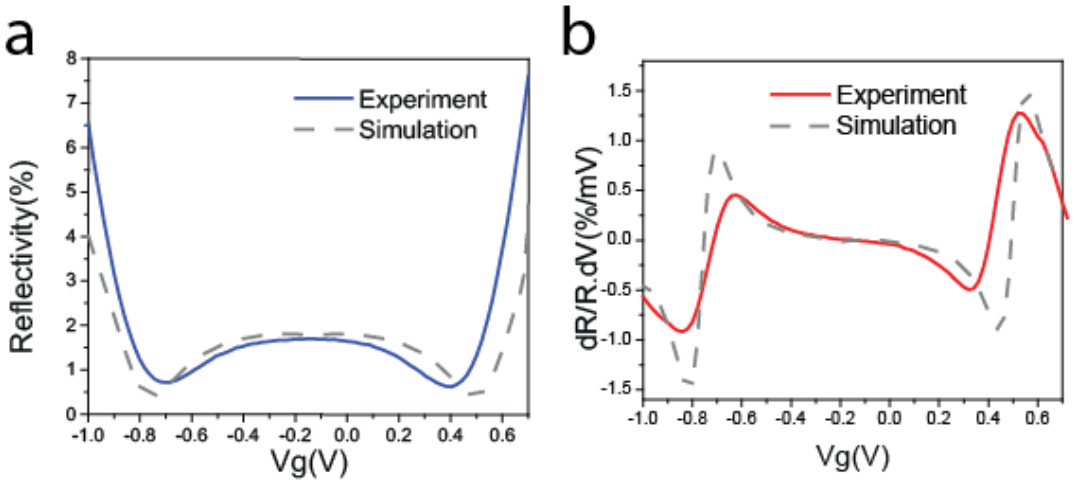

Figure 5-6 Optical responses from graphene-waveguide devices. a, Reflectance measurement of TE-polarized, collimated 1.55um beam incident at the resonance angle of the fabricated waveguide as a function of gating with Ag/AgCl electrode in PBS solution. Reflectance shows a dip corresponding to the critical condition. The simulated curve with graphene absorption from independent experiment is shown as gray dashed line. **b**, The responsitivity dR/R.dV derived from (**a**) for experiment(red) and simulation(gray dashed). The maximum responsitivity of our device is found to be 1.2%/mV at V_g = +0.53V.

5.4.4 Small Signal Analysis

To demonstrate the capability of detecting small fluctuation of electric field in solutions, we simulated a small time-dependent voltage modulation to test the bounds of our charge sensitivity. The optimal Fermi energy of graphene(V_g= 0.53 V) and the incident beam angle determined by the previous test at in Fig. 5-3 are used during the small modulation is applied. In this measurement, we apply a periodic rectangular waveform on the gate voltage with peak-to-peak voltage ranging from 500μV to 100 μV and record the reflection with a band-pass filter from 10Hz to 10kHz. The resulting reflection modulation is recorded and shown in Fig. 5-4a. The dR/R for 500μV, 200μV, and 100μV modulation are 0.58%,0.23%, 0.11%, respectively and agrees well with the dR/R.dV = 1.2%/mV at 0.53V shown in figure 2b. For data at Vpp =100μV,we can observe clear periodic modulation of reflection signal and the signal-to-noise ratio is calculated to be 6.5 which indicate a detection limit of ~ 15μV, or equivalently 2.3×10^8 electron/cm^2.

The response speed of our device is also tested by applying 1mVppsinusoidal waveforms with different frequencies. To have well-defined resistance and capacitance, we use photolithography technique to defined the exposed graphene area by a 200μm×400μm rectangular opening. The magnitude of dR/R for frequency from 20Hz to 50kHz is measured and shown in Fig. 5-4b. The magnitude of dR/R stays a constant up to ~10kHz and decays rapidly for higher frequency. The low-pass behavior can be explained by an equivalent

circuit consisted of interfacial capacitance and resistance of graphene in series. The resulting fitted curve with this simple model(dashed curve in Fig. 5-4b) is described by 1.4% / (1+ f/19000Hz) and agrees well with experimental data. The RC constant of 50μs is compatible with graphene resistance R~ 6kΩ and interfacial capacitance C~ 0.022F/m^2. We demonstrate that the high conductivity of graphene makes our device operate at frequency up to at least 10kHz which already covers many dynamics of electrical signals including neuron and cardiomyocite action potential[85,88,89] and various electrophoresis processes[93,127,128].

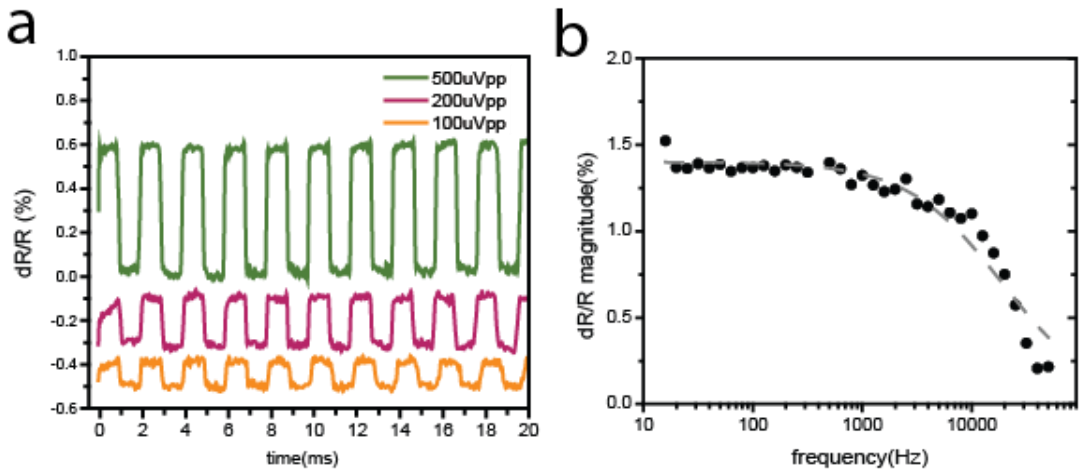

Figure 5-7 Small signal analysis of optical readout to determine device sensitivity and speed. a, Reflectance change of the infrared beam at critical condition due to small periodic rectangular waveform applying on the Ag/AgCl electrode with peak-to-peak voltage 500μV_{pp}(green), 200μV_{pp}(purple)and100 μV_{pp}(orange). A bandpass filter from 10Hz to 10kHz is applied. The data for 100μV modulation shows a signal-to-noise ratio SN= 6.5 which indicate a detection limit of ~ 15μV. **b**, Reflectance modulation of a device with well-defined exposed graphene area(80,000μm^2) due to 1mV_{pp} periodic sinusoidal waveform applying on the Ag/AgCl electrode with frequency ranging from 20Hz to 50kHz. High-speed operation up to 10kHz is demonstrated and is the consequence of high conductivity of graphene film. The fitted curve with simple equivalent circuit model including double-layer capacitance and resistance in graphene is shown with gray dashed line.

5.5 Simulation of Electric Potential Dynamics in Solution

Here, we digress a little to understand the spatio-temporal behavior of local potential produced in micro-electrode stimulation, neuron action potential, or microfluid systems. We use the Electrochemistry Module in COMSOL Multiphysics to simulate the electric potential

in solution during voltage pulses applied. The simulation accounts the effect of the electrode kinetics in addition to solution resistance. The current distribution in electrolyte is assumed to obey Ohm's law and the electrode interface are simulated by a double-layer capacitance together with a linearized Butler–Volmer equation to describe electrode current, namely:

$$i_{el} = i_0 \frac{\alpha F}{RT} \eta \qquad \text{Eq. 5-4}$$

, where i_{el} is the electrode current, i_0 the exchange current density, α the cathodic and anodic charge transfer coefficient, F the faraday constant, R the gas constant, T the temperature and η the overpotential of the electrode.
In the simulation, we use a 1μm-radius-disk stimulating electrode with C = 10F/m^2, i_0 = 20A/m^2, α = 1 embedded in an electrolyte with conductivity σ = 0.00022 S/m. (The parameters for stimulating electrode are provided by the manufacturer and electrolyte conductivity is from literature[129]) Large-area graphene is put 50um away from the stimulating electrode and with parameters: C = 0.02F/m^2 and i_0 = 0.05A/m^2. Both graphene and stimulating electrode are set at 0V in the beginning and a 50ms pulse with 1V magnitude is applied to the stimulating electrode. The cross-section of simulation geometry is shown in Fig. 5-8a.Fig. 5-8b shows the simulated spatial distribution of electrolyte potential at t = -1ms, 1ms, 3ms and 5ms during the voltage pulse applied. One can see the dynamics of potential propagating through the solution.

It is well-known in electrophysiology that the local electric potential φ(r) in electrolyte in ms time scale decays as the position moves away from the stimulating electrode and can be characterized by[87]:

$$\varphi(r) = \frac{1}{4\pi\sigma} \frac{i_{el}}{r} \qquad \text{Eq. 5-5}$$

,wherei_{el} is the point source current from the stimulating electrode, r the distance between the point source and the measuring position, σ the conductivity of the electrolyte.

Fig. 5-8c shows the integrated current at the stimulating electrode during the 50ms pulse. The stimulating voltage generates a ~10ms transient current due to the high-pass nature of the capacitance at stimulating electrode interface. The transient current quickly decay to a stationary current as the current flow in electrolyte reach to an equilibrium state. Fig. 5-8d shows the potential dynamics in solution just above graphene for three positions corresponding to A1(below the tip), A2(200μm away) and A3(400 μm away) shown in Fig.5-9b. The potential waveform possess the same dynamics as the electrode current in Fig. 5-8c and one can also quantitatively verifies Eq. 5-5 is valid.

The simulation without graphene in presence is also shown in Fig. 5-8d as dashed lines. The comparison shows that the local potential difference with or without graphene are within 10% which means graphene can be treated as a non-perturbed detection scheme due to little electrochemistry happens at the graphene interface.

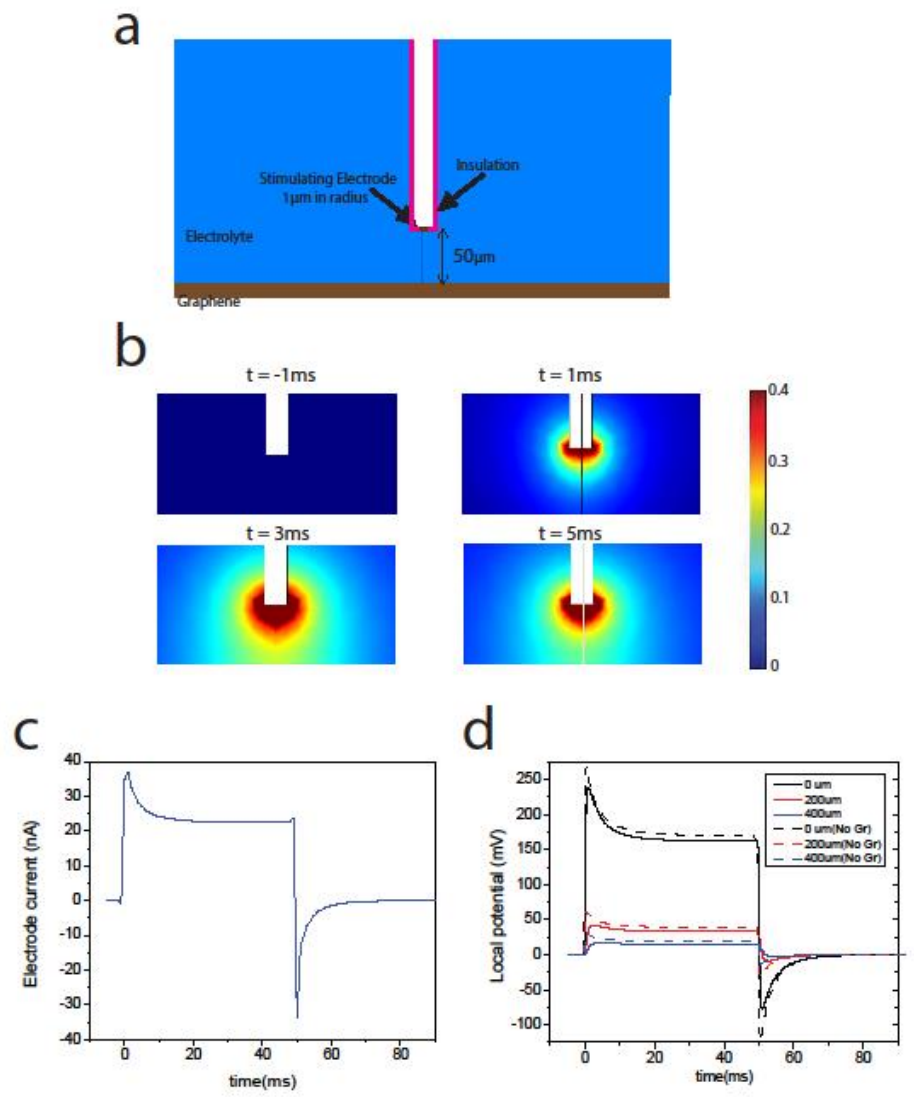

Figure 5-8 Finite-element simulation for micro-eletrode voltage pulsing. a, Cross-section of simulation geometry and the equivalent circuit. **b,** Color map of simulated spatial distribution of electrolyte potential at t = -1ms, 1ms, 3ms and 5ms during the voltage pulse applied. **c,** Integrated current at the stimulating electrode during the 50ms pulse. **d,** Dynamics of local potential (solid) in electrolyte just above graphene for positions corresponding to A1(below the tip), A2(200μm away) and A3(400 μm away) shown in Fig.5-9b. The same quantity without graphene(dashed) is also shown for comparison. The simulation gives a qualitative description for the spatio-temporal phenomenon seen in experiment.

5.6 Imaging Spatio-Temporal Dynamics in Solution

Next, we demonstrate the imaging capability of our device with time-varying voltage from stimulating electrode in 1mg/L NaCl aqueous solution as an example. The stimulating electrode is made of platinum/iridium tip covered with parylene insulation cladding and only 2um length close to tip is exposed. The electrode is placed 50μm away from graphene as shown in Fig. 5-9a. The infrared image of graphene plane (Fig. 5-9b) is formed by a long-working-distance near-infrared objective and an InGaAs camera. The red spot in Fig. 5-9b indicates where the stimulating electrode is located.

To start with, we choose three areas(50um×100um) shown in blue circles A1,A2 and A3 by apertures and send the reflected light to an InGaAs photodiode. The measured reflection signal is shown in Fig. 5-9c while a 50ms pulse with 1V magnitude applied (top inset)to resemble the stimulation experiment done in previous simulation. The reflection signal is converted to local potential with a calibration curve measured by AgCl/Ag electrode where the voltage drop at electrode-solution interface is negligible. The local potential from A1 area shows a ~6ms transient voltage and quickly decay to a stationary potential while A2 and A3 area show a smaller transient voltage and stationary potential.

The behavior can be explained by previous finite-element simulation or by a simple equivalent circuit shown in Fig. 5-9d. The experimental data of local potential dynamics can be compared with the simulation in Fig. 5-9c. The equivalent circuit consists of impedance from electrode-solution interface, resistance from solution, and impedance from graphene-solution interface. The value of each resistance and capacitance are close to their real value estimated from other experiments. The stationary potential can be understood as stationary state of the circuit where the capacitor are fully charged and the transient voltage is due to the charging process of capacitors. The dynamical solution of the equivalent circuit is also shown as dashed curves in Fig. 5-9d for comparison.

At last, we demonstrate the imaging capability by observing the same experimental condition with InGaAs camera at frame rate 80Hz. Fig. 5-9e shows a sequence of images of reflection intensity during the voltage pulse is applied normalized to that without stimulation and the integrated period of each frame is illustrated in the lower inset of Fig. 5-8c. Frame 1 and frame 5 integrate over the transient voltage and show larger positive dR/R and negative dR/R, respectively. Frame 2-4 integrate over the stationary potential period and show the spatial distribution of the electrical potential in solution. Frame 6-8 show the decay of electrical potential after the pulse. The sequence of images confirms both the transient voltage and stationary potential observed previous by photodiodes and indicates the spatial-temporal dynamics can be monitored in real time. Unfortunately, the frame rate of the InGaAs camera is too slow to resolve the fine dynamics of the transient voltage, but one can expect to have better time resolution with commercially available high-frame-rate camera(~1000Hz).

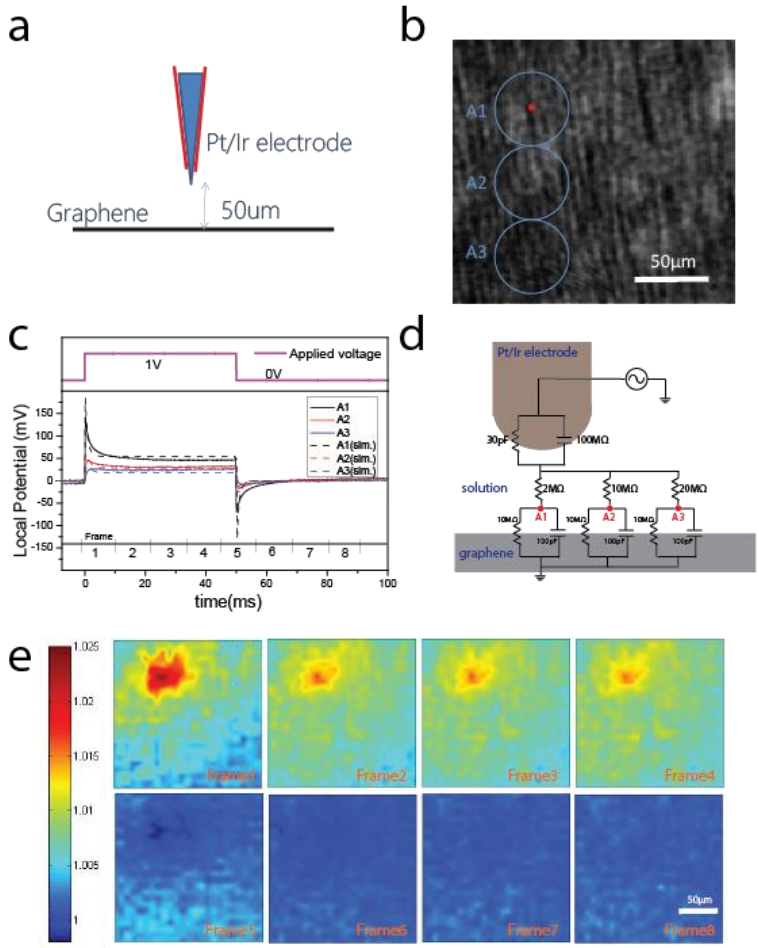

Figure 5-9 Demonstration of the imaging capability with micro-electrode as stimulation. **a**, Geometry of experiment setup. A platinum/iridium micro-electrode is placed 50μm away from graphene in 1mg/L NaCl solution. **b**, Image of graphene plane taken by an InGaAs camera. The red spot indicates where the stimulating electrode is located and blue circles A1,A2 and A3 show the integrating areas in photodiode measurements. **c**, The local potential for A1(black),A2(red) and A3(blue) derived from measured reflection signal with a 50ms pulse(top inset) with 1V magnitude applied. **d**, Simplified equivalent circuit to qualitatively describe the spatio-temporal dynamics shown in (**c**,**e**). **e**, Video taken by an InGaAs camera at frame rate 80Hz while the same pulse in (**c**) is applied. The sequence of images of reflection intensity is normalized to that without stimulation and the integrated time interval of each frame is illustrated in the lower inset of (**c**).The video confirms the spatial-temporal dynamics can be monitored in real time with our graphene-waveguide device.

5.7 Summary

We first developed a diffraction-based detection scheme with graphene grating structures that allows wide-field imaging and high-sensitivity measurements of electric field in solution at the same time. The technique makes use of the fact that monolayer graphene opto-electronic property is sensitive to surrounding electric field. We demonstrate the sensitivity is enhanced compared to transmission measurements and the detectable level is equivalent to 100μV. However, the integration with in-vitro cell culture is proven to be difficult due to scattered light from cell medium.

Later, we address this problem by developing an total internal reflection optical detection scheme with waveguide-integrated graphene that allows wide-field imaging and high-sensitivity measurements of electric field in solution at the same time. Through integrating graphene with an innovative planar waveguide structure, the sensitivity is enhanced due to multiple reflections in the waveguide layer. In this proof-of-principle study we used voltage modulation from an excitation electrode as an example. The sensitivity is enhanced by 250 times compared to transmission measurements and the detectable level is equivalent to 15μV with bandwidth of 10Hz-10kHz. We also show that the imaging capability of our device can be used to monitor spatial-temporal dynamics of electric field in real time and has potentially applications in studying various electrophoresis processes and biological electrical signaling. With the advance of two dimensional materials research, the novel waveguide coupling method we developed can readily be applied to other materials to create a total absorber and have potentials to construct opto-electronics with various purposes.

References

[1] K. S. Novoselov, A. K. Geim, S. V. Morozov, D. Jiang, M. I. Katsnelson, I. V. Grigorieva, S. V. Dubonos, and A. A. Firsov, "Two-dimensional gas of massless Dirac fermions in graphene," *Nature*, vol. 438, no. 7065, pp. 197–200, Nov. 2005.

[2] Y. Zhang, Y.-W. Tan, H. L. Stormer, and P. Kim, "Experimental observation of the quantum Hall effect and Berry's phase in graphene," *Nature*, vol. 438, no. 7065, pp. 201–204, Nov. 2005.

[3] M. I. Katsnelson, K. S. Novoselov, and A. K. Geim, "Chiral tunnelling and the Klein paradox in graphene," *Nat Phys*, vol. 2, no. 9, pp. 620–625, Sep. 2006.

[4] V. Ryzhii, A. Satou, and T. Otsuji, "Plasma waves in two-dimensional electron-hole system in gated graphene heterostructures," *J. Appl. Phys.*, vol. 101, no. 2, p. 024509, 2007.

[5] J. M. Dawlaty, S. Shivaraman, J. Strait, P. George, M. Chandrashekhar, F. Rana, M. G. Spencer, D. Veksler, and Y. Chen, "Measurement of the optical absorption spectra of epitaxial graphene from terahertz to visible," *Appl. Phys. Lett.*, vol. 93, no. 13, p. 131905, 2008.

[6] H. Choi, F. Borondics, D. A. Siegel, S. Y. Zhou, M. C. Martin, A. Lanzara, and R. A. Kaindl, "Broadband electromagnetic response and ultrafast dynamics of few-layer epitaxial graphene," *Appl. Phys. Lett.*, vol. 94, no. 17, p. 172102, 2009.

[7] Z. Q. Li, E. A. Henriksen, Z. Jiang, Z. Hao, M. C. Martin, P. Kim, H. L. Stormer, and D. N. Basov, "Dirac charge dynamics in graphene by infrared spectroscopy," *Nat. Phys.*, vol. 4, no. 7, pp. 532–535, Jun. 2008.

[8] F. Wang, Y. Zhang, C. Tian, C. Girit, A. Zettl, M. Crommie, and Y. R. Shen, "Gate-Variable Optical Transitions in Graphene," *Science*, vol. 320, no. 5873, pp. 206–209, Apr. 2008.

[9] P. R. Wallace, "The Band Theory of Graphite," *Phys. Rev.*, vol. 71, no. 9, pp. 622–634, May 1947.

[10] A. H. . Neto, F. Guinea, N. M. R. Peres, K. S. Novoselov, and A. K. Geim, "The electronic properties of graphene," *Rev. Mod. Phys. Rev Mod Phys*, vol. 81, no. 1, p. 109, 2009.

[11] V. P. Gusynin and S. G. Sharapov, "Transport of Dirac quasiparticles in graphene: Hall and optical conductivities," *Phys. Rev. B*, vol. 73, no. 24, Jun. 2006.

[12] "Experimental observation of the quantum Hall effect and Berry's phase in graphene : Abstract : Nature." [Online]. Available: http://www.nature.com/nature/journal/v438/n7065/abs/nature04235.html. [Accessed: 08-Feb-2011].

[13] T. Ando, Y. Zheng, and H. Suzuura, "Dynamical Conductivity and Zero-Mode Anomaly in Honeycomb Lattices," *J. Phys. Soc. Jpn.*, vol. 71, no. 5, pp. 1318–1324, May 2002.

[14] D. Svintsov, V. Ryzhii, and T. Otsuji, "Negative dynamic Drude conductivity in pumped graphene," *Appl. Phys. Express*, vol. 7, no. 11, p. 115101, 2014.

[15] M. Polini, A. H. MacDonald, and G. Vignale, "Drude weight, plasmon dispersion, and pseudospin response in doped graphene sheets," *arXiv*, vol. 901, 2009.

[16] Y.-W. Tan, Y. Zhang, K. Bolotin, Y. Zhao, S. Adam, E. H. Hwang, S. Das Sarma, H. L. Stormer, and P. Kim, "Measurement of Scattering Rate and Minimum Conductivity in Graphene," *Phys. Rev. Lett.*, vol. 99, no. 24, p. 246803, 2007.
[17] N. Peres, J. Lopes dos Santos, and T. Stauber, "Phenomenological study of the electronic transport coefficients of graphene," *Phys. Rev. B*, vol. 76, no. 7, Aug. 2007.
[18] E. Hwang, S. Adam, and S. Sarma, "Carrier Transport in Two-Dimensional Graphene Layers," *Phys. Rev. Lett.*, vol. 98, no. 18, May 2007.
[19] J.-H. Chen, C. Jang, S. Adam, M. S. Fuhrer, E. D. Williams, and M. Ishigami, "Charged-impurity scattering in graphene," *Nat. Phys.*, vol. 4, no. 5, pp. 377–381, Apr. 2008.
[20] A. Lherbier, X. Blase, Y.-M. Niquet, F. Triozon, and S. Roche, "Charge Transport in Chemically Doped 2D Graphene," *Phys. Rev. Lett.*, vol. 101, no. 3, Jul. 2008.
[21] K. Nomura and A. H. MacDonald, "Quantum Transport of Massless Dirac Fermions," *Phys. Rev. Lett.*, vol. 98, no. 7, p. 076602, 2007.
[22] X. Hong, K. Zou, and J. Zhu, "Quantum scattering time and its implications on scattering sources in graphene," *Phys. Rev. B*, vol. 80, no. 24, Dec. 2009.
[23] T. Ando, "Screening Effect and Impurity Scattering in Monolayer Graphene," *J. Phys. Soc. Jpn.*, vol. 75, p. 074716, 2006.
[24] K. F. Mak, M. Y. Sfeir, Y. Wu, C. H. Lui, J. A. Misewich, and T. F. Heinz, "Measurement of the Optical Conductivity of Graphene," *Phys. Rev. Lett.*, vol. 101, no. 19, Nov. 2008.
[25] Y. Zhang, T.-T. Tang, C. Girit, Z. Hao, M. C. Martin, A. Zettl, M. F. Crommie, Y. R. Shen, and F. Wang, "Direct observation of a widely tunable bandgap in bilayer graphene," *Nature*, vol. 459, no. 7248, pp. 820–823, Jun. 2009.
[26] X. Li, W. Cai, J. An, S. Kim, J. Nah, D. Yang, R. Piner, A. Velamakanni, I. Jung, E. Tutuc, S. K. Banerjee, L. Colombo, and R. S. Ruoff, "Large-Area Synthesis of High-Quality and Uniform Graphene Films on Copper Foils," *Science*, vol. 324, no. 5932, pp. 1312–1314, May 2009.
[27] J. Liu, Q. Qian, Y. Zou, G. Li, Y. Jin, K. Jiang, S. Fan, and Q. Li, "Enhanced performance of graphene transistor with ion-gel top gate," *Carbon*, vol. 68, pp. 480–486, Mar. 2014.
[28] P. Sharma and Z. L. Miıfmmode \checks\else š\fikoviıfmmode \acutec\else ć\fi, "Capacitance of graphene in aqueous electrolytes: The effects of dielectric saturation of water and finite size of ions," *Phys Rev B*, vol. 90, no. 12, p. 125415, Sep. 2014.
[29] R. R. Nair, P. Blake, A. N. Grigorenko, K. S. Novoselov, T. J. Booth, T. Stauber, N. M. R. Peres, and A. K. Geim, "Fine Structure Constant Defines Visual Transparency of Graphene," *Science*, vol. 320, no. 5881, pp. 1308–1308, Jun. 2008.
[30] X. Yu, Y. Shen, T. Liu, T. (Tom) Wu, and Q. Jie Wang, "Photocurrent generation in lateral graphene p-n junction created by electron-beam irradiation," *Sci. Rep.*, vol. 5, p. 12014, Jul. 2015.
[31] C.-F. Chen, C.-H. Park, B. W. Boudouris, J. Horng, B. Geng, C. Girit, A. Zettl, M. F. Crommie, R. A. Segalman, S. G. Louie, and F. Wang, "Controlling inelastic light scattering quantum pathways in graphene," *Nature*, vol. 471, no. 7340, pp. 617–620, Mar. 2011.
[32] M. Koshino and T. Ando, "Minimum Conductivity in Bilayer Graphene," *Phys. Semicond. Part A*, vol. 893, pp. 621–622, 2007.

[33] M. M. Fogler, D. S. Novikov, and B. I. Shklovskii, “Screening of a hypercritical charge in graphene,” *Phys. Rev. B*, vol. 76, no. 23, Dec. 2007.
[34] A. Shytov, M. Katsnelson, and L. Levitov, “Atomic Collapse and Quasi–Rydberg States in Graphene,” *Phys. Rev. Lett.*, vol. 99, no. 24, Dec. 2007.
[35] M. van Exter and D. Grischkowsky, “Carrier dynamics of electrons and holes in moderately doped silicon,” *Phys Rev B*, vol. 41, no. 17, pp. 12140–12149, Jun. 1990.
[36] S. Adam, E. H. Hwang, V. M. Galitski, and S. Das Sarma, “A self-consistent theory for graphene transport,” *Proc. Natl. Acad. Sci.*, vol. 104, no. 47, p. 18392, 2007.
[37] N. Peres, F. Guinea, and A. Castro Neto, “Electronic properties of disordered two-dimensional carbon,” *Phys. Rev. B*, vol. 73, no. 12, Mar. 2006.
[38] J. Kim, H. Son, D. J. Cho, B. Geng, W. Regan, S. Shi, K. Kim, A. Zettl, Y.-R. Shen, and F. Wang, “Electrical Control of Optical Plasmon Resonance with Graphene,” *Nano Lett.*, vol. 12, no. 11, pp. 5598–5602, Nov. 2012.
[39] K. Stelmaszczyk, M. Fechner, P. Rohwetter, M. Quei\s ser, A. Czy\.zewski, T. Stacewicz, and L. Wöste, “Towards Supercontinuum Cavity Ring-Down Spectroscopy,” *Appl. Phys. B*, vol. 94, no. 3, pp. 369–373, 2008.
[40] I. J. Finkelstein, J. Zheng, H. Ishikawa, S. Kim, K. Kwak, and M. D. Fayer, “Probing dynamics of complex molecular systems with ultrafast 2D IR vibrational echo spectroscopy,” *Phys Chem Chem Phys*, vol. 9, no. 13, pp. 1533–1549, 2007.
[41] J. P. Moy and J.-P. h. Reboul, “Operation of a double heterostructure PbSnTe laser at 10.6 μm, 85 K,” *Infrared Phys.*, vol. 22, no. 3, pp. 163–166, May 1982.
[42] J. Faist, F. Capasso, D. L. Sivco, C. Sirtori, A. L. Hutchinson, and A. Y. Cho, “Quantum Cascade Laser,” *Science*, vol. 264, no. 5158, pp. 553–556, Apr. 1994.
[43] R. Ghosh and L. Mandel, “Observation of nonclassical effects in the interference of two photons,” *Phys Rev Lett*, vol. 59, no. 17, pp. 1903–1905, Oct. 1987.
[44] P. G. Kwiat, K. Mattle, H. Weinfurter, A. Zeilinger, A. V. Sergienko, and Y. Shih, “New High-Intensity Source of Polarization-Entangled Photon Pairs,” *Phys Rev Lett*, vol. 75, no. 24, pp. 4337–4341, Dec. 1995.
[45] R. L. Sutherland and R. Hopkins F. Kenneth, “Handbook of Nonlinear Optics,” *Opt. Eng.*, vol. 36, no. 3, pp. 964–964, 1997.
[46] Y. Shen, *The Principles of Nonlinear Optics (Wiley Classics Library)*. Wiley-Interscience, 2002.
[47] H. M. Driel, “Synchronously pumped optical parametric oscillators,” *Appl. Phys. B*, vol. 60, no. 5, pp. 411–420.
[48] L. E. Myers, R. C. Eckardt, M. M. Fejer, R. L. Byer, W. R. Bosenberg, and J. W. Pierce, “Quasi-phase-matched optical parametric oscillators in bulk periodically poled LiNbO3,” *J Opt Soc Am B*, vol. 12, no. 11, pp. 2102–2116, Nov. 1995.
[49] L. E. Myers and W. R. Bosenberg, “Periodically poled lithium niobate and quasi-phase-matched optical parametric oscillators,” *IEEE J. Quantum Electron.*, vol. 33, no. 10, pp. 1663–1672, Oct. 1997.
[50] Masaru Nakamura and Shinji Higuchi and Shunji Takekawa and Kazuya Terabe and Yasunori Furukawa and Kenji Kitamura, “Optical Damage Resistance and Refractive Indices in Near-Stoichiometric MgO-Doped LiNbO 3,” *Jpn. J. Appl. Phys.*, vol. 41, no. 1A, p. L49, 2002.

[51] J. G. Gordon, O. R. Melroy, and M. F. Toney, “Structure of metal-electrolyte interfaces: Copper on gold(111), water on silver(111),” *Surf. Struct. Electrochem. React.*, vol. 40, no. 1, pp. 3–8, Jan. 1995.
[52] S. Pons, C. Korzeniewski, R. B. Shirts, and A. Bewicks, “Field-induced infrared absorption in metal surface spectroscopy: the electrochemical Stark effect,” *J. Phys. Chem.*, vol. 89, no. 11, pp. 2297–2298, May 1985.
[53] K. Ataka, T. Yotsuyanagi, and M. Osawa, “Potential-Dependent Reorientation of Water Molecules at an Electrode/Electrolyte Interface Studied by Surface-Enhanced Infrared Absorption Spectroscopy,” *J. Phys. Chem.*, vol. 100, no. 25, pp. 10664–10672, Jan. 1996.
[54] M. F. Toney, J. N. Howard, J. Richer, G. L. Borges, J. G. Gordon, O. R. Melroy, D. G. Wiesler, D. Yee, and L. B. Sorensen, “Voltage-dependent ordering of water molecules at an electrode-electrolyte interface,” *Nature*, vol. 368, no. 6470, pp. 444–446, Mar. 1994.
[55] D. B. Parry, M. G. Samant, H. Seki, M. R. Philpott, and K. Ashley, “In situ Fourier transform infrared spectroelectrochemical study of bisulfate and sulfate adsorption on gold, with and without the underpotential deposition of copper,” *Langmuir*, vol. 9, no. 7, pp. 1878–1887, Jul. 1993.
[56] M. D. Stoller, S. Park, Y. Zhu, J. An, and R. S. Ruoff, “Graphene-Based Ultracapacitors,” *Nano Lett.*, vol. 8, no. 10, pp. 3498–3502, Oct. 2008.
[57] L. Qu, Y. Liu, J.-B. Baek, and L. Dai, “Nitrogen-Doped Graphene as Efficient Metal-Free Electrocatalyst for Oxygen Reduction in Fuel Cells,” *ACS Nano*, vol. 4, no. 3, pp. 1321–1326, Mar. 2010.
[58] M. Winter and R. J. Brodd, “What Are Batteries, Fuel Cells, and Supercapacitors?,” *Chem. Rev.*, vol. 104, no. 10, pp. 4245–4270, Oct. 2004.
[59] Paunovic, M., Schlesinger, M. & Snyder, D. D., *Modern Electroplating*. Wiley, 2010.
[60] A. C. Hillier, S. Kim, and A. J. Bard, “Measurement of Double-Layer Forces at the Electrode/Electrolyte Interface Using the Atomic Force Microscope: Potential and Anion Dependent Interactions,” *J. Phys. Chem.*, vol. 100, no. 48, pp. 18808–18817, Jan. 1996.
[61] S. Pons, T. Davidson, and A. Bewick, “Vibrational spectroscopy of the electrode-electrolyte interface,” *J. Electroanal. Chem. Interfacial Electrochem.*, vol. 160, no. 1, pp. 63–71, Jan. 1984.
[62] P. S. Cremer, X. Su, Y. R. Shen, and G. A. Somorjai, “Ethylene Hydrogenation on Pt(111) Monitored in Situ at High Pressures Using Sum Frequency Generation,” *J. Am. Chem. Soc.*, vol. 118, no. 12, pp. 2942–2949, Jan. 1996.
[63] H.-X. Zhang, Y. Sasaki, M. Abe, Y. Zhang, S. Ye, M. Osawa, and K. Uosaki, “Electrochemical and infrared spectroscopic study of the self-assembled monolayer of a cyano-bridged dimeric triruthenium complex on gold surface,” *J. Electroanal. Chem.*, vol. 714–715, pp. 51–55, Feb. 2014.
[64] F. W. Richey, B. Dyatkin, Y. Gogotsi, and Y. A. Elabd, “Ion Dynamics in Porous Carbon Electrodes in Supercapacitors Using in Situ Infrared Spectroelectrochemistry,” *J. Am. Chem. Soc.*, vol. 135, no. 34, pp. 12818–12826, Aug. 2013.
[65] R. A. Campbell, S. R. W. Parker, J. P. R. Day, and C. D. Bain, “External Reflection FTIR Spectroscopy of the Cationic Surfactant Hexadecyltrimethylammonium Bromide (CTAB) on an Overflowing Cylinder,” *Langmuir*, vol. 20, no. 20, pp. 8740–8753, Sep. 2004.

[66] H. Seki, K. Kunimatsu, and W. G. Golden, “A Thin-Layer Electrochemical Cell for Infrared Spectroscopic Measurements of the Electrode/Electrolyte Interface,” *Appl. Spectrosc.*, vol. 39, no. 3, pp. 437–443, May 1985.
[67] Y. Wang, Z. Shi, Y. Huang, Y. Ma, C. Wang, M. Chen, and Y. Chen, “Supercapacitor Devices Based on Graphene Materials,” *J. Phys. Chem. C*, vol. 113, no. 30, pp. 13103–13107, Jul. 2009.
[68] X. Wang, L. Zhi, and K. Müllen, “Transparent, Conductive Graphene Electrodes for Dye-Sensitized Solar Cells,” *Nano Lett.*, vol. 8, no. 1, pp. 323–327, Jan. 2008.
[69] S. Bae, H. Kim, Y. Lee, X. Xu, J.-S. Park, Y. Zheng, J. Balakrishnan, T. Lei, H. Ri Kim, Y. I. Song, Y.-J. Kim, K. S. Kim, B. Ozyilmaz, J.-H. Ahn, B. H. Hong, and S. Iijima, “Roll-to-roll production of 30-inch graphene films for transparent electrodes,” *Nat Nano*, vol. 5, no. 8, pp. 574–578, Aug. 2010.
[70] Z. Q. Li, E. A. Henriksen, Z. Jiang, Z. Hao, M. C. Martin, P. Kim, H. L. Stormer, and D. N. Basov, “Dirac charge dynamics in graphene by infrared spectroscopy,” *Nat Phys*, vol. 4, no. 7, pp. 532–535, Jul. 2008.
[71] F. Wang, Y. Zhang, C. Tian, C. Girit, A. Zettl, M. Crommie, and Y. R. Shen, “Gate-Variable Optical Transitions in Graphene,” *Science*, vol. 320, no. 5873, pp. 206–209, 2008.
[72] L. Ju, B. Geng, J. Horng, C. Girit, M. Martin, Z. Hao, H. A. Bechtel, X. Liang, A. Zettl, Y. R. Shen, and F. Wang, “Graphene plasmonics for tunable terahertz metamaterials,” *Nat Nano*, vol. 6, no. 10, pp. 630–634, Oct. 2011.
[73] K. Nakamoto, “Frontmatter,” in *Infrared and Raman Spectra of Inorganic and Coordination Compounds*, John Wiley & Sons, Inc., 2008, pp. i–xi.
[74] M. Osawa, “Dynamic Processes in Electrochemical Reactions Studied by Surface-Enhanced Infrared Absorption Spectroscopy (SEIRAS),” *Bull. Chem. Soc. Jpn.*, vol. 70, no. 12, pp. 2861–2880, 1997.
[75] K. F. Mak, M. Y. Sfeir, Y. Wu, C. H. Lui, J. A. Misewich, and T. F. Heinz, “Measurement of the Optical Conductivity of Graphene,” *Phys Rev Lett*, vol. 101, no. 19, p. 196405, Nov. 2008.
[76] R. R. Nair, P. Blake, A. N. Grigorenko, K. S. Novoselov, T. J. Booth, T. Stauber, N. M. R. Peres, and A. K. Geim, “Fine Structure Constant Defines Visual Transparency of Graphene,” *Science*, vol. 320, no. 5881, pp. 1308–1308, 2008.
[77] K. Jia, J. Luo, R. Hu, J. Zhan, H. Cao, Y. Su, H. Zhu, L. Xie, C. Zhao, D. Chen, and T. Ye, “Evaluation of PMMA Residues as a Function of Baking Temperature and a Graphene Heat-Free-Transfer Process to Reduce Them,” *ECS J. Solid State Sci. Technol.*, vol. 5, no. 3, pp. P138–P141, Jan. 2016.
[78] J. Kim, H. Son, D. J. Cho, B. Geng, W. Regan, S. Shi, K. Kim, A. Zettl, Y.-R. Shen, and F. Wang, “Electrical Control of Optical Plasmon Resonance with Graphene,” *Nano Lett.*, vol. 12, no. 11, pp. 5598–5602, Nov. 2012.
[79] M. Milosevic and S. L. Berets, “Applications of the Theory of Optical Spectroscopy to Numerical Simulations,” *Appl Spectrosc*, vol. 47, no. 5, pp. 566–574, May 1993.
[80] M. G. Murray and W. F. Thompson, “Rapid isolation of high molecular weight plant DNA,” *Nucleic Acids Res.*, vol. 8, no. 19, pp. 4321–4326, Oct. 1980.
[81] T. K. Sau and C. J. Murphy, “Room Temperature, High-Yield Synthesis of Multiple Shapes of Gold Nanoparticles in Aqueous Solution,” *J. Am. Chem. Soc.*, vol. 126, no. 28, pp. 8648–8649, Jul. 2004.

[82] V. C. Moore, M. S. Strano, E. H. Haroz, R. H. Hauge, R. E. Smalley, J. Schmidt, and Y. Talmon, “Individually Suspended Single-Walled Carbon Nanotubes in Various Surfactants,” *Nano Lett.*, vol. 3, no. 10, pp. 1379–1382, Oct. 2003.
[83] W. Wang, B. Gu, L. Liang, and W. A. Hamilton, “Adsorption and Structural Arrangement of Cetyltrimethylammonium Cations at the Silica Nanoparticle−Water Interface,” *J. Phys. Chem. B*, vol. 108, no. 45, pp. 17477–17483, Nov. 2004.
[84] T. K. Sau and C. J. Murphy, “Self-Assembly Patterns Formed upon Solvent Evaporation of Aqueous Cetyltrimethylammonium Bromide-Coated Gold Nanoparticles of Various Shapes,” *Langmuir*, vol. 21, no. 7, pp. 2923–2929, Mar. 2005.
[85] M. E. Spira and A. Hai, “Multi-electrode array technologies for neuroscience and cardiology,” *Nat Nano*, vol. 8, no. 2, pp. 83–94, Feb. 2013.
[86] M. R. Angle, B. Cui, and N. A. Melosh, “Nanotechnology and neurophysiology,” *Large-Scale Rec. Technol. 32*, vol. 32, pp. 132–140, Jun. 2015.
[87] G. T. Einevoll, C. Kayser, N. K. Logothetis, and S. Panzeri, “Modelling and analysis of local field potentials for studying the function of cortical circuits,” *Nat Rev Neurosci*, vol. 14, no. 11, pp. 770–785, Nov. 2013.
[88] M. E. J. Obien, K. Deligkaris, T. Bullmann, D. J. Bakkum, and U. Frey, “Revealing neuronal function through microelectrode array recordings,” *Front. Neurosci.*, vol. 8, p. 423, 2014.
[89] U. Frey, U. Egert, F. Heer, S. Hafizovic, and A. Hierlemann, “Microelectronic system for high-resolution mapping of extracellular electric fields applied to brain slices,” *Biosens. Bioelectron.*, vol. 24, no. 7, pp. 2191–2198, Mar. 2009.
[90] K. D. Dorfman, S. B. King, D. W. Olson, J. D. P. Thomas, and D. R. Tree, “Beyond Gel Electrophoresis: Microfluidic Separations, Fluorescence Burst Analysis, and DNA Stretching,” *Chem. Rev.*, vol. 113, no. 4, pp. 2584–2667, Apr. 2013.
[91] Z. R. Gagnon, “Cellular dielectrophoresis: Applications to the characterization, manipulation, separation and patterning of cells,” *ELECTROPHORESIS*, vol. 32, no. 18, pp. 2466–2487, 2011.
[92] C. Zhang, K. Khoshmanesh, A. Mitchell, and K. Kalantar-zadeh, “Dielectrophoresis for manipulation of micro/nano particles in microfluidic systems,” *Anal. Bioanal. Chem.*, vol. 396, no. 1, pp. 401–420, 2010.
[93] B. Çetin and D. Li, “Dielectrophoresis in microfluidics technology,” *ELECTROPHORESIS*, vol. 32, no. 18, pp. 2410–2427, 2011.
[94] Z. Tang, S. Hong, D. Djukic, V. Modi, A. C. West, J. Yardley, and R. M. Osgood, “Electrokinetic flow control for composition modulation in a microchannel,” *J. Micromechanics Microengineering*, vol. 12, no. 6, p. 870, 2002.
[95] T. Kaneko, F. Nomura, T. Hamada, Y. Abe, H. Takamori, T. Sakakura, K. Takasuna, A. Sanbuissho, J. Hyllner, P. Sartipy, and K. Yasuda, “On-chip in vitro cell-network pre-clinical cardiac toxicity using spatiotemporal human cardiomyocyte measurement on a chip,” *Sci. Rep.*, vol. 4, p. 4670, Apr. 2014.
[96] T. J. Herron, P. Lee, and J. Jalife, “Optical Imaging of Voltage and Calcium in Cardiac Cells & Tissues,” *Circ. Res.*, vol. 110, no. 4, pp. 609–623, Feb. 2012.
[97] C. Morris and H. Lecar, “Voltage oscillations in the barnacle giant muscle fiber.,” *Biophys. J.*, vol. 35, no. 1, pp. 193–213, Jul. 1981.

[98] A. L. Hodgkin, A. F. Huxley, and B. Katz, “Measurement of current-voltage relations in the membrane of the giant axon of Loligo,” *J. Physiol.*, vol. 116, no. 4, pp. 424–448, 1952.
[99] B. Hofmann, V. Maybeck, S. Eick, S. Meffert, S. Ingebrandt, P. Wood, E. Bamberg, and A. Offenhausser, “Light induced stimulation and delay of cardiac activity,” *Lab. Chip*, vol. 10, no. 19, pp. 2588–2596, 2010.
[100] M. Hutzler, A. Lambacher, B. Eversmann, M. Jenkner, R. Thewes, and P. Fromherz, “High-Resolution Multitransistor Array Recording of Electrical Field Potentials in Cultured Brain Slices,” *J. Neurophysiol.*, vol. 96, no. 3, pp. 1638–1645, 2006.
[101] A. Lambacher, M. Jenkner, M. Merz, B. Eversmann, R. A. Kaul, F. Hofmann, R. Thewes, and P. Fromherz, “Electrical imaging of neuronal activity by multi-transistor-array (MTA) recording at 7.8 μm resolution,” *Appl. Phys. A*, vol. 79, no. 7, pp. 1607–1611, 2004.
[102] J. Park, C. A. Werley, V. Venkatachalam, J. M. Kralj, S. D. Dib-Hajj, S. G. Waxman, and A. E. Cohen, “Screening Fluorescent Voltage Indicators with Spontaneously Spiking HEK Cells,” *PLoS ONE*, vol. 8, no. 12, p. e85221, 2013.
[103] D. Shoham, D. E. Glaser, A. Arieli, T. Kenet, C. Wijnbergen, Y. Toledo, R. Hildesheim, and A. Grinvald, “Imaging Cortical Dynamics at High Spatial and Temporal Resolution with Novel Blue Voltage-Sensitive Dyes,” *Neuron*, vol. 24, no. 4, pp. 791–802, Dec. 1999.
[104] C. Stosiek, O. Garaschuk, K. Holthoff, and A. Konnerth, “In vivo two-photon calcium imaging of neuronal networks,” *Proc. Natl. Acad. Sci.*, vol. 100, no. 12, pp. 7319–7324, Jun. 2003.
[105] M. W. Barnett and P. M. Larkman, “The action potential,” *Pract. Neurol.*, vol. 7, no. 3, pp. 192–197, Jun. 2007.
[106] D. E. Goldman, “POTENTIAL, IMPEDANCE, AND RECTIFICATION IN MEMBRANES,” *J. Gen. Physiol.*, vol. 27, no. 1, pp. 37–60, Sep. 1943.
[107] Y. Gao, R.-J. Shiue, X. Gan, L. Li, C. Peng, I. Meric, L. Wang, A. Szep, D. Walker, J. Hone, and D. Englund, “High-Speed Electro-Optic Modulator Integrated with Graphene-Boron Nitride Heterostructure and Photonic Crystal Nanocavity,” *Nano Lett.*, vol. 15, no. 3, pp. 2001–2005, Mar. 2015.
[108] C. T. Phare, Y.-H. Daniel Lee, J. Cardenas, and M. Lipson, “Graphene electro-optic modulator with 30 GHz bandwidth,” *Nat Photon*, vol. 9, no. 8, pp. 511–514, Aug. 2015.
[109] F. Seifert, P. Kwee, M. Heurs, B. Willke, and K. Danzmann, “Laser power stabilization for second-generation gravitational wave detectors,” *Opt Lett*, vol. 31, no. 13, pp. 2000–2002, Jul. 2006.
[110] J. T. Kim and S.-Y. Choi, “Graphene-based plasmonic waveguides for photonic integrated circuits,” *Opt Express*, vol. 19, no. 24, pp. 24557–24562, Nov. 2011.
[111] S. J. Koester and M. Li, “Waveguide-Coupled Graphene Optoelectronics,” *Sel. Top. Quantum Electron. IEEE J. Of*, vol. 20, no. 1, pp. 84–94, Jan. 2014.
[112] M. Liu, X. Yin, E. Ulin-Avila, B. Geng, T. Zentgraf, L. Ju, F. Wang, and X. Zhang, “A graphene-based broadband optical modulator,” *Nature*, vol. 474, no. 7349, pp. 64–67, Jun. 2011.
[113] Y. Liu, A. Chadha, D. Zhao, J. R. Piper, Y. Jia, Y. Shuai, L. Menon, H. Yang, Z. Ma, S. Fan, F. Xia, and W. Zhou, “Approaching total absorption at near infrared in a large area monolayer graphene by critical coupling,” *Appl. Phys. Lett.*, vol. 105, no. 18, 2014.

[114] A. Majumdar, J. Kim, J. Vuckovic, and F. Wang, “Electrical Control of Silicon Photonic Crystal Cavity by Graphene,” *Nano Lett.*, vol. 13, no. 2, pp. 515–518, Feb. 2013.
[115] J. R. Piper and S. Fan, “Total Absorption in a Graphene Monolayer in the Optical Regime by Critical Coupling with a Photonic Crystal Guided Resonance,” *ACS Photonics*, vol. 1, no. 4, pp. 347–353, Apr. 2014.
[116] R.-J. Shiue, X. Gan, Y. Gao, L. Li, X. Yao, A. Szep, D. Walker, J. Hone, and D. Englund, “Enhanced photodetection in graphene-integrated photonic crystal cavity,” *Appl. Phys. Lett.*, vol. 103, no. 24, 2013.
[117] F. J. García de Abajo, “Graphene Plasmonics: Challenges and Opportunities,” *ACS Photonics*, vol. 1, no. 3, pp. 135–152, Mar. 2014.
[118] A. N. Grigorenko, M. Polini, and K. S. Novoselov, “Graphene plasmonics,” *Nat Photon*, vol. 6, no. 11, pp. 749–758, Nov. 2012.
[119] T. Low and P. Avouris, “Graphene Plasmonics for Terahertz to Mid-Infrared Applications,” *ACS Nano*, vol. 8, no. 2, pp. 1086–1101, Feb. 2014.
[120] L. Ju, B. Geng, J. Horng, C. Girit, M. Martin, Z. Hao, H. A. Bechtel, X. Liang, A. Zettl, Y. R. Shen, and F. Wang, “Graphene plasmonics for tunable terahertz metamaterials,” *Nat Nano*, vol. 6, no. 10, pp. 630–634, Oct. 2011.
[121] S. H. Lee, J. Choi, H.-D. Kim, H. Choi, and B. Min, “Ultrafast refractive index control of a terahertz graphene metamaterial,” *Sci. Rep.*, vol. 3, p. 2135, Jul. 2013.
[122] S. H. Lee, M. Choi, T.-T. Kim, S. Lee, M. Liu, X. Yin, H. K. Choi, S. S. Lee, C.-G. Choi, S.-Y. Choi, X. Zhang, and B. Min, “Switching terahertz waves with gate-controlled active graphene metamaterials,” *Nat Mater*, vol. 11, no. 11, pp. 936–941, Nov. 2012.
[123] Y. Long, R. Su, Q. Wang, L. Shen, B. Li, and W. Zheng, “Deducing critical coupling condition to achieve perfect absorption for thin-film absorbers and identifying key characteristics of absorbing materials needed for perfect absorption,” *Appl. Phys. Lett.*, vol. 104, no. 9, 2014.
[124] W. Zhang, S. Serna, X. L. Roux, L. Vivien, and E. Cassan, “Highly sensitive refractive index sensing by fast detuning the critical coupling condition of slot waveguide ring resonators,” *Opt Lett*, vol. 41, no. 3, pp. 532–535, Feb. 2016.
[125] S. Zhu, A. W. Yu, D. Hawley, and R. Roy, “Frustrated total internal reflection: A demonstration and review,” *Am. J. Phys.*, vol. 54, no. 7, pp. 601–607, 1986.
[126] *CLASSICAL ELECTRODYNAMICS, 3RD ED*. Wiley India Pvt. Limited, 2007.
[127] F. H. Labeed and H. O. Fatoyinbo, *Microfluidics in Detection Science: Lab-on-a-chip Technologies*. Royal Society of Chemistry, 2014.
[128] M. W. Shinwari, D. Zhitomirsky, I. A. Deen, P. R. Selvaganapathy, M. J. Deen, and D. Landheer, “Microfabricated Reference Electrodes and their Biosensing Applications,” *Sensors*, vol. 10, no. 3, pp. 1679–1715, 2010.
[129] W. M. Haynes and D. R. Lide, *CRC handbook of chemistry and physics : a ready-reference book of chemical and physical data*. Boca Raton, Fla.: CRC Press, 2011.